IMPLEMENTATION OF MICROPHONE ARRAY PROCESSING TECHNIQUES ON A SYNTHETIC ARRAY FOR FLUID POWER NOISE DIAGNOSTICS

A Thesis

Submitted to the Faculty

of

Purdue University

by

Dan Ding

In Partial Fulfillment of the

Requirements for the Degree

of

Master of Science in Mechanical Engineering

May 2019

Purdue University

West Lafayette, Indiana

THE PURDUE UNIVERSITY GRADUATE SCHOOL
STATEMENT OF THESIS APPROVAL

Dr. Andrea Vacca, Co-Chair

School of Mechanical Engineering

Dr. Stuart Bolton, Co-Chair

School of Mechanical Engineering

Dr. Yangfan Liu

School of Mechanical Engineering

Approved by:

Dr. Jay P. Gore

Head of the School Graduate Program

To Monika.

ACKNOWLEDGMENTS

My experience at Maha was a joyful and memorable journey. First of all, I would like to thank all my committee members. I'm so thankful for Dr. Andrea Vacca, not only for funding me after the mournful August, but also for understanding and supporting my decisions of early graduation. Besides, I'm grateful to my two committee members from Herrick Lab, Dr. Stuart Bolton and Dr. Yangfan Liu. So many times, they pointed out directions and provided constructive suggestions to my research. In addition, I particularly appreciate Dr. Bolton caring my complicated situation. I'm grateful to my colleagues at Maha, particularly Paul. He has been mentoring me since my SURF. His experience protected me from falling into pitfalls for hundreds of times. Many thanks to the Maha staff, especially Susan. Finally, I would like to thank Dr. Monika Ivantysynova, my previous advisor, who took me to the world of research. For a long time, her appreciation and encouragement motivated me to keep doing excellent work. I hope she'll like this thesis.

TABLE OF CONTENTS

Page

Page

LIST OF TABLES

LIST OF FIGURES

Figure Page

Figure Page

SYMBOLS

$(\cdot)^*$	Complex conjugate
$(\cdot)^{\mathrm{T}}$	Transpose
$(\cdot)^{\mathrm{H}}$	Hermitian complex transpose
$(\cdot)^\dagger$	Pseudoinverse
$(\cdot)!$	Factorial
$*$	Commutative convolution operation
∇	Gradient
∇^2	Laplace operator
∇_x^2	Laplace operator in Cartesian coordinates
∇_r^2	Laplace operator in spherical coordinates
$\mathrm{Im}\{\cdot\}$	Imaginary part
$\mathrm{Re}\{\cdot\}$	Real part
a_k	Fourier series coefficient
a_{nm}	Spherical Fourier series coefficient
c	Speed of sound
$\mathbb{C}$	One-dimensional space of complex numbers
$\mathrm{E}[\cdot]$	Expectation
f	Frequency
$\mathcal{F}(\cdot)$	Fourier transform operator
$h_n^{(1)}, h_n^{(2)}$	Spherical Hankel Function
I	Sound intensity
j	imaginary unit ($\sqrt{-1}$)
$j_n(x), y_n(x)$	Spherical Bessel functions
k	wave number

$\mathbb{N}$	Set of all natural numbers
p	Sound pressure in space domain
$p_{nm}(r)$	Sound pressure in spherical harmonics domain
$P_n^m(x)$	Associated Legendres Function
r	Radius
$\mathbb{R}$	One-dimensional space of real numbers
$\mathbb{R}^3$	Three-dimensional space of real numbers
$x_d(t)$	Deterministic component of signal $x(t)$
$x_r(t)$	Residual part of signal $x(t)$
$Y_n^m(\theta, \phi)$	Spherical harmonic function
$\mathbb{Z}$	Set of all integers
$\mathbb{Z}^+$	Set of all positive integers
δ_{ij}, δ_n	Kronecker delta function
λ	Wave length
μ	Mean value
σ^2	Variance
ω	Angular frequency
Π	Sound Power
ϕ	Azimuth angle
ρ	Instantaneous density
ρ_0	Equilibrium density
θ	Polar angle

ABBREVIATIONS

ABN	Air-borne Noise
BEM	Boundary Element Method
CTFT	Continuous-time Fourier Transform
DAQ	Data Acquisition
DFT	Discrete Fourier Transform
DTFT	Discrete-time Fourier Transform
ESM	Equivalent Source Method
HELS	Helmholtz Equation Least Squares
IBEM	Inverse Boundary Element Method
IDC	Inner Dead Center
IRF	Impulse Response Function
LTI	Linear Time Invariant
FEM	Finite Element Method
FFT	Fast Fourier Transform
FBN	Fluid-borne Noise
MUSIC	Multiple Signal Classification
NAH	Near-field Acoustic Holography
NSI	Noise Source Identification
NVH	Noise, Vibration, and Harshness
ODC	Outer Dead Center
SBN	Structure-borne Noise
SNR	Signal-to-Noise Ratio
SIL	Sound Intensity Level
SPL	Sound Pressure Level

SVD	Singular Value Decomposition
SWL	Sound Power Level
TSA	Time Synchronous Average

ABSTRACT

Ding, Dan M.S.M.E, Purdue University, May 2019. Implementation of Microphone Array Processing Techniques on A Synthetic Array for Fluid Power Noise Diagnostics. Major Professor: Andrea Vacca.

Fluid power is widely used in a variety of applications such as construction machines, aerospace, automotive, agricultural machinery, manufacturing, etc. Although this technology has many obvious advantages such as compactness, robustness, high power density, and so forth, there is much room for improvement, of which one of the most important and challenging problems is the noise.

Different institutes have been researching fluid power noise for decades. However, much of the experimental investigation was based on simple measurement and analysis techniques, which left the designers/researchers no method of understanding the complicated phenomena. A microphone array is a powerful tool that unfortunately has not been introduced to the fluid power noise research. By capturing the magnitude and phase information in space, a microphone array enables the noise source identification, separation, localization and so forth.

This thesis focuses on implementing the microphone array processing techniques on a synthetic microphone array for fluid power noise diagnostics. Differing from traditional scan-based approaches, the synthetic array is created by synchronizing the non-synchronous measurements to achieve the equivalent effect of a multi-microphone snapshot. The final results will show the power of microphone arrays and provide an economical solution to achieve approximate results when a real microphone array is not available.

1. OVERVIEW

Motivated by the desire for advanced experimental analysis tools, this thesis describes an exploratory implementation of microphone array processing techniques, more specifically, acoustical holography, on a synthesized virtual microphone array for the fluid power noise diagnostics.

Chapter 2 gives a brief introduction to fluid power including its working principle and typical noise sources, microphone array technology, and the state the art of both topics. The state of the art of fluid power research leads to a desire for advanced experimental analysis tools, and the processing enabled by microphone arrays can be the potential solution.

Chapter 3 covers the experimental facilities, including the measurement environment, sensors, data acquisition system, fluid power system setup and, most importantly, the automatic robotic arm. This robot is the key to the synthetic array. Measurements taken by the robot are non-synchronous, which prevents implementing microphone array techniques directly. Thus, another topic in chapter 3 is explaining how to synthesize the non-synchronous measured data to an array data. It involves some assumptions and a synchronization technique.

Chapter 4 introduces the prerequisite theories for developing the acoustical holography methods, including two sections: Fourier analysis and acoustics. The section of Fourier analysis highlights the Fourier series and the Fourier transform in both discrete time and continuous time. In addition to common sinusoidal functions, another Fourier basis defined on the unit sphere is introduced. The section on acoustics mainly discusses the linear wave equation, solutions of the wave equation, sound energy, and its measurement.

Based on the knowledge presented in previous chapters, the principles of acoustical holography are introduced in Chapter 5. Some commonly used methods are reviewed

first. Of all the available methods, a method called HELS is focused on because it suits the robot's feature most, and has a good balance between complexity and performance. To verify the theory and obtain a better understanding of the features of this method, some simulation cases are studied.

Chapter 6 analyzes two measurement cases made by using the synthetic array. Through the use of acoustical holography, as much information about the example sound fields is extracted as possible. Both successful and failed results are discussed. The last chapter summarizes the work of this thesis. As one of the main objectives of this exploratory work, some potential future works and directions are recommended to future researchers.

2. INTRODUCTION

2.1 Brief Introduction to Fluid Power

Fluid power is a technology that transmits energy and controls the actuators motion through the fluid. Within the scope of this thesis, fluid power is narrowly referred to as a hydrostatic technology, or hydraulics, which means the working fluid is liquid instead of gas, and energy transmission is achieved by static pressure propagation instead of the momentum of fluid. Hydrostatic machines are also called positive displacement machines, with which a fixed amount of fluid is displaced per revolution of pump shaft rotation.

A hydraulic system usually includes one or multiple positive displacement machines, of which the ones that convert mechanical power to fluid power are called pumps and the ones that utilize fluid power do mechanical work are called motors. Beside motors, a linear actuator is another type of machine that converts fluid power to mechanical power. Pumps and actuators are connected by hoses, filled with fluid. Varying from one system to another, there might be some other necessary components, such as valves, filters, coolers, and so forth.

Hydraulic systems have a reputation for noise, and most of the noise in a system can be attributed to the positive displacement machines. It is not only because a great level of the noise is radiated by the positive displacement machines themselves, but also because the noise generated by the system is directly related to these machines. The oscillating moments generated by varying pressure of the displacement chambers leads to the vibration of the system structure and cause structure-borne noise (SBN). Due to the finite number of displacement elements, e.g. pistons in piston machines, the pump delivery flow pulsates at the pump ports. This pulsating flow is amplified with effects caused by fluid compressibility and other design-related effects like cross-

porting, internal and external leakages. Consequently, the flow ripple leads to pressure ripple in the connected pipes, which are transmitted through the system and cause fluid-borne noise (FBN).

2.1.1 Axial Piston Machine

Among various categories of positive displacement machines, the piston machines are one of the most popular type. This thesis only uses axial piston swash plate type machine as the object for experimental diagnostics. Nevertheless, the proposed analysis method can still be applied to other types of machines, as long as the assumptions behind the method is valid. Figure 2.1 highlights the main components of a sectioned pump. Of all the components, the shaft, slipper, piston, and cylinder block rotate, and the remaining parts are fixed.

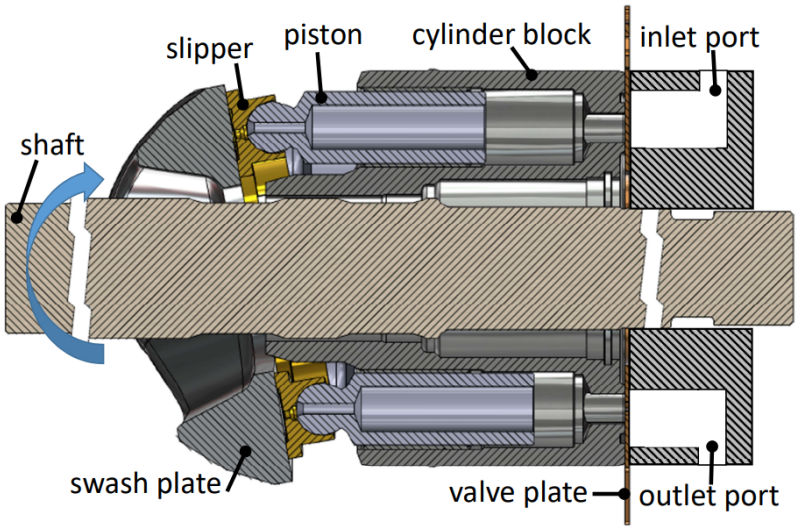

Fig. 2.1. Cross-sectional view of swash plate type axial piston machine (Kalbfleisch 2018)

Axial piston machines displace fluid by the reciprocating motion of the pistons. Take the pumping mode for example, as a piston moves from $\varphi = 180$, or *Inner Dead Center* (IDC), to $\varphi = 0$, or *Outer Dead Center* (ODC), the displacement chamber

volume increases, and displaces fluid into the chamber through the inlet; as the piston rotates from ODC to IDC, the displacement chamber volume decreases, and displaces fluid out of the chamber through the outlet.

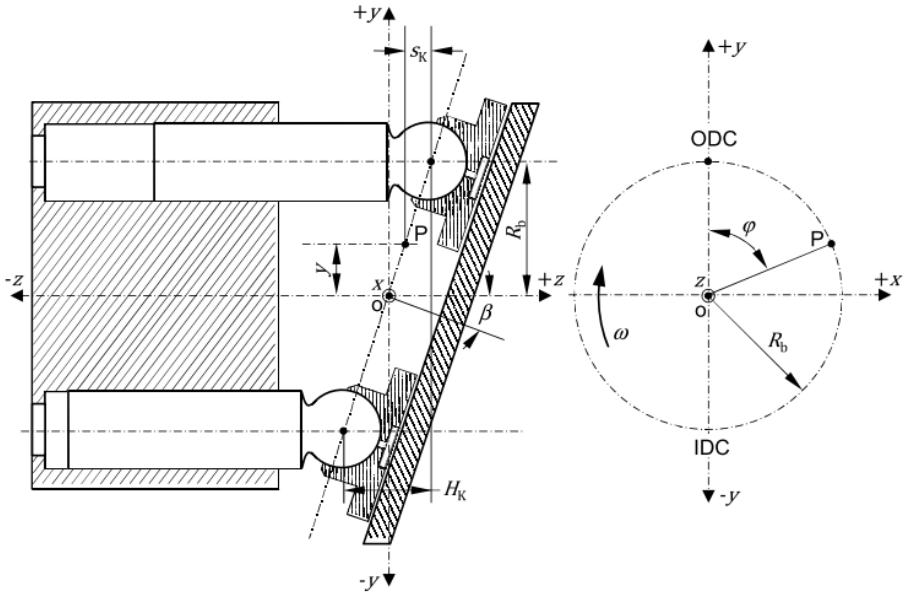

Fig. 2.2. Kinematics of swash plate type axial piston machine (Ivantysyn & Ivantysynova 2003)

The displaced fluid volume by a piston in each shaft revolution is determined by the piston diameter d_K, pitch radius R_b and maximum piston displacement distance, or stroke, which can be adjusted by the swash plate angle β:

$$H_K = 2 \cdot R_b \cdot \tan(\beta). \tag{2.1}$$

2.1.2 Fluid-borne Noise Source

The delivery flow rate of a positive displacement machine is the sum of the delivery flow rate of each piston, i.e.,

$$Q_{geo} = n \cdot z_K \cdot A_K \cdot H_K = n \cdot z_K \cdot \frac{\pi \cdot d_K^2}{2} \cdot R_b \cdot \tan(\beta), \tag{2.2}$$

where z_K is the number of pistons, n is shaft speed in rev/min, A_K is the piston area and d_K is the piston diameter. The subscript stands for 'geometric' because this flow rate is a constant only depending on the machine's geometry.

However, the instantaneous flow rate doesn't equal this constant because the piston velocity varies in a revolution. The kinematic flow rate is thus given by Eq. 2.3

$$\begin{aligned} Q_{kin} = \sum_{i=1}^{z_K} Q_{kin,i} &= \sum_{i=1}^{z_K} v_{k,i} \cdot A_K \\ &= \sum_{i=1}^{z} \omega \cdot R_b \cdot \tan(\beta) \cdot \sin(\varphi_i) \cdot A_K. \end{aligned} \tag{2.3}$$

where v_k is the piston velocity. Eq.2.3 clearly points out the oscillation of the delivery flow. In reality, the flow oscillation is even stronger than that described by this equation, because of the existence of the fluid compressibility, aeration, system impedance, and internal valve plate design, etc (Kim 2012, Kalbfleisch 2015). Figure 2.3 demonstrates a good example.

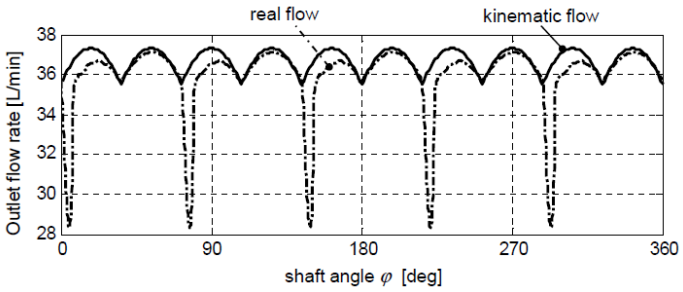

Fig. 2.3. Kinematic and real flow rates for a 5 piston pump (Klop & Ivantysynova 2010*a*)

The interaction of flow oscillation (or flow ripple) and the various components in the hydraulic system, including pipes, hoses, valves, and cylinders, will generate oscillating forces that eventually will result in vibration and the propagation of an acoustic wave. As previously mentioned, this flow ripple is therefore referred to as the fluid-borne noise source.

2.1.3 Structure-borne Noise Source

Beside fluid-borne noise, axial piston machines also generate noise by exerting oscillating forces on the structure directly. Within each displacement chamber, the chamber pressure varies over a shaft revolution. The displacement chamber force (F_{DCi}) combining with the piston friction force (F_{TKi}), and the inertia force (F_{aKi}) creates a single resultant force (F_{rKi}) acting in the z-direction.

$$F_{rKi} = F_{DCi} + F_{TKi} + F_{aKi} \tag{2.4}$$

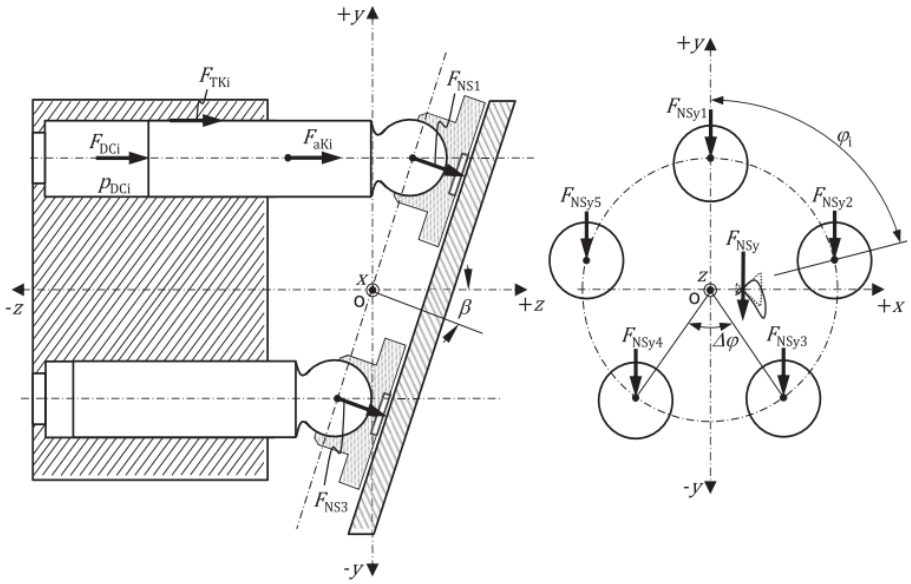

Fig. 2.4. Forces acting on the swash plate of a 5 piston pump (Klop 2010)

Accompanying the solid body assumption, the resulting force (F_{rKi}) generates resultant moments acting on the swash plate in the three axial directions, x, y, and z:

$$M_x = \frac{R_b}{\cos^2(\beta)} \sum_{i=1}^{z} F_{rKi} \cdot \cos(\varphi_i) \tag{2.5}$$

$$M_y = R_b \sum_{i=1}^{z} F_{rKi} \cdot \sin(\varphi_i) \tag{2.6}$$

$$M_z = -R_b \cdot \tan(\beta) \sum_{i=1}^{z} F_{rKi} \cdot \sin(\varphi_i) \tag{2.7}$$

These moments exerted on the swash plate are transmitted to the piston machine's casing and other connected structures and cause vibrations and therefore noise. This type of noise is referred to as structure borne noise, and the moments are considered as the structure borne noise source.

2.1.4 Other Noise Sources

In addition to the two main noise sources mentioned above, there are some other possible noise sources such as (Kalbfleisch 2018):

- Friction forces on sliding parts (bearing grind, insufficient lubrication)
- Mechanical impacting forces on moving components
- Turbulent flow
- Collapsing cavitation bubbles

It has to be clarified that noise induced by many of these sources, technically, can be categorized into structure-borne noise. However, most of these listed noise sources can be avoided in properly designed machines and even in the cases where there exist these noise sources, they are usually much less significant than pressure ripple and swash plate moments. Thus, in most conversation about axial piston machines' noise (including this thesis), FBN and SBN are specifically referred to as noise caused by the pressure ripple and the swash plate moments.

2.2 Brief Introduction to Microphone Array

A microphone array system refers to a collection of microphones operating concurrently for certain acoustic signal processing purposes. Particularly, microphone array technologies have drawn considerable attention as a means of enhancing signal quality and, more recently, visualizing sound fields, and identifying noise sources.

As a matter of fact, microphones are not the only type of sensors that are used to form an array for advanced processing. The earliest sensor array application can be traced back to radar antennas in World War II. Although electromagnetic and sound waves are far different in physical essence, the solutions of their propagation equations share a similar form. As a result, microphone array processing methodologies for the far-field applications are to a great extent influenced by electromagnetic antennas array design. Not limited to applications mentioned above, array signal processing technologies have found their roles in many areas, such as non-destructive evaluation, underwater imaging, machine diagnosis, and so forth (Bai et al. 2013).

2.2.1 Far-field Applications

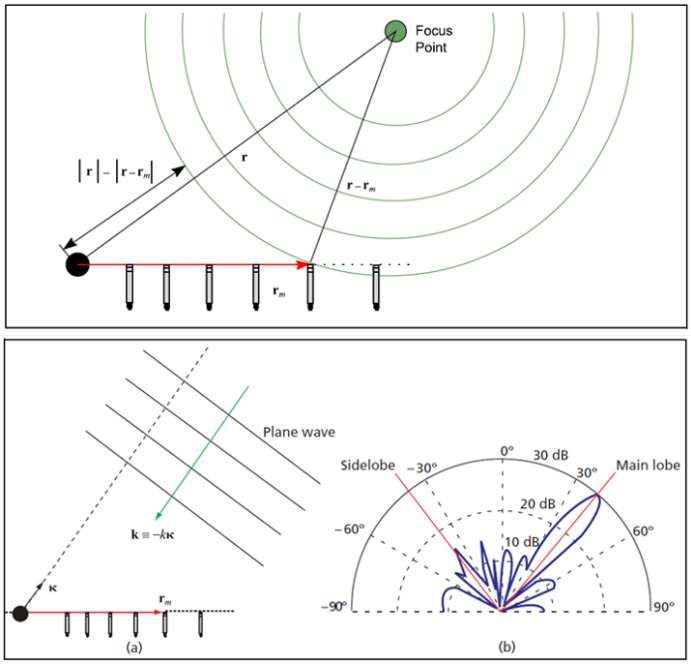

Fig. 2.5. Beamforming Conceptual Graph (Christensen & Hald 2004)

Combining a number of microphones together is advantageous, compared to a single microphone. First, multiple microphones make it much easier to filter out random noise so that the signal-to-noise ratio (SNR) can usually be increased. Secondly, mul-

tiple microphones capture both magnitude and phase information in space, which a single sensor is not able to accomplish. Artificially adjusting the weightings on different sensors enables the manipulation of array directivity. This feature is fascinating because it allows the achievement of spatial filtering i.e. focusing on the primary source of interest while rejecting noise and reverberation in the background. More importantly, this manipulation or direction steering can be all accomplished electronically instead of physically. With these features, microphone arrays are widely used in the context of estimating the direction of arrival (DOA) and enhancing speech quality in telecommunication applications. The manipulation of array directivity is referred to as beamforming, which is achieved by assuming either a plane wave or spherical wave model in space (Figure 2.5). Consequently, this technology particularly suits the long-distance and large scale scenarios such as trains and aircrafts because the sound pressure in the far-field can be described by the two models very well.

2.2.2 Near-field Applications

Apart from the far-field array technologies, acousticians also developed near-field microphone arrays processing since the 1980s. These near-field array techniques were given the name near-field acoustical holography (NAH) when they were first introduced. Since then, numerous NAH techniques have been suggested based on different principles. The purposes of near-field techniques differ from the far-field techniques. The word "holography" implies these techniques aim to reconstruct the complete sound field information and usually represent the results in graphical manners. The information that can be potentially computed by acoustical holography include:

- The sound pressure at any location exterior to the source
- The particle velocity at any location exterior to the source
- Modal vibration patterns of object surfaces (Figure 2.6 (a))
- The vector intensity field, in which energy flows (Figure 2.6 (b))

- Far-field radiation pattern
- The total radiated power

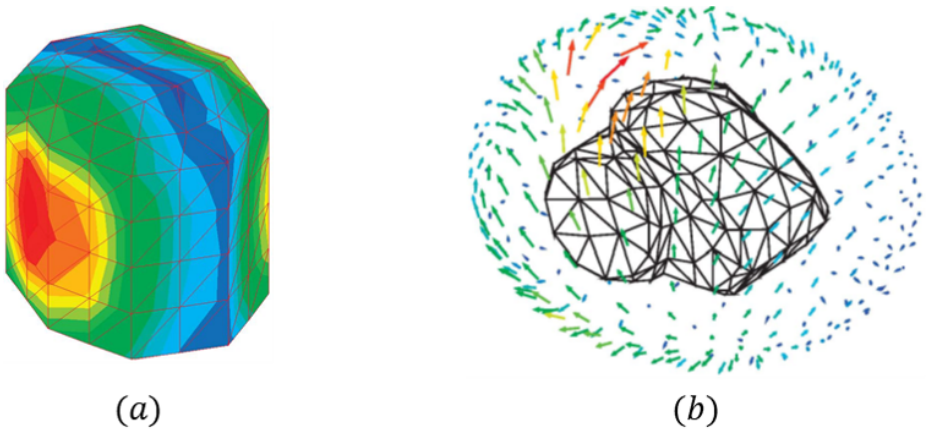

Fig. 2.6. Near-field Acoustical Holography Examples (Bai et al. 2013)

The capability of revealing the full pictures of sound fields makes acoustical holography a very powerful tool in noise source identification (NSI) and sound field visualization for noise analysis and control engineering.

2.3 State of the Art

2.3.1 Fluid Power Noise

As a well-known issue, fluid power noise has been studied for decades. The earliest found source on the study of noise for positive displacement machines can be traced back to Stan Skaistis at the Vicker's pump company in Detroit, Michigan (Skaistis 1962, Kalbfleisch 2018). One of the most profound work in this area was done in the 1970s involving many universities in the United Kingdom, during which the two main noise sources, FBN and SBN, were clearly defined for the first time (British Hydromechanics Research Group 1982). From then on, the fluid power society organizes their research efforts into these two categories.

Since the 1980s, as computing power grew rapidly, great efforts have gone into developing sophisticated models. Edge gave a general overview of developments and contributions of the simulation tools in 1999 (Edge 1999). The progress in the simulation work led to an efficient noise reduction methodology: computational valve plate design. The Maha Fluid Power Research Center at Purdue University led this research (Ivantysynova, Huang & Christiansen 2004, Seeniraj & Ivantysynova 2006, Klop, Williams, Dyminski & Ivantysynova 2007, Seeniraj & Ivantysynova 2008, Klop & Ivantysynova 2008, Klop & Ivantysynova 2010*b*, Kumar Seeniraj, Zhao & Ivantysynova 2011, Seeniraj & Chandran 2011, Kalbfleisch & Ivantysynova 2012, Kalbfleisch 2015). Valve plate design has a great influence on the chamber pressure (therefore swash plate moments) and flow ripple. However, it has been found in many experiments that the sources of FBN and SBN are not simply correlated to the perceived noise. More surprisingly, a recent work by Kim (2017) founds that a successful swash plate momenta elimination by active control inside a pump only affected the sound marginally. These challenging findings imply that there is still unknown phenomena to be discovered between the noise source generation and noise perception.

While a large effort went to developing sophisticated models, very little attention was paid on experimental methods. Most experimental progress has been about improving the sound level measurements. For the quick and fair comparison of sound levels of positive displacement machines produced by different manufacturers, a series of ISO standards were developed (Standard 2002, Standard 2011*a*, Standard 2011*b*). The general requirements of the ISO measurement systems include hemi-anechoic environment, isolation from the prime mover, and spatial sampling at six specified locations on a hemi-sphere. The sparse sampling grid required by ISO standards started being challenged by a 152-point rectangular measurement grid since (Klop & Ivantysynova 2010*a*) at the Maha Fluid Power Research Center, Purdue University. Later the same methodology was applied to evaluate the noise of a number of external gear machines by a 64-point rectangular grid (Opperwall & Vacca 2013). Evolving

from this methodology, a robotic arm has been designed and implemented to automate the grid measurements (Kalbfleisch et al. 2016), which is currently the state of the art sound power measurement methodology for fluid power noise.

2.3.2 Microphone Array Processing Techniques

As already introduced in the previous section, there are two main categories of microphone array processing techniques: far-field methods and near-field methods. Far-field methods are usually referred to as beamforming, and near-field methods mainly include near-field acoustical holography (NAH).

Beamforming

Most beam-forming algorithms were originally developed for other phased-array applications, such as radar and sonar. Based on the same principles behind wave propagation, J. Billingsley (1976) invented the first microphone array called acoustic telescope to localize real-time jet engine noise (Billingsley & Kinns 1976). About 20 years later in 1999, G. Heinz et al. created the first acoustic camera by combining the microphone array with a camera for visualization purposes (Heinz, Döbler & Nguyen 1999). A variety of algorithms are now available in this category, including the Delay-and-Sum (DAS) algorithm, the Minimum Variance Distortionless Response (MVDR) algorithm, the Multiple Signal Classification (MUSIC) (Schmidt 1981) algorithm, the Deconvolution Approach for the Mapping of Acoustic Sources (DAMAS) (Brooks & Humphreys 2006) and artificial neural network algorithm. The most recent application focus of beam-forming has been switched from source localization or visualization to speech enhancement in room.

Fourier-based Acoustical Holography

NAH was first theorized and implemented by Williams, Maynard, and Skudrzyk (Williams, Maynard & Skudrzyk 1980, Maynard, Williams & Lee 1985). It was originally developed for the purpose of noise source identification. Various methods have been developed since then, and there is not a widely accepted categorization of all the methods. This thesis follows the categorization proposed by Liu (Liu 2016) dividing all the methods into two types: the non-parametric methods and the parametric methods. The methods proposed by Williams were in the category of non-parametric methods, which are also referred to as Fourier-based methods. The common idea of these methods is to decompose the sound field into the orthogonal basis functions. The selection of basis functions depends on the coordinate system. Under Cartesian, cylindrical and spherical coordinate system, the Fourier methods have been implemented successfully (Devries 1994).

Equivalent Source Method

To satisfy the requirement of orthogonality, the discrete sampling locations are constrained. Techniques in the parametric category methods don't have this limitation. In general, these methods can be considered as equivalent source methods (ESM). In other words, it is assumed that the actual sound field is equivalent to a field that is generated by a combination of some wave or source components. Depending on the assumptions made for the source components, models with undetermined parameters are built, and after that, the parameters are estimated using measured data.

In many contexts, ESM is narrowly referred to as classical Equivalent Source Methods, in which the sound field is approximated by a distribution of simple sources, such as monopoles or dipoles, with fixed locations (Koopmann, Song & Fahnline 1989, Fahnline & Koopmann 1991, Jeans & Mathews 1992).

To achieve better performance on objects with irregular geometry, the Inverse Boundary Element Method (IBEM) was developed (Bai 1992). It discretizes the object surface into small elements, with the aid of interpolation schemes. Although its formulation relies heavily upon integral representation and Green's function theory, IBEM can also be interpreted as using a distribution of monopoles (pressure terms) and dipoles (normal velocity terms) on a closed boundary (Liu 2016).

In addition to methods using distributed simple lower order sources, Wang and Wu proposed a method utilizing higher order sources with one fixed location (Wang & Wu 1997). Solutions of the Helmholtz equation in the spherical coordinate system are a series of spherical harmonic functions multiplied by spherical Hankel functions. These terms are selected to be the component sources. Coefficients for these terms are estimated by least squares fitting and this method is therefore called Helmholtz Equation Least Squares (HELS).

Methods mentioned above usually only use a finite subset of a complete basis. Thus, information measured but outside of this subspace will be unfortunately discarded. Statistically Optimized Near-field Acoustical Holography (SONAH) was developed to overcome this limitation, i.e., to find an optimized prediction in a larger space, or even the whole space spanned by the complete basis (Cho, Bolton & Hald 2005, Hald 2009). It can also be viewed as a member of the higher order, single location category. Additional flexibility can be achieved by adapting un-fixed sources (Liu 2016).

2.4 Motivation and Objectives

Even in the state-of-the-art experimental system, with a large number of measurements points and considerable accuracy achieved by an automatic robotic arm, the information that can be obtained is still inadequate. It is unable to explain the strange phenomena that don't conform to the current theories of fluid power noise. Given design changes, there is no method to fully understand their effects. Even

for computational work, without comprehensive experimental characterization of the sound field, validation of simulation models is limited. All of these calls for more advanced experimental analysis tools.

Microphone array techniques have been developed for decades and have become very powerful. Unfortunately, they are rarely known to or used by the fluid power community. This thesis aims to introduce this powerful tool to the fluid power researchers. One of the main disadvantages of a microphone array system, including sensors, cables, and a data acquisition system, is it is usually expensive. However, it has been found that the robotic measurement system built at Maha Fluid Power Research Center has the potential to synthesize a "pseudo" microphone array. By doing that, there is no additional cost for implementing microphone array processing techniques on this system.

The first objective of this thesis is to prove the concept of the synthetic array. Once this synthesis approach is proved feasible, the treasure house of array technology will be fully open to the robotic system. Future researchers can pick whatever tool they need from it. This proof of concept must be done in both theory and practice. Thus, one of the acoustical holography methods is applied to study an example pump. Successful implementation will present useful information about the given machine and demonstrate the value of acoustical holography. Realizing the synthetic array is not a true array, the results are not expected to be perfect. Thus, another important objective of this work is discovering the limitations of the current system configuration to provide information and suggestions for future work, either on method development or system modifications.

3. SYNTHETIC MICROPHONE ARRAY

The synthetic microphone array is the core of this thesis. Although similar ideas have been implemented on radar antennae and acousticians have also developed their solutions to apply microphone array processings on non-synchronous measurements, this work presents a unique solution that synchronizes hundreds of sequentially taken measurements to synthesize a microphone array. The physical facilities introduced in the beginning of this chapter are contributed by previous researchers (Klop & Ivantysynova 2010*a*, Kalbfleisch et al. 2016, Kalbfleisch 2018). The process of array synthesis involves an idealized model of two main noise sources, a few assumptions, and a specific synchronization approach. In the end, experimental results will provide valid evidence of the applicability of this proposed method.

3.1 Environment and Facilities

3.1.1 Hemi-anechoic Chamber

Sound measurements are usually performed in anechoic chambers. An anechoic chamber usually has two main functions. First, it isolates the outside noise to make sure all the gathered sound information is generated inside the chamber by the target objects. Secondly, it creates a non-reflective environment or sometimes called free-space, which simplifies the post-processing.

The chamber at Maha Fluid Power Research Center, Purdue University, a hemi-anechoic chamber, designed by Kalbfleisch (Kalbfleisch 2018), was built specifically for positive displacement machines' noise measurements, as shown on Figure 3.1. "Hemi-" means there exists one and only one reflective plane in the chamber. The sound will be reflected back when it hits this plane, which is a required setup in ISO

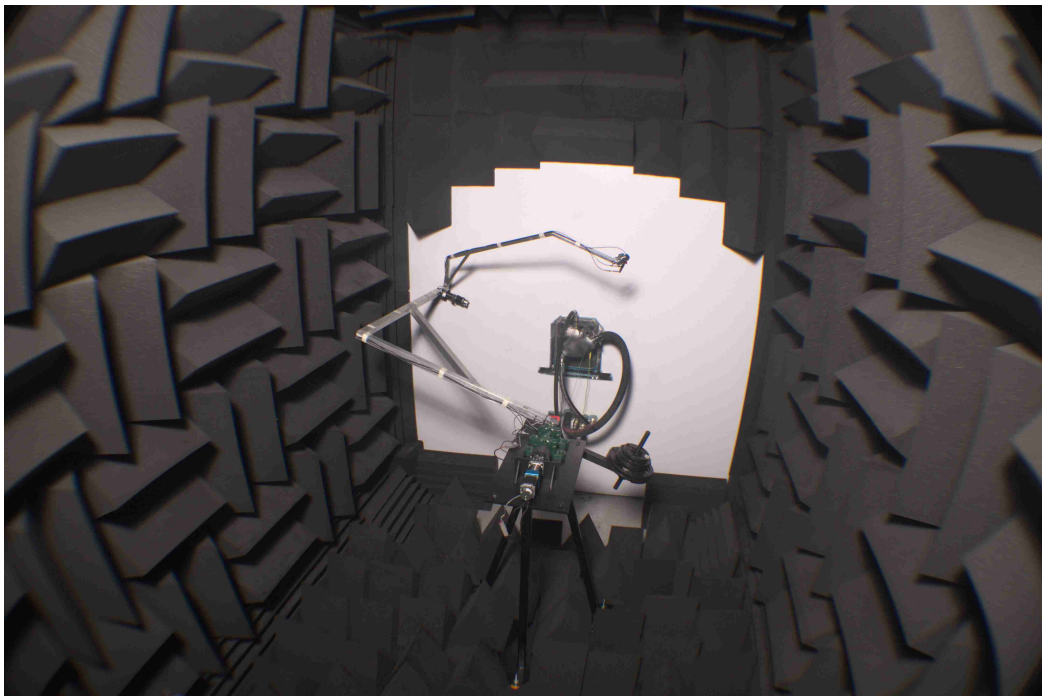

Fig. 3.1. Maha's Hemi-Anechoic Chamber (Kalbfleisch 2018)

Table 3.1.
Sound Chamber Specifications (Kalbfleisch 2018)

Physical dimensions	2.44m × 3.65m × 3.05m (8 ft × 12 ft × 10 ft)
Noise floor	42 dB (above lower limiting frequency)
60 dB Reverberation time	0.11 seconds

Table 3.2.
Microphone Specifications (Klop & Ivantysynova 2010*a*)

Microphones	GRAS, three microphones Type 40A0
Pre-amplifer	GRAS, Type 26CB, 6.35 mm ($\frac{1}{4}$") diameter
Sound Calibrator	GRAS Type 42AB, calibrated at 114.01dB, 1000.25 Hz
Sound Intensity Calibrator	GRAS Type 51AB

standards (Standard 1991, Standard 2002, Standard 2011*b*). In the Maha chamber, this reflective plane is a wall that divides the whole room into two parts: a hemi-anechoic chamber, where the measurements are taken, and an adjacent electric motor room, in which the electric motor and most of the hydraulic components are placed. With multilayer composition and substantial weight, the wall layer, QuietRock 545, effectively reduces the transmission of sound through the wall. Besides, all the possible air gaps are sealed by caulk sealant. In the chamber room, all the remaining surfaces, including the two side walls, ceiling, and the door are covered with acoustic foams in triangular patterns. The ground is not permanently covered, but during measurements, foams are placed on it. All of these structures and treatments guarantees the interference by noise emitted by non-interested sources is minimized. The sensors used to capture the sound pressure are GRAS type 40A0 microphones. Three microphones are combined together to form a probe. The sound pressure gradients measured by the 3 microphones are used to estimate the particle velocity and therefore sound intensity.

3.1.2 Automatic Robotic Arm

To better characterize the sound field, measurements taken at multiple locations is preferred. Traditionally, this was achieved by either putting multiple microphones on a structure with fixed mounting locations or manually adjusting and recording the locations of microphones during the test.

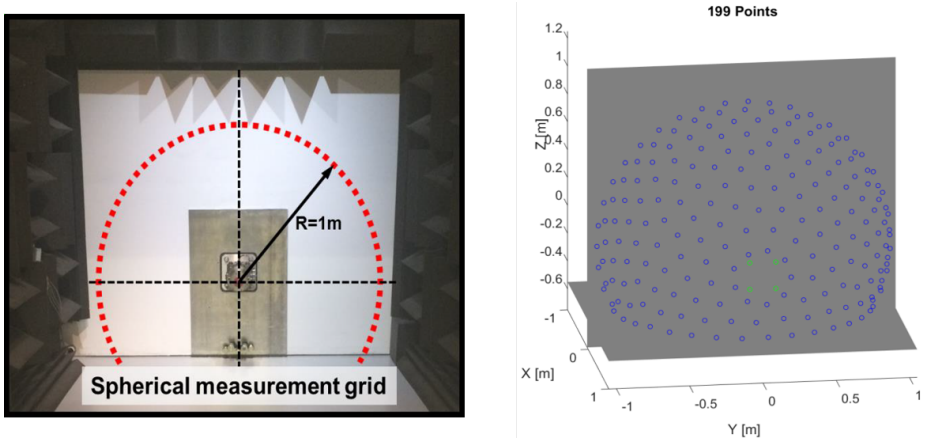

Fig. 3.2. Previous Chamber Setup and a 199-point Grid (Kalbfleisch et al. 2016)

In Maha's chamber, an automatic robotic arm was built to automate the process of moving the microphones. When compared to previously available methods, a robotic arm has a great number of advantages. First, it frees people from staying inside the closed chamber during the whole measurement time. Consequently, it also avoided possible noise and mistakes made by humans. In addition, it is able to take a large number of measurements in a relatively short period of time. Besides the efficiency, the angle sensors on the robot record position information automatically. Last but not least, it allows a flexible measurement setup because changing the measurement locations can be easily done on the computer.

Figure 3.2 shows the chamber setup and an example measurement locations, called grid, when the robotic system was originally designed. Back then, the pump was mounted relatively close to the ground. As a result, the measurements was interfered by the floor reflection and the robot could only cover approximately a quarter of a

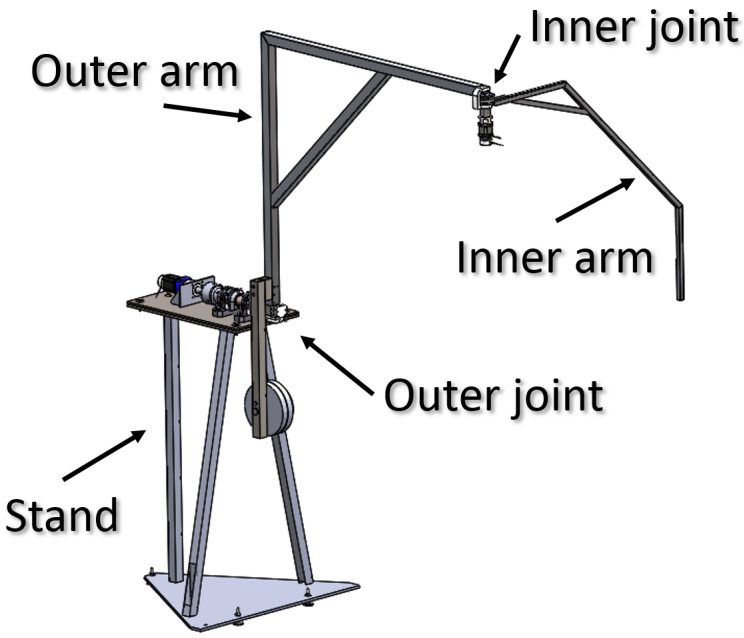

Fig. 3.3. Robot Structure (Kalbfleisch 2018)

sphere. To reduce the effect of the floor reflection and help the investigation of this thesis, the electric motor room was remodelled along with the modification of the robot stand. By doing these, the whole shaft and the robot stand were lifted up by 1.2m, which allowed foams to be placed on the floor during measurements, and enabled the robot coverage of a hemisphere (as shown on the left of Figure. 3.4).

Figure 3.3 shows the structure of the current robot. It consists of two arms, an inner arm and an outer arm, and two joints providing 2-degrees-of-freedom mobility. At the end of the inner arm, the microphones are fixed. Due to the kinematic equations, the microphones are constrained on the surface of a sphere with a radius of 1 meter and centered at the machine's center.

The grid is predefined by an optimization algorithm, which makes sure every point on the grid represents an equal area. The whole system was initially designed for sound intensity and sound power measurement. Equal-area scheme helps to interpret the sound intensity map and simplifies the calculation of sound power.

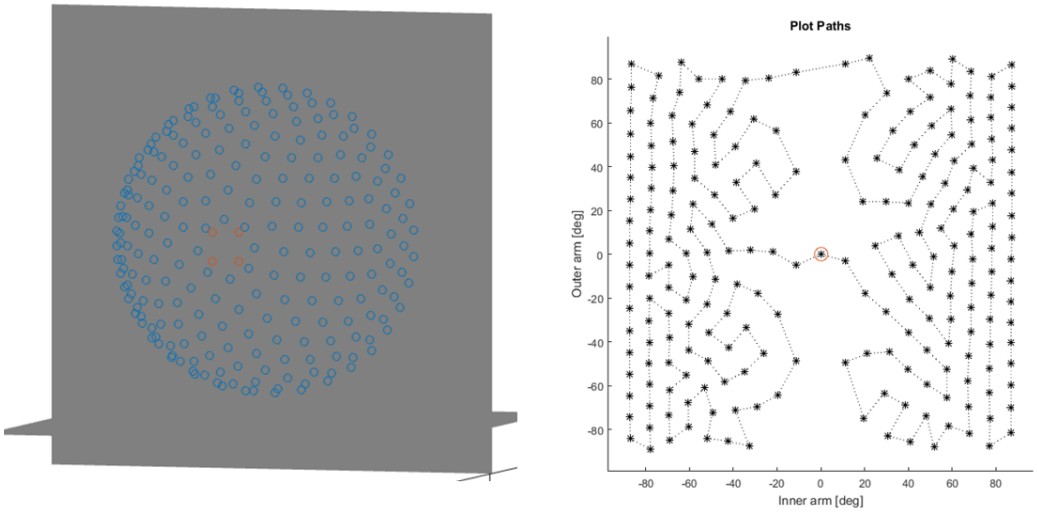

Fig. 3.4. 225-Point Grid and Optimized Path

Once all the measurement locations are determined, an algorithm is applied to find the fastest route. This problem is well-known as the traveling-salesman problem: given a number of cities (vertices), roads (edges) and corresponding traveling time (weighting functions), the objective is to find a path visiting each city exactly once and finishing at the starting city and minimizing the total time cost. In this case, vertices are 2-dimensional coordinates containing the inner and outer motor angles; and edges are all the 2-combination of the total points. For an n-point grid, there are $n^2 - n$ unique edges, and $(n-1)!$ possible paths starting from a fixed vertex. Two motors of the robots move independently and simultaneously. The weighting function is the greater value of the inner motor and outer motor's traveling time. The traveling-salesman problem is an NP problem, i.e. there is no polynomial time algorithm proven so far but any given solution can be verified in polynomial time. In other words, even with currently the fastest algorithm, the computational time increases exponentially with the number of vertices. Fortunately, the number of measurement locations (vertices) needed is not too big and the fastest route only needs to be solved once. The found vertices in the fastest path will be saved to a file in order. Figure 3.4 shows a 225-point grid, which is the most frequently used one, and the fastest route determined. Every time the robot control program reads the grid file and controls the robot arm go through all the locations following the given order.

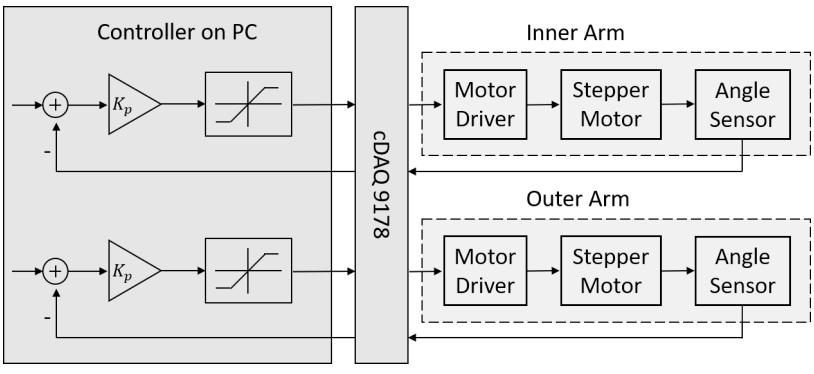

Fig. 3.5. Block Diagram of Robot Angle Control

3.1.3 Controls and Data Acquisition

The independent position control of two robot joints was implemented utilizing a computer, a National Instruments (NI) cDAQ-9178 chassis, two stepper motors, two stepper motor drivers, two motor brakes, two planetary gears, two non-contact-type angle sensors, and their corresponding NI input/output modules. Figure 3.5 illustrates the angle control structure. Data gathered from the angle sensors is sent to a computer via the interface of the NI cDAQ-9178. On the computer, a proportional control with saturation was implemented based on angle sensor feedback. The purpose of saturation was to limit rotation speed, thus maintaining sufficient stepper motor torque for the robotic arm. The computer synthesizes and transmits control inputs to the stepper motor drivers via the NI cDAQ-9178 again.

Although the control program of the robot before the investigation of this thesis worked well, it was not optimal. The controller designer Kim intentionally designed a logic that made the arms move slowly as they reach their commanded angles to help stabilize the structures. A side-effect was, it took averagely 2 to 3 seconds for the arms to move from one point to another, but 7 and 12 seconds for each arm to converge. After tuning the parameters inside the controller, the speed of the both arms are increased the convergence times for the inner arm and the outer arm were reduced to 6 seconds and 3 seconds, without sacrificing the stability. As shown in Figure 3.6, the final speed profile of the arms has relatively high peak speed and a smooth slowing down stage, which effectively prevented shaking of the structures according to in-field observations. The statistics obtained from this studied were absorbed into the optimization objective for the traveling-salesman problem. The weighting function used to be only dependent on the angular distance and was then changed to the total time cost from one point to another, including a varying traveling time and a constant converging time. By making these two changes, the measurement time for a 225-point hemi-spherical grid is reduced to 37 minutes. Compared with the previous cost of 1 hour for a 199-point grid, the speed of the system was improved by 54%.

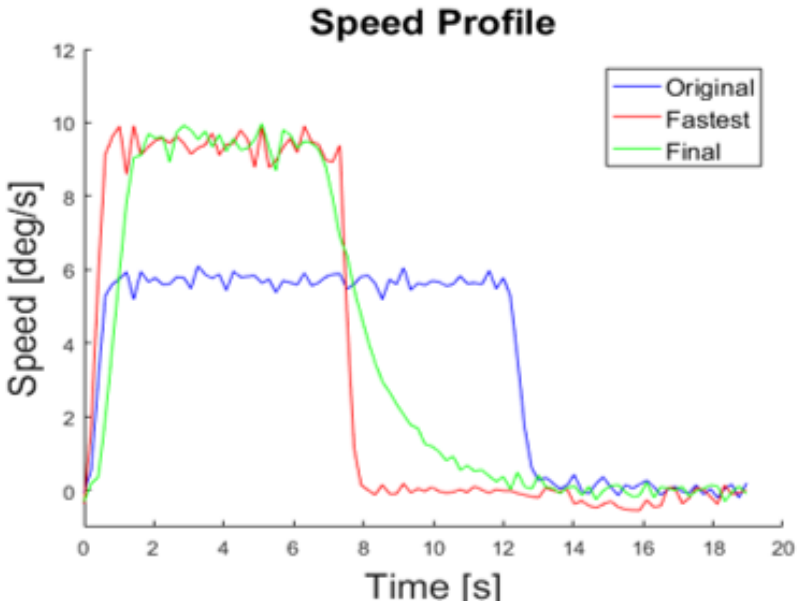

Fig. 3.6. Speed Profile of Robot Controller Tuning

Figure 3.7 presents an overview of all the inputs and outputs via NI cDAQ-9178. The chassis is not only used for the robot control, but also functions as the data acquisition interface of the acoustical and thermal measurements. Three microphones are connected to module NI-9134 and sampled at 51.2 kHz. On the same NI-9134 module, there is another signal recorded besides the three microphones, which is the encoder signal generated from an optical sensor. That is the key to the synthetic array, and details will be explained in Section 3.3. In the post-processing, the air density and speed of sound are required. Both of them are the function of temperature; thus, the temperature in the chamber room is measured by a thermocouple and sampled by the module NI-9211.

3.1.4 Hydraulic Setup

Figure 3.8 shows the hydraulic circuit of the test rig and Table 3.5 lists the corresponding sensors. The whole system was set up in such a way that satisfies the ISO 4409 (Standard 2007). It has to be pointed out that, unlike the acoustical environ-

Table 3.3.
Robot Control Elements (Kalbfleisch et al. 2016)

Stepper Motors	Anaheim 17Y and 23Y
Stepper Motor Drivers	Anaheim MBC 25081TB
Motor Brakes	Anaheim BRK 12H
Planetary Gears	Anaheim GBPN 0402 and 0602
Angle Sensors	Contelec Vert-X22 and Vert-X 31E

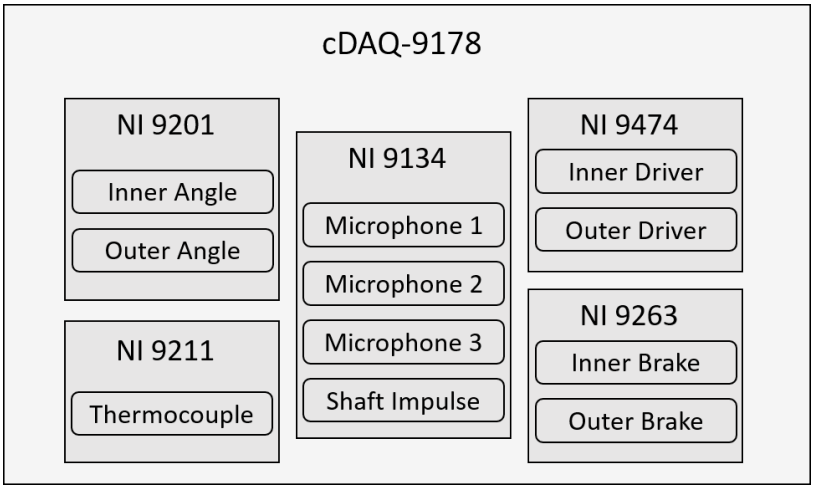

Fig. 3.7. Signals through NI cDAQ-9178

Table 3.4.
Data Acquisition Modules

NI cDAQ-9178	8-slot USB chassis
NI 9234	4-channel analog in, ±5V, 24 bit, $f_{s,max} = 51.2$ kHz
NI 9201	8-channel analog in, ±10V, 12 bit, $f_{s,max} = 500$ kHz
NI 9211	4-channel thermocouple in, ±80mV, 24 Bit
NI 9263	4-channel analog out, ±10V, 16 bit, 100 kS/s/ch
NI 9474	8-channel digital out, 5V–30V, update rate: 1 μs

ment and robotic arm, the hydraulic setup usually changes with different machines. This circuit is only for an open circuit pump, which is also the one used for the later case study. Open circuit means that the inlet of the pump is connected to a tank. To avoid cavitation, the tank is pressurized by air. The operating load is set by the pressure relief valve connected to the outlet of the pump. Sensors A1 - A7 are mainly for monitoring the state of the system because they are not fast enough to catch the high-frequency physical phenomena. Data collected by A13, A14, and A15 are used to represent the noise sources. They are piezoelectric type pressure sensors, which are able to capture the high-frequency pressure change. A13 and A14 measure the inlet and outlet pressure ripple, respectively; they are expected to correlate the FBN source. A15 is hidden behind the confidential block. It measures the pressure ripple of a cylinder actuator, which controls the swash plate angle. Because the swash plate moments must be balanced by the control cylinder, the pressure inside the control cylinder is expected to correlate the SBN source.

Table 3.5.
Fluid Power Sensor List (Kalbfleisch 2018)

A1, A2, A3	Omega Type K (Ni-Cr), −200°C +850°C
A4	Hydac 4745, strain gauge type; 0 – 400bar
A5	Wika S-10, piezoresistive type, 0 – 400bar
A6	VSE VS4 GPO 12V, gear type, 1 – 250 LPM
A7	VSE VS1 GPO 12V, gear type, 0.05 – 80 LPM
A8, A9	HBM T30FNA, $M_{max} = 500$ Nm, $n_{max} = 3000$ RPM
A13, A14, A15	Kistler 603B, piezoelectric type, range: 0 – 1000 bar

3.2 Periodicity Assumption

Although the robot captures the spatial information of the sound field, it is not able to apply microphone array processing, because all the measurements are taken

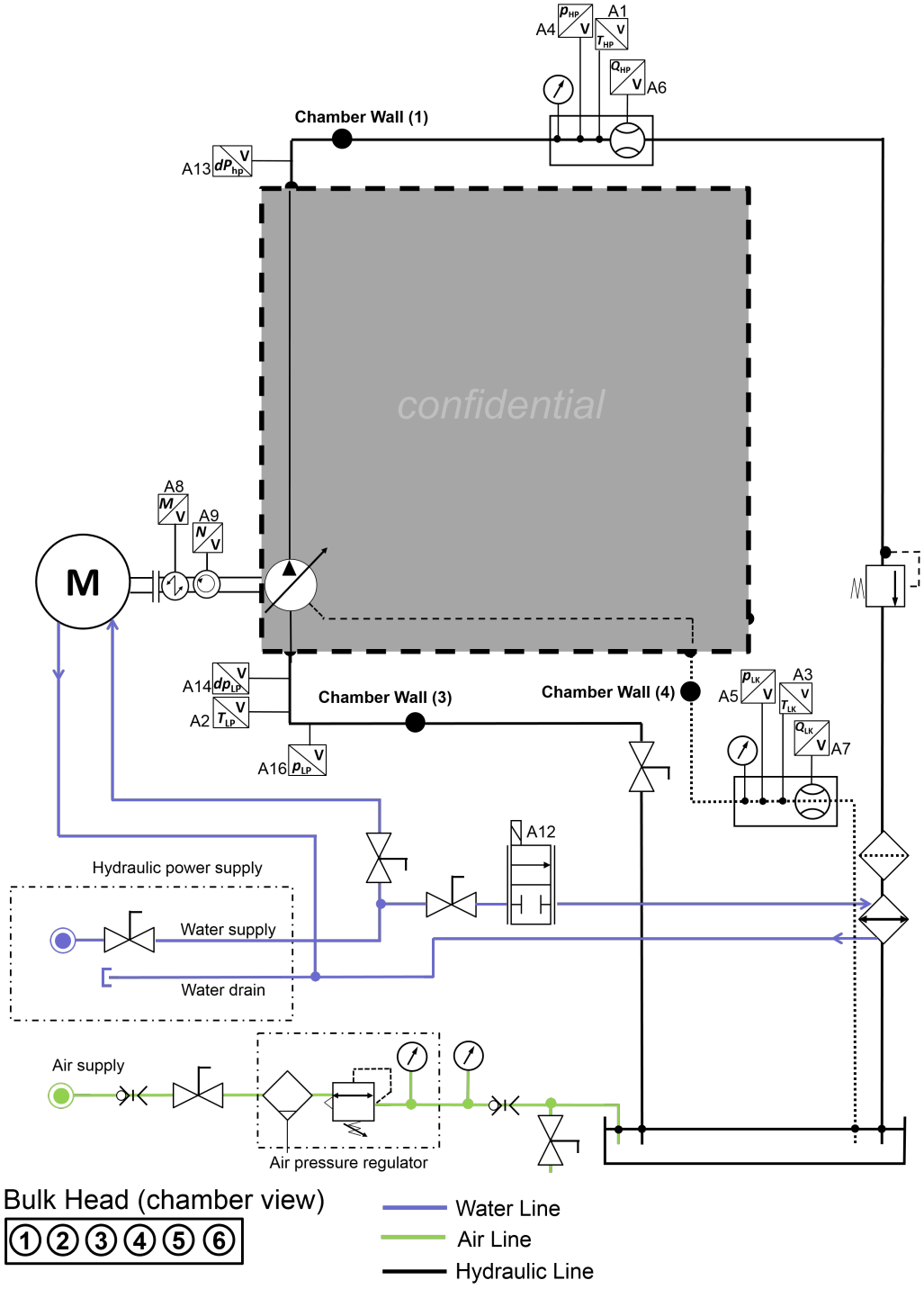

Fig. 3.8. Hydraulic Circuit of Test Rig

sequentially instead of simultaneously. On the one hand, the sound field characteristics might change over time. On the other hand, even if the sound field is steady, the relative phase information is still missing.

This section will use the axial piston machine as an example to show that under steady-state the idealized model would generate periodic noise sources. Along with the assumption of invariant structural response and radiation properties, the perceived sound signals are expected to be periodic. To avoid confusion, the periodicity mentioned here is defined as: (1) the time it takes for a single shaft revolution remains a constant, and (2) what happens in a shaft revolution keeps happening in every shaft revolution, repeatedly.

Technically, to satisfy the first requirement, the shaft speed doesn't necessarily have to be constant, it only needs to be periodic with period T, where T is the time for one revolution rotation. The second requirement, in essence, is equivalent to a steady-state. To establish a steady-state, the system needs to be operated under constant load, constant displacement, and constant shaft speed until the thermal equilibrium is reached. By setting constant shaft speed, the first requirement is satisfied automatically. To summarize, all the assumptions made include:

a. FBN and SBN contribute most of the noise

b. Under steady-state the noise sources of FBN and SBN are periodic

c. Steady-state or "quasi-steady-state" is established during the measurements

d. The structural response and radiation properties don't change

3.2.1 Noise Source Model of Swash Plate Type Machine

The primary purpose of a positive displacement machine is to generate flow to do useful work. Axial piston machines are driven by a rotary mover. This type of input implies there can exist some type of periodic behaviors of the system. In piston machines, the fluid displacement is achieved by the reciprocating motion of the

pistons, the instantaneous flow rate determined by these motions is called kinematic flow rate, Q_{kin}:

$$\begin{aligned} Q_{kin} = \sum_{i=1}^{z} Q_{kin,i} &= \sum_{i=1}^{z} v_{k,i} \cdot A_K \\ &= \sum_{i=1}^{z} \omega \cdot R_b \cdot \tan(\beta) \cdot \sin(\varphi_i) \cdot A_K. \end{aligned} \tag{3.1}$$

Under steady-state, ω, R_b, β, and A_K are all constant, the only varying part is angular position of the piston φ_i. The sinusoidal function makes the speed of the pistons and the flow periodically changes with the angular positions of pistons. At constant shaft speed, it is also equivalent to periodic with time. For simplicity, the leakages, fluid compression, and cross-porting are ignored at this stage. Therefore, the actual flow rate should equal the flow rate caused by kinematics. At the same time, the fluid flows through two ports is also governed by the orifice equation,

$$Q = \alpha A \sqrt{\frac{2|\Delta p|}{\rho}} sgn(\Delta p) \tag{3.2}$$

where α is a coefficient, A is minimum cross-sectional area perpendicular to a streamline, ρ is the fluid density and Δp is the pressure difference between the two sides of the orifice. When observing a single displacement chamber, the opening areas to the ports are only functions of the angular position. Assuming the fluid properties are constant, the minimum cross-sectional area A can also be considered as periodic with shaft rotation. Consequently, to follow the periodic kinematic flow rate, the pressure difference, Δp, must be periodic. If the inlet and outlet pressure are constant (or periodic), the chamber pressure is periodic. This is the general logic for the periodicity of the system.

Now a more general model developed by Kalbfleisch, in which fluid compression and cross-porting are included, is introduced (Kalbfleisch 2015). The control volume of the displacement chamber is shown as Figure 3.9, the pressure inside a displacement chamber is given by the pressure build-up equation:

$$\frac{dp_i}{dt} = \frac{K}{V_i}(Q_{ri} - Q_{SKi} - Q_{SBi} - Q_{SGi} - \frac{dV_i}{dt}) \tag{3.3}$$

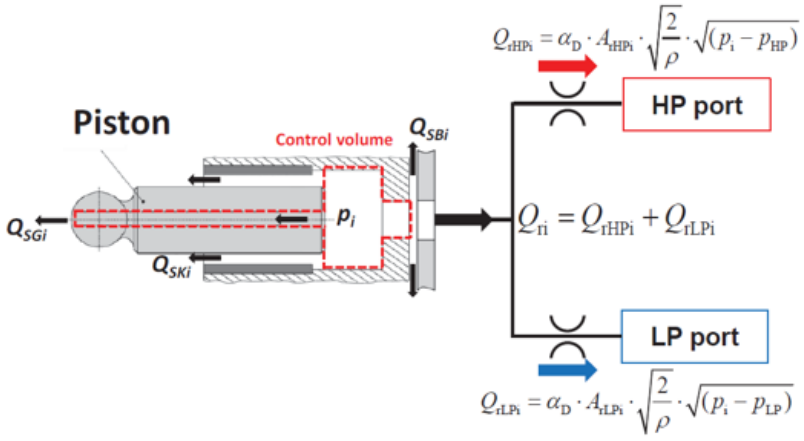

Fig. 3.9. Control Volume of Displacement Chamber (Kim et al. 2014)

where Q_{SKi} represents the leakage flow rate between each piston and cylinder, Q_{SBi} represents the leakage flow rate between the cylinder block and valve plate, and Q_{SGi} the leakage flow rate through the piston bore to the slipper. The three leakage terms are neglected because they are relatively insignificant.

The term $\frac{dV_i}{dt}$ is determined by the piston kinematics: i.e.,

$$\frac{dV_i}{dt} = v_{k,i} A_K = \omega \cdot R_b \cdot \tan(\beta) \cdot \sin(\varphi_i). \tag{3.4}$$

and Q_{ri} is the sum of the flow through the high pressure and low-pressure ports, i.e.

$$Q_{ri} = Q_{rHPi} + Q_{rLPi},$$

Each of the these two term is described by a orifice equation:

$$\begin{aligned} Q_{rHPi} &= \alpha_{DHP} A_{rHPi} \sqrt{\frac{2|p_i - p_{HP}|}{\rho}} sgn(p_i - p_{HP}) \\ Q_{rLPi} &= \alpha_{DLP} A_{rLPi} \sqrt{\frac{2|p_i - p_{LP}|}{\rho}} sgn(p_i - p_{LP}) \end{aligned} \tag{3.5}$$

where p_{HP} and p_{LP} are the two port pressures, which are again described by the pressure build-up equations:

$$\begin{aligned} \frac{dp_{LP}}{dt} &= \frac{K}{V_{LP}}(Q_1 - Q_{rLP}) \\ \frac{dp_{HP}}{dt} &= \frac{K}{V_{HP}}(Q_{rHP} - Q_2) \end{aligned} \tag{3.6}$$

where Q_{rLP} and Q_{rHP} are the summuation of all the individual flows of all the displacement chambers to low-pressure and high-pressure port, respectively: i.e.,

$$\begin{aligned} Q_{rLP} &= \sum_{i=1}^{z} Q_{rLPi} \\ Q_{rHP} &= \sum_{i=1}^{z} Q_{rHPi} \end{aligned} \tag{3.7}$$

and Q_1 and Q_2 are the entering and the exiting flows of the axial piston machine, given by:

$$\begin{aligned} Q_1 &= \alpha_{DHP} A_{rLPi} \sqrt{\frac{2|p_1 - p_{LP}|}{\rho}} sgn(p_1 - p_{LP}) \\ Q_2 &= \alpha_{DLP} A_{rHPi} \sqrt{\frac{2|p_2 - p_{HP}|}{\rho}} sgn(p_2 - p_{HP}) \end{aligned} \tag{3.8}$$

where p_1 and p_2 are two pressure sources. All the cross-sectional areas in the orifice equations above are determined relying on another software called Automated Valve-plate Area Search (AVAS), which caluclates the areas based on the CAD geometry of the valve plate and computational fluid dynamics (Ivantysynova et al. 2004).

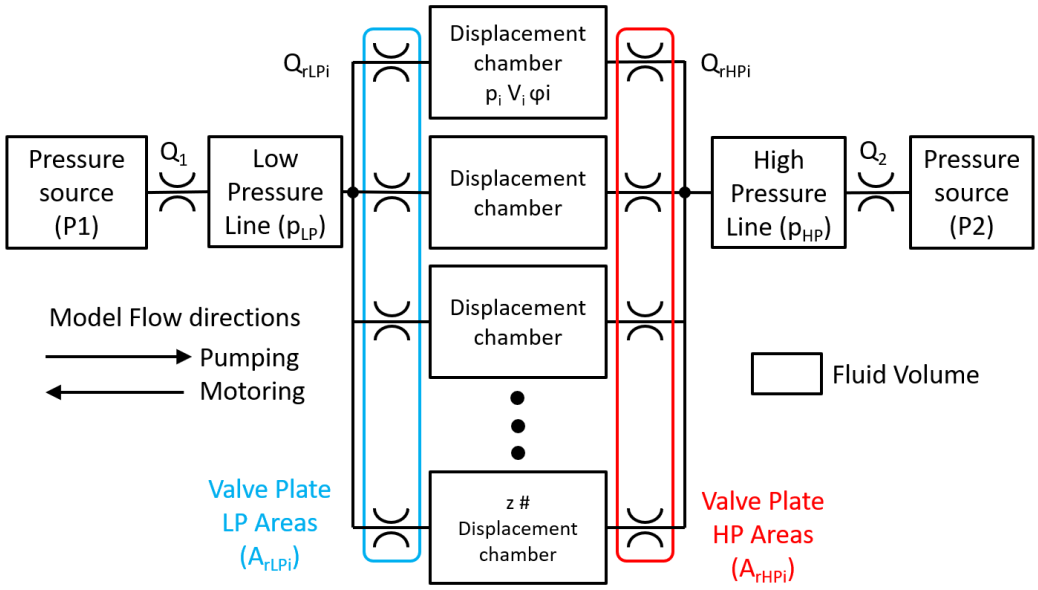

Fig. 3.10. Structure of Pressure Module (Kalbfleisch 2015)

Because of the complexity of the system, it is hard to perform a rigorous mathematical proof or even describe how periodicity is eventually established. Instead, a simulation was run on a numerical software based on the theories introduced above, called Pressure Module. The structure of the simulation model is shown as Figure. 3.10. Figure 3.11 presents simulation results for a 44 cc open-circuit unit operated under 2400 rpm, 280 bar, and 90% displacement. The sub-figures on top illustrate the swash plate moments M_x and p_{HP} in the first 8 revolutions. They clearly show that after the transient stage at the beginning, where the steady-state has not been established, both M_x and p_{HP} become periodic. The bottom sub-figures plot M_x and p_{HP} in 16 revolutions on top of each other. They are too close to distinguish any difference such that only one curves seemingly exists on each graph. These simulation results demonstrate that the periodicity exists in the idealized axial piston machine model.

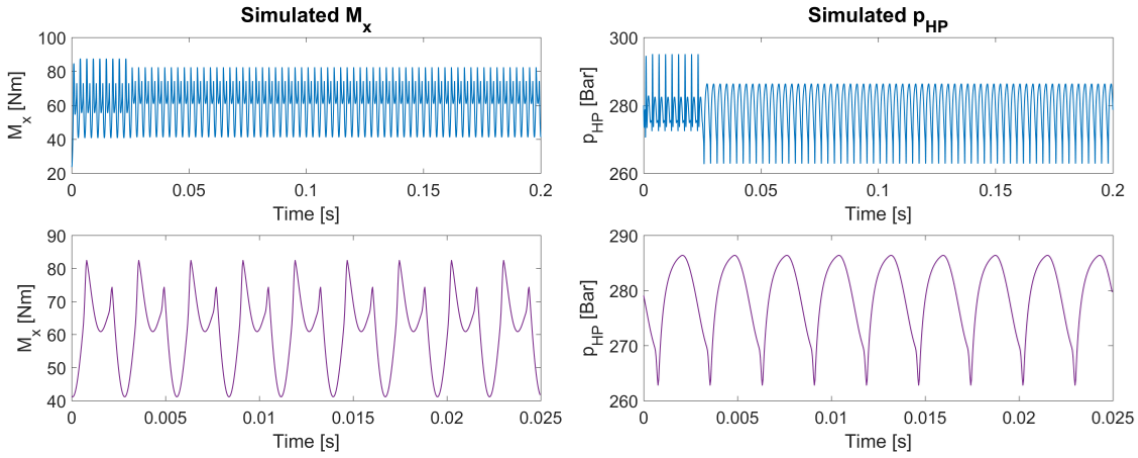

Fig. 3.11. Simulated Noise Sources

Now that the periodicity is observed from an idealized model, what crucial in practice is to guarantee that the steady-state or quasi-steady-state is established. The key factors include constant load, constant displacement, constant shaft speed, and constant oil temperature. As presented previously, in Maha's noise test rig, the

load is set by a relief valve, which should vary only in a relatively small range. For variable displacement axial piston machines, the swash plate angle can potentially change slightly due to pressure forces. This effect should also be insignificant because a well-designed displacement control system should account for it. The shaft is driven by an electric motor at constant speed. Although the torque varies within a revolution in theory, Horn showed that the speed variation is insignificant because the inertia of an electric motor is usually large (Horn 2018). Finally, the inlet oil temperature is set at 50 °C and controlled by a cooling system with ±0.1°C error.

3.3 Synchronization

With the periodicity assumption, measurements taken sequentially can be synchronized to achieve the equivalent effect of a snapshot. Before explaining the synchronization technique used for the synthetic array, a conventional approach using reference microphones is reviewed first.

3.3.1 Available Non-synchronous Array Approaches

The performance of a microphone array largely depends on the number and density of array elements, but adding actual sensor elements brings is a financial burden. Therefore, prior to this work, acousticians have developed various approaches to deal with non-synchronous measurements in microphone array processings. A real microphone array moves sequentially to take measurements and form a larger array. This method is referred to as the sub-array method or scan-based method.

For these approaches, assumptions are still required, although it is not as strict as the one made for this work. The conventional method requires the stationarity and coherence of the sound field. Hald proposed a solution that no longer requires this assumption by using multiple reference microphones (Hald 1989). In the cases where the sound field is not totally stationary, solutions have also been developed with a new assumption of invariant sources' directivity (Kwon, Kim & Bolton 2003, Lee &

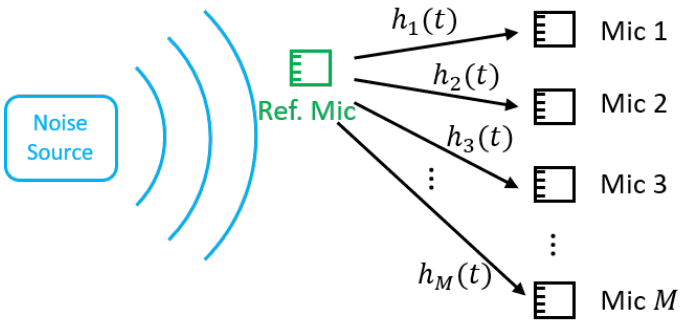

Fig. 3.12. Diagram of Reference Microphone Approach

Bolton 2006). For simplicity, only the method for the stationary and coherent field is introduced.

Once stationarity is assumed, the only missing information is the relative phase among the array microphones. The solution is to put a reference microphone in the sound field and treating the signals perceived by the reference microphone as the input or source. If the sound field is coherent, all the signals measured on the array can be written as this input convolved with an unknown path function,

$$y_i(t) = x(t) * h_i(t) \tag{3.9}$$

where $y_i(t)$ denotes the measured signal on the i-th microphone, $x(t)$ denotes the signal perceived by the reference microphone, and $h_i(t)$ is the path function. Applying Fourier transform and its property (both will be introduced in Chapter 4) yields

$$Y_i(\omega) = X(\omega)H_i(\omega) \tag{3.10}$$

The part of $X(\omega)$ is the same for all the array microphones. Thus, what needs to be determined is the $H_i(\omega)$. The application of Fourier transform to the cross-correlation of $x(t)$ and $y_i(t)$ yields,

$$S_{xy,i}(\omega) = H_i(\omega)S_{xx}(\omega) \tag{3.11}$$

Therefore,

$$Y_i(\omega) = \frac{S_{xy}(\omega)}{S_{xx}(\omega)}X(\omega) \tag{3.12}$$

This method can theoretically be applied for the robotic measurements. The practical constraint is there is not an extra microphone available without taking the 3-microphone probe apart. Even taking it apart, there is no guarantee that two reference microphones are enough for the number of incoherent sources.

Recently, methods without using reference microphones have also been proposed. Nejade developed a reference-less method based on the pressure-velocity type intensity probes (Nejade 2014). Another reference-less method proposed by Antoni, Yu, and Leclére are based on assumptions of stationarity and coherence (Antoni, Liang & Leclère 2015). It has been implemented on beamforming (Yu, Jiang, Antoni, Leclère & Wu 2018) and acoustical holography (Yu, Antoni, Jérôme & Leclère 2014, Yu, Antoni & Leclère 2016, Yu, Antoni, Leclère & Jiang 2017) to estimate the sound quadratic properties (e.g. sound intensity, sound power, quadratic flux).

3.3.2 Synchronization by Encoder

Thanks to the property of periodicity, Kalbfleisch designed and installed a device to achieve synchronization. The general idea is to segment all the measured signals by periods, which correspond to signals generated in shaft revolutions with a fixed physical starting point. Figure 3.13 illustrates the design of this device. An encoder signal is generated by an optical sensor, which points to the rotation shaft. On the shaft is attached a strip of reflective tape. When the optical sensor points on the non-reflective metal, a high voltage is generated; while the optical pointer is on the reflective tape, a low voltage is generated. Consequently, as the electric motor rotates at constant speed, a square wave is generated periodically. This square wave is recorded in parallel with the other sensors' measurements at the same sampling rate, just as shown in Figure 3.7. The edges of the square wave can then be able to used to determine the starting and ending points of the shaft revolutions, as shown in Figure 3.14.

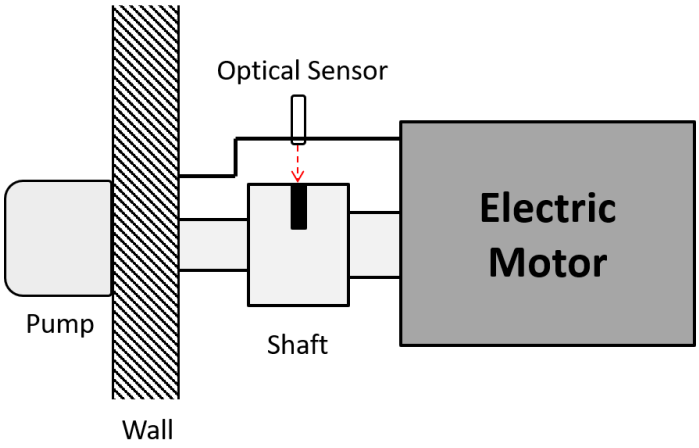

Fig. 3.13. Conceptual Diagram of Optical Shaft Encoder

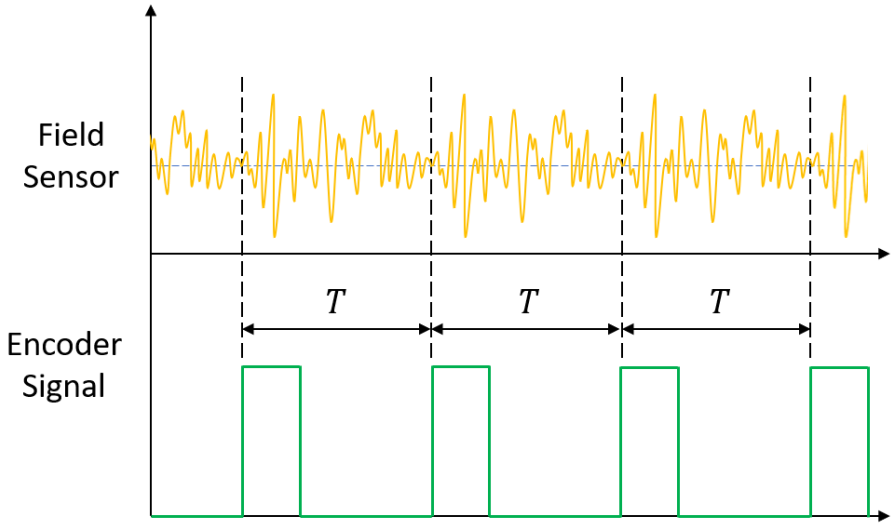

Fig. 3.14. Synchronization with Encoder

The first successful synchronization utilizing this device was achieved by Ding (Ding, Ivantysynova & Kalbfleisch 2016). The time-synchronous sound field videos on the measurement sphere were created and presented on ASME/BATH 2016 Symposium on Fluid Power & Motion Control. This novel visualization technique drew much attention and led to interesting discussions. It was pointed out that this equiv-

alent effect of a snapshot was similar to an "acoustic camera". Inspired by that observation, the concept of a virtual microphone array emerged and led to the investigation of this thesis work.

Time-synchronous Averaging

At each measurement point, it is not expected that the signal captured in every revolution is exactly identical, because of disturbances of a variety of noises. The signal classification system introduced by Kalbfleisch, Horn and Ivantysynova is applied in this investigation (Kalbfleisch, Horn & Ivantysynova 2018). Based on the forestated assumptions, there must, however exist the periodic component. This periodic component is called the deterministic part, denoted by subscript $(\cdot)_d$. The total measured signal subtracted by the deterministic part is called the residual, denoted by subscript $(\cdot)_r$. The deterministic part can be extracted by averaging the synchronized single-revolution data, and this process is called time synchronous averaging (TSA). Generally, averaging with a fixed time delay T is given by Eq. 3.13

$$y(t) = \frac{1}{N}\sum_{n=0}^{N-1} x(t - nT) \tag{3.13}$$

and has the frequency response given by Eq. 3.14

$$|H(\frac{f}{f_p})| = \frac{1}{N}\frac{\sin(\pi N \frac{f}{f_p})}{\sin(\pi \frac{f}{f_p})} \tag{3.14}$$

where $f_p = 1/T$ (Braun 2011). This has a form of a comb filter, with the main lobes at the integer multiples of f_p. If T happens to be the period for one shaft revolution, then the integer multiples of f_p will be referred to as shaft orders. As a result, the TSA identifies all the contents happening at shaft orders.

In discrete-time signal, the period T determines an expected sequence length for one shaft revolution:

$$\bar{L} = T \cdot f_s = \frac{60}{n} \cdot f_s \tag{3.15}$$

where n is the nominal shaft speed in rpm. However, there is no guarantee that the expected length is an integer. Even in the cases where the expected sequence length

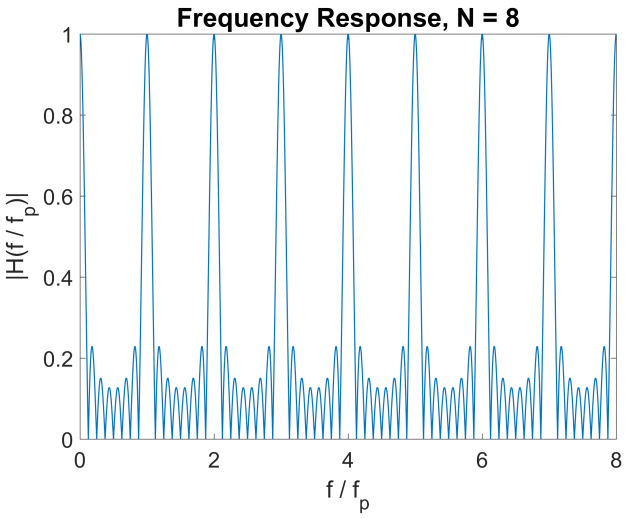

Fig. 3.15. FRF of Comb Filter

is an integer, speed variations can make the sequence length a fraction. In the cases where the expected sequence length is not an integer, the discrete time samples of the encoder signal cannot exactly determine the physical starting point of one shaft revolution, and this effect is called quantization error (Horn 2018, Kalbfleisch, Ding, Baruah, Ivantysynova, Franzoni & Zhang 2019).

This effect brings another issue: averaging of synchronized data cannot be applied when the sequence lengths are not the same. This issue is solved accompanying with the finalization of the theory for the synthetic array (Kalbfleisch et al. 2019): the signals are considered as periodic with shaft angle, instead of time. When the speed is perfectly constant, periodic with time is equivalent to periodic with shaft angle; but once there is any speed variation (not significant enough to affect the steady-state though), this equivalency is no longer true. Therefore, a re-sampling technique using cubic spline interpolation is applied for each synchronized segments (McFadden 1989). Due to the observation from Horn that the instantaneous shaft speed in one shaft revolution is nearly constant, the synchronized segments can be considered as equi-angle sampling from 0 to 360 degrees of the shaft angle with corresponding $\Delta\varphi$. Thus, the interpolation is interpreted as a re-sampling at new angular positions. Figure 3.16

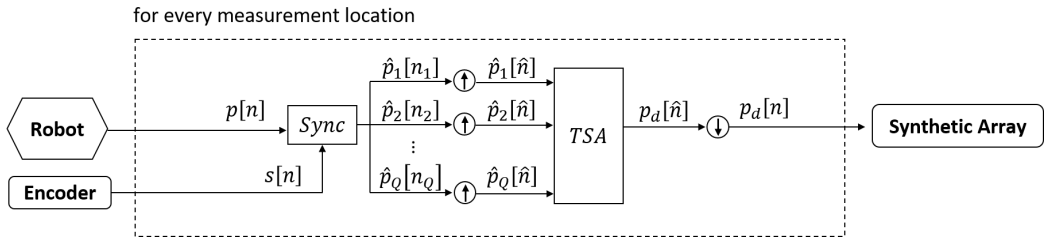

Fig. 3.16. Processes from Robot Measurements to Synthetic Array

summarizes the processes of synthesizing the robot measured data to an equivalent snapshot measured data. For each measurement location, the sensor measured data and its corresponding encoder data are used to determine the signal generated in every single shaft revolution. These synchronized segments are upsampled to the same length, which represents a new angle domain re-sampling with finer resolution, followed by an averaging. The averaged data is then downsampled back to the of expected length $\bar{L}$. If $\bar{L}$ is, unfortunately, a fraction, the averaged data needs to be duplicated q times before downsampling, where $q \in \mathbb{Z}^+$ and it makes $q\bar{L}$ also to be a positive integer. The minimum choice of q is given by

$$q_{min} = \frac{n}{\gcd(60f_s, n)} \tag{3.16}$$

where f_s is the time domain sampling rate, and n is the shaft speed in rpm, and $\gcd(n, m)$ denotes the greatest common divider of integers n and m.

3.3.3 Experimental Validation for Noise Sources

To examine how an actual machine differs from an idealized model and how noise affects the stated assumption, a few experiments were conducted. The data collected from sensors A13, A14 and A15 are used to validate the periodicity assumption on the noise sources. They are all the piezoelectric type pressure sensor, which have the capability to measure the high-frequency pressure variation. A13 and A14 are placed at the inlet and outlet port, respectively. The measured pressure ripples are interpreted as a manifestation of FBN source.

Figure 3.17 shows the deterministic part of p_{LP} and p_{HP}. Each sub-graph contains 9 curves, of which each is the deterministic part of a 4-second long measurement. Every measurement is taken 5 minutes after the previous one. As a result, the time span for these 9 curves is around 40 minutes. Clearly, the deterministic components at different times share almost the same shape with each other. Quantitatively, the linear correlation coefficient among the $p_{LP,d}$ is between 0.9842 and 0.9951, and the linear correlation coefficient among the $p_{HP,d}$ is between 0.9998 and 1.000. These results prove that within an acceptable tolerance, the fluid-borne noise source is periodic.

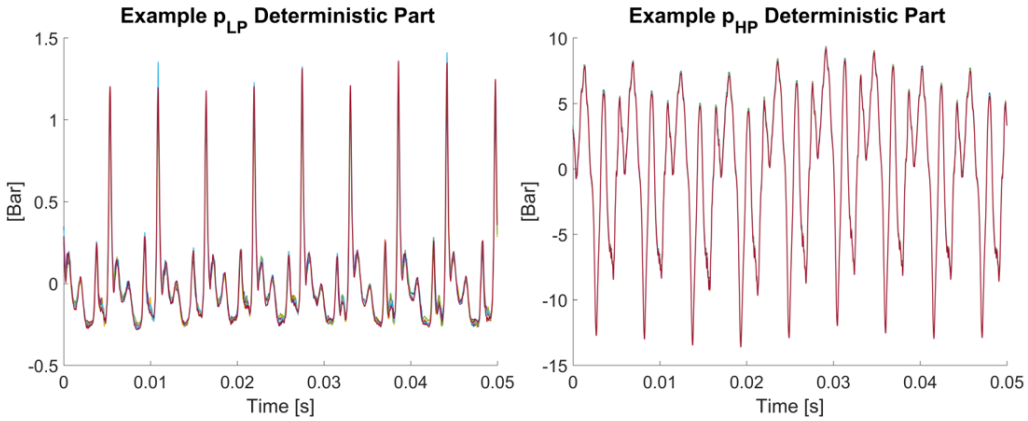

Fig. 3.17. Example Deterministic Part of p_{LP} and p_{HP}

The third piezoelectric pressure sensor measures the control cylinder pressure, which is hidden behind the confidential block on Figure 3.8. Because the forces exerted on the swash plate must be balanced by the control cylinder, the pressure inside the control cylinder should correlate with the swash plate moment very well. Measuring with the same duration and delay, Figure 3.18 shows the deterministic component of 8 samples of the control cylinder pressure. The curves show an obvious correlation. Quantitatively, the correlation coefficients among the 8 curves are between 0.9960 and 0.9979. It is safe to conclude that the structure-borne noise source, estimated by the deterministic component, is periodic in this measurement.

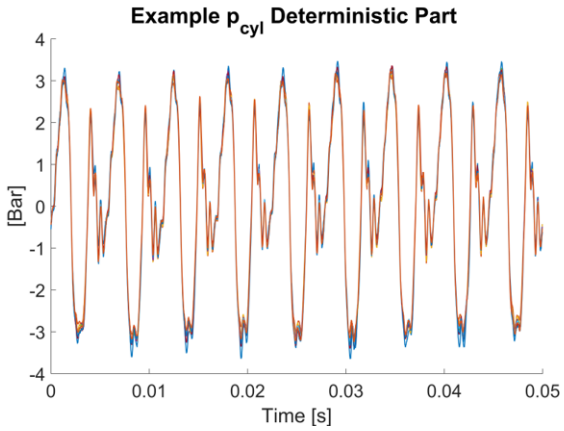

Fig. 3.18. Example Deterministic Part of p_{cyl}

3.3.4 Experimental Validation for Perceived Sound

The periodic sources don't necessarily guarantee that the perceived sound is periodic, because the noise generated by other uncorrelated sources are also perceived and there are structural response function and radiation function playing roles in between. As mentioned before, these two parts are assumed invariant. Therefore, the perceived sound should be nearly periodic and the experimental data is expected to provide some evidence.

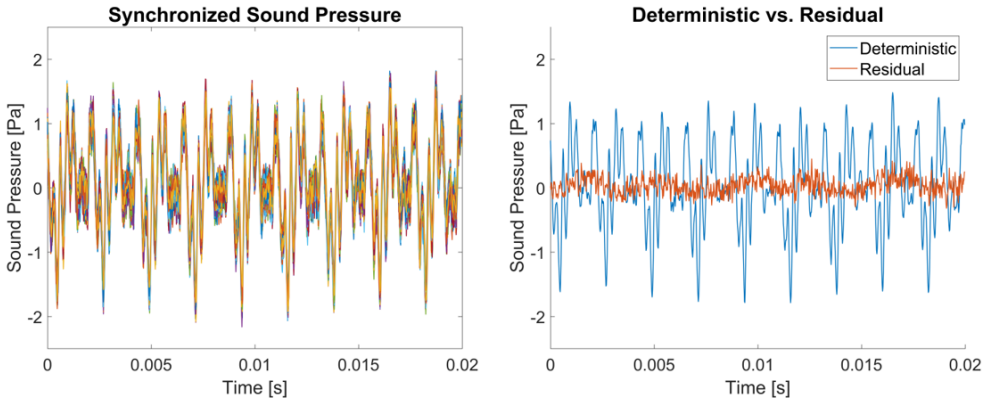

Fig. 3.19. Synchronization for a Good Signal

Randomly picking a 4-second sample taken at one location and segmenting the signal by using the shaft encoder, Figure 3.19 (left) contains 199 the synchronized segments plotted on top of each other. The waveforms of the sound pressure in every shaft revolution match each other very well. The correlation coefficients vary from 0.9445 to 0.9651, which is good. The right sub-figure of Figure 3.19 compares the deterministic part with one of the residuals. The deterministic part is significantly stronger than the residual. The perceived sound in this example can be considered as nearly periodic in this 4-second duration.

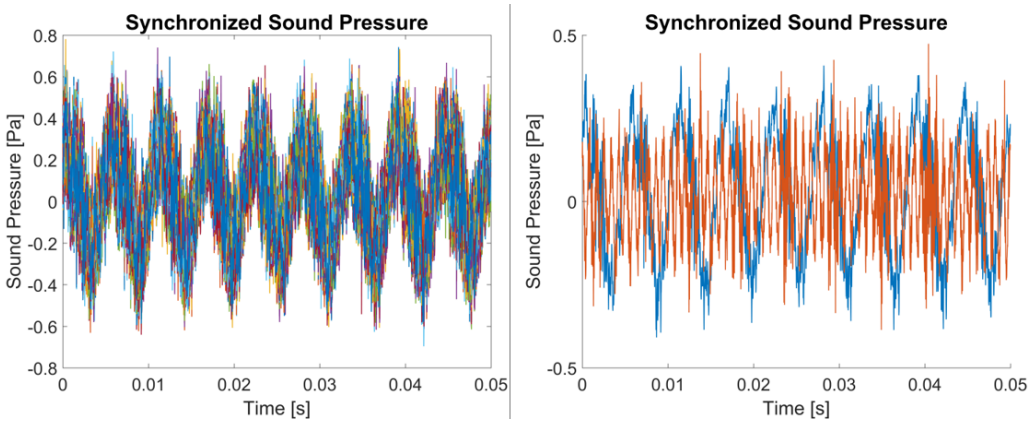

Fig. 3.20. Synchronization for a Bad Signal

Unfortunately, not every case is as clear as this one. Figure 3.20 gives another example, in which the synchronized segments show a non-negligible level of variation from one revolution to another and their correlation coefficients range from 0.7872 to 0.9010. Consequently, the residual level (peak-to-peak) is as large as the deterministic part. This result seemingly challenges the assumptions made. Fortunately, it was defended by another experimental study for the same machine, which involved a reference microphone at a fixed position.

The 3-microphone probe was taken apart and one of them was put at a fixed location under the pump. The reference microphone measured simultaneously with the microphone on the robot. For a 225-point grid, 225 4-second samples are taken at a fixed location with a time span of 40 minutes. For each 4-second sample, TSA is

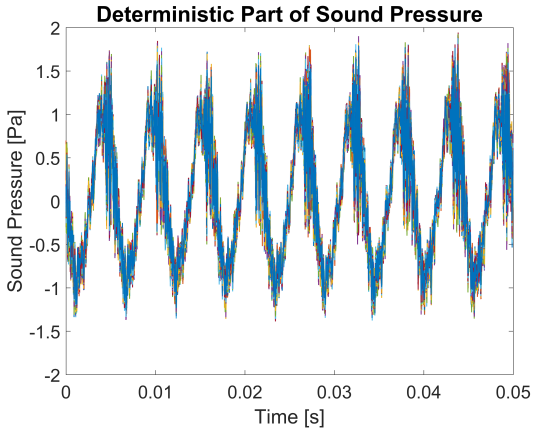

Fig. 3.21. Deterministic Components over 40 Minutes

applied to extract the deterministic part, and Figure 3.21 plots the 225 deterministic components on top of each other. It can be clearly seen that the deterministic part stays consistent over 40 minutes. Quantitatively, the correlation coefficients range from 0.8970 to 0.9933. Even for a signal whose synchronized segments have significant variation, there exists a long-lasting periodic deterministic part; results from cases like the previous one are expected to be even better. Further investigation found out that there is a friction happening once per revolution. This friction resulted in transient noise, which is not periodic with shaft period, and therefore appeared in the residual.

By combining all the information presented above, it is certain to conclude that the periodicity assumption proposed is valid for most axial piston machines, i.e., there does exist a periodic sub-field, which is generated by the two main noise sources under steady-state. Even if in the cases where there exists noise generated by other sources that are aperiodic, the deterministic component can be obtained correctly by using TSA. It has to be pointed out that only extracting the periodic component also becomes the main limitation of this method. If there exists significant aperiodic content, the results obtained from this method can be limited.

4. THEORETICAL PRELIMINARIES

4.1 Fourier Analysis

4.1.1 Fourier Series

Consider a signal $x(t)$ defined in a finite length time interval $[-\frac{T}{2}\frac{T}{2}]$. If $x(t)$ satisfies the Dirichlet condition, it can be decomposed into a series of sinusoidal functions. Such decomposition is called the Fourier series representation of $x(t)$, expressed as:

$$x(t) = \sum_{k=-\infty}^{\infty} a_k e^{jk\omega_0 t} = \sum_{k=-\infty}^{\infty} a_k e^{jk\frac{2\pi}{T}t} \tag{4.1}$$

where $k \in \mathbb{Z}$, a_k is called Fourier series coefficient, and ω_0 is called the fundamental frequency. The most intuitive interpretation of the Fourier series is a projection from the time domain to the frequency domain.

The essential property of the Fourier series is the orthogonality of sinusoidal functions: i.e.,

$$\frac{1}{T}\int_{-\frac{T}{2}}^{+\frac{T}{2}} e^{jk\omega_0 t}e^{-jl\omega_0 t}dt = \delta_{kl} = \begin{cases} 0, & k \neq l \\ 1, & k = l \end{cases} \tag{4.2}$$

Because of orthogonality, the Fourier series coefficients can be determined by computing the inner product between $x(t)$ and Fourier basis $e^{jk\omega_0 t}$, i.e.,

$$a_k = \frac{1}{T}\int_{-\frac{T}{2}}^{+\frac{T}{2}} x(t)e^{-jk\omega_0 t}dt = \frac{1}{T}\int_{-\frac{T}{2}}^{+\frac{T}{2}} x(t)e^{-jk\frac{2\pi}{T}t}dt \tag{4.3}$$

Eq. 4.3 is called analysis equation, and Eq. 4.1 is called the synthesis equation. In addition, orthogonality also induces the Parseval's relation:

$$\frac{1}{T}\int_{-\frac{T}{2}}^{+\frac{T}{2}} |x(t)|^2 dt = \sum_{k=-\infty}^{\infty} |a_k|^2 \tag{4.4}$$

The left side of Eq. 4.4 is referred to as the signal power. If a signal $x(t)$ is defined in $(-\infty, \infty)$, and is periodic with period T, the Fourier series still applies, as long as the Dirichlet condition is satisfied in every period.

Besides continuous time signals, discrete time signals can also be decomposed into a series of discrete sinusoidal functions. Consider a discrete signal with length L: its Fourier series representation is given by:

$$x[n] = \sum_{k=0}^{L-1} a_k e^{jk\omega_0 n} = \sum_{k=0}^{L-1} a_k e^{jk\frac{2\pi}{L}n} \tag{4.5}$$

where a_k is the Fourier series coefficient, and ω_0 is called the fundamental frequency. Here, $k = 0, 1, ..., L-1$, because the discrete sinusoidal function is only unique over the interval $[-\pi, \pi)$ or $[0, 2\pi)$: e.g, $e^{jk\frac{2\pi}{L}n} = e^{j(k+nL)\frac{2\pi}{L}n}$. Therefore, the Fourier series representation of a length-L discrete time signal will contain at most L frequency components.

In parallel with the continuous time Fourier series, discrete sinusoidal functions are also orthogonal,

$$\frac{1}{L}\sum_{n=0}^{L-1} e^{j2\pi k\omega_0 n} e^{-j2\pi k'\omega_0 n} = \delta_{kk'} = \begin{cases} 1, & k - k' = 0, \pm L, \pm 2L, ... \\ 0, & \text{otherwise} \end{cases} \tag{4.6}$$

Thus, the analysis equation for the discrete Fourier series is expressed as:

$$a_k = \frac{1}{L}\sum_{n=0}^{L-1} x[n] e^{-j2\pi k\omega_0 n} = \frac{1}{L}\sum_{n=0}^{L-1} x[n] e^{-jk\frac{2\pi}{L}n} \tag{4.7}$$

and not surprisingly, Parseval's relation also holds: i.e.,

$$\frac{1}{L}\sum_{n=0}^{L-1} |x[n]|^2 = \sum_{k=0}^{L-1} |a_k|^2 \tag{4.8}$$

Again, if an infinitely long signal $x[n]$ is periodic with period L, the Fourier series applies.

Furthermore, the Fourier series can be extended to 2-variable functions. For any square-integrable function $x(\theta, \phi)$, where $\theta \in [0, \pi]$, $\phi \in [0, 2\pi)$, its Fourier series representation is

$$x(\theta, \phi) = \sum_{n=0}^{\infty} \sum_{m=-n}^{n} a_{nm} Y_n^m(\theta, \phi) \tag{4.9}$$

where the $Y_n^m(\theta,\phi)$ are called spherical harmonic functions with the expression:

$$Y_n^m(\theta,\phi) \equiv \sqrt{\frac{(2n+1)}{4\pi}\frac{(n-m)!}{(n+m)!}} P_n^m(\cos(\theta))e^{jm\phi} \tag{4.10}$$

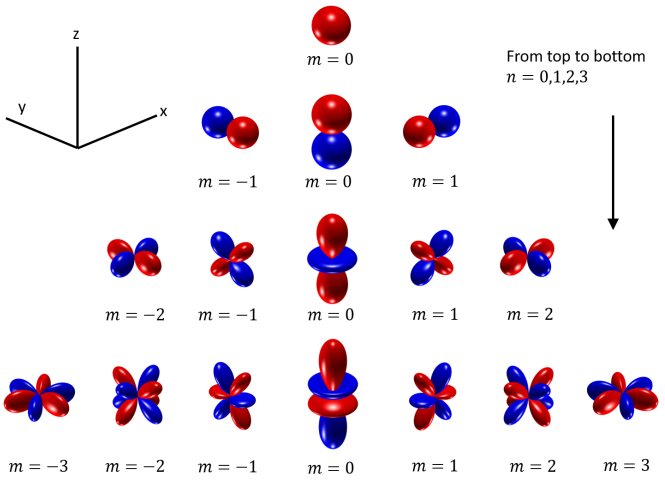

Fig. 4.1. Spherical Harmonic Visualization

Table 4.1.
Illustration of Fig. 4.1

			Y_0^0			
		$\mathrm{Im}\{Y_1^{-1}\}$	Y_1^0	$\mathrm{Re}\{Y_1^1\}$		
	$\mathrm{Im}\{Y_2^{-2}\}$	$\mathrm{Im}\{Y_2^{-1}\}$	Y_2^0	$\mathrm{Re}\{Y_2^1\}$	$\mathrm{Re}\{Y_2^2\}$	
$\mathrm{Im}\{Y_3^{-3}\}$	$\mathrm{Im}\{Y_3^{-2}\}$	$\mathrm{Im}\{Y_3^{-1}\}$	Y_3^0	$\mathrm{Re}\{Y_3^1\}$	$\mathrm{Re}\{Y_3^2\}$	$\mathrm{Re}\{Y_3^3\}$

As for the to single variable Fourier series, $Y_n^m(\theta,\phi)$ also holds to orthogonality: i.e.,

$$\int_0^{2\pi}\int_0^{\pi} Y_n^m(\theta,\phi)[Y_{n'}^{m'}(\theta,\phi)]^* \sin\theta d\theta d\phi = \delta_{nn'}\delta_{mm'} = \begin{cases} 1, & n=n' \text{ and } m=m' \\ 0, & \text{otherwise} \end{cases} \tag{4.11}$$

Consequently, the Fourier series coefficient a_{nm} can be calculated as:

$$a_{nm} = \int_0^{2\pi} \int_0^{\pi} x(\theta, \phi)[Y_n^m(\theta, \phi)]^* \sin\theta d\theta d\phi \tag{4.12}$$

and again the Parseval's relation holds:

$$\int_0^{2\pi} \int_0^{\pi} |x(\theta, \phi)|^2 \sin\theta d\theta d\phi = \sum_{n=0}^{\infty} \sum_{m=-n}^{m} |a_{nm}|^2 \tag{4.13}$$

Eq. 4.12 and Eq. 4.9 are called spherical Fourier transform and its inverse, although they have the exact same essence as the Fourier series and integration is not involved.

Unlike single variable functions, there is not a simple parallel discrete form for the 2-variable Fourier series. Simply discretizing Eq. 4.12 by converting integration to summation yields

$$a_{nm} = \sum_{i=1}^{Q} \alpha_i x(\theta_i, \phi_i)[Y_n^m(\theta_i, \phi_i)]^* \tag{4.14}$$

where Q is the sampling number, and α_i are the weights. Meanwhile, for practical purposes, the synthesis equation sometimes has to be truncated at a finite order N: i.e.,

$$x(\theta, \phi) \simeq \sum_{n=0}^{N} \sum_{m=-n}^{n} a_{nm} Y_n^m(\theta, \phi) \tag{4.15}$$

Since Eq. 4.12 is derived based on orthogonality, for Eq. 4.14 to be correct, the orthogonality must hold after discretization: i.e.,

$$\sum_{i=1}^{Q} \alpha_i Y_n^m(\theta_i, \phi_i)[Y_{n'}^{m'}(\theta_i, \phi_i)]^* = \delta_{nn'}\delta_{mm'} \tag{4.16}$$

must be true for all possible n, n', m and m'. Note that α_i obviously depends on the sampling scheme and not just any arbitrary sampling can find such a α_i that makes Eq. 4.16 always true.

Rafaely presented three common sampling schemes and the corresponding weighting functions that guarantee orthogonality (Rafaely 2015). Equal-angle sampling is a method that has uniformly-spaced angular positions along θ and ϕ. Given the max-

imum truncated order N, the sampling number Q must be $4(N+1)^2$. Under this sampling method, α_i is given by:

$$\alpha_i = \frac{2\pi}{(N+1)^2} \sin\theta_i \sum_{q=0}^{N} \frac{1}{2q+1} \sin\left[2q+1\right]\theta_i \tag{4.17}$$

Another sampling scheme is called Gaussian sampling, which is $2(N+1)$ equal-angle samples along the ϕ direction and $(N+1)$ equal-angle samples along the θ direction. The weights for Gaussian sampling are given by:

$$\alpha_i = \frac{\pi}{N+1} \frac{2(1-\cos^2\theta_i)}{(N+2)^2 P_{N+2}^2(\cos\theta_i)}) \tag{4.18}$$

The last sampling scheme is called uniform sampling. This method requires all the samples to be located at the vertices of a Platonic solid, e.g., the tetrahedron, the octahedron and so forth. Sampling satisfying this condition has a constant weighing function

$$\alpha_i = \frac{4\pi}{Q} \tag{4.19}$$

4.1.2 Fourier Transform

Fourier series only applies on finite length functions or periodic infinite length functions. The Fourier transform extends Fourier analysis to a wider range of functions. Any aperiodic function defined in $(-\infty, \infty)$ can be considered as a periodic function with period $T \to \infty$. As a result, the Fourier series coefficient is then calculated as:

$$a_k = \lim_{T\to\infty} \frac{1}{T} \int_{-\frac{T}{2}}^{\frac{T}{2}} x(t) e^{-jk\omega_0 t} dt \tag{4.20}$$

As long as the integration in Eq. 4.20 is bounded, the Fourier coefficient a_k will be an infinitely small quantity. Therefore, define a more meaningful value:

$$X(\omega) = Ta_k = \int_{-\infty}^{+\infty} x(t) e^{-jk\omega_0 t} dt = \int_{-\infty}^{+\infty} x(t) e^{-j\omega t} dt \tag{4.21}$$

The substitution of Eq. 4.21 into Eq. 4.1 yields

$$x(t) = \frac{1}{T} \sum_{k=-\infty}^{+\infty} X(\omega) e^{j\omega t} = \frac{1}{2\pi} \sum_{k=-\infty}^{+\infty} X(\omega) e^{j\omega t} \omega_0 \tag{4.22}$$

Note that $\omega_0 = \frac{2\pi}{T} \to 0$ as $T \to \infty$, and Eq. 4.22 then becomes:

$$x(t) = \frac{1}{2\pi} \int_{-\infty}^{+\infty} X(\omega) e^{j\omega t} d\omega \tag{4.23}$$

Eq. 4.21 is called the continuous-time Fourier transform (CTFT) or analysis equation, and Eq. 4.23 is called inverse Fourier transform or synthesis equation. Here, $\omega_0 = 0$ means the variable ω becomes continuous, unlike Fourier series. Meanwhile, multiplying by time T in Eq. 4.21 is equivalent to dividing by frequency in the sense of dimension. Thus, what the Fourier transform describes actually is the density of some quantity on the frequency domain.

Hence, denote $\mathcal{F}(\cdot)$ as the Fourier transform operator, thus

$$X(\omega) \equiv \mathcal{F}\big((x(t)\big) \tag{4.24}$$

Naturally, $\mathcal{F}^{-1}$ is denoted to represent the inverse Fourier transform: i.e.,

$$x(t) \equiv \mathcal{F}^{-1}\big((X(\omega)\big) \tag{4.25}$$

Two of the following properties of Fourier transforms are very useful (Oppenheim, Willsky & Nawab 1996). First, Fourier transform is a linear operator, which means

$$\mathcal{F}\big(c_1 \cdot x_1(t) + c_2 \cdot x_2(t)\big) = c_1 \cdot X_1(\omega) + c_2 \cdot X_2(\omega) \tag{4.26}$$

Besides that, another important property is the duality of multiplication and convolution in the time domain and frequency domain, given by Eq. 4.27

$$\begin{aligned} \mathcal{F}\big(x_1(t) \times x_2(t)\big) &= X_1(\omega) * X_2(\omega) \\ \mathcal{F}\big(x_1(t) * x_2(t)\big) &= X_1(\omega) \times X_2(\omega) \end{aligned} \tag{4.27}$$

The Discrete-time Fourier transform (DTFT) is derived by using the same idea of deriving CTFT. It considers a infinitely long sequence and Eq. 4.7 becomes the evaluation of a limit. Eq. 4.29 and Eq. 4.28 give the definitions of DTFT and inverse-DTFT: i.e.,

$$x[n] = \frac{1}{2\pi} \int_{2\pi} X(\omega) e^{j\omega n} d\omega \tag{4.28}$$

$$X(\omega) = \sum_{n=-\infty}^{+\infty} x[n]e^{j\omega n} \tag{4.29}$$

It needs to be pointed out that the range of the frequency domain in DTFT is $[-\pi, \pi)$ or $[0, 2\pi)$. Although Eq. 4.26 and Eq. 4.27 are for the CTFT, the DTFT also holds the same linearity and duality of multiplication and convolution.

Parseval's relation also applies to Fourier transform in both continuous time case and discrete time cases

$$\begin{aligned} \int_{-\infty}^{+\infty} |x(t)|^2 dt &= \frac{1}{2\pi} \int_{-\infty}^{+\infty} |X(\omega)|^2 d\omega \\ \sum_{n=-\infty}^{+\infty} |x[n]|^2 &= \frac{1}{2\pi} \int_{2\pi} |X(\omega)|^2 d\omega \end{aligned} \tag{4.30}$$

4.1.3 Discrete Fourier Transform (DFT)

In practice, the most common case is the discrete frequency representation of a discrete time signal. Although this problem can be handled very well by the discrete-time Fourier series as previously mentioned, people have developed another tool called discrete Fourier transform (DFT) in signal processing. The DFT and inverse discrete Fourier transform (IDFT) are given by Eq. 4.31 and Eq. 4.32: i.e.,

$$X[k] = \sum_{n=0}^{N-1} x[n]e^{-jk\frac{2\pi}{N}n} \tag{4.31}$$

$$x[n] = \frac{1}{N} \sum_{n=0}^{N-1} e^{jk\frac{2\pi}{N}n} \tag{4.32}$$

By comparing Eq. 4.31 and Eq. 4.32 with Eq. 4.7 and Eq. 4.5, it's clear that if $N = L$, the DFT only differs from the discrete-time Fourier series by a factor N (or L). Different meanings of N and L makes the DFT fundamentally different from the discrete-time Fourier series. For the discrete-time Fourier series, there are at most L sinusoidal functions needed because they form a complete basis; but in the DFT there is no limitation for N. The DFT is interpreted as an N-point equi-space discrete sampling on the continuous frequency spectrum (DTFT) of a discrete signal. The

properties of frequency domain sampling turn out to be symmetric to time domain sampling. The frequency representation of discrete time signals is periodic with the period of 2π. Similarly, if treating the DFT as an N-point equi-space sampling on a DTFT from $[-\pi, \pi)$ or $[0, 2\pi)$, the signal it represents in the time domain is an infinitely long periodic signal with the period of N. In discrete time domain sampling, an insufficient sampling rate leads to frequency domain aliasing, which is a well-known fact. In the same way, inadequate frequency domain samples (i.e., insufficient frequency resolution) will lead to time domain aliasing; and if the number of samples exceeds the signal length, L, it will result in extra zeros on the end of the signal (Proakis & Manolakis 2006).

From the perspective of discrete frequency domain sampling, it is intuitive to understand the results of the DFT applied to finite length sinusoidal functions. Let's consider this signal,

$$x[n] = \begin{cases} e^{j\omega_a n}, & n = 0, 1, ..., L-1 \\ 0, & \text{otherwise} \end{cases} \tag{4.33}$$

This signal can be considered as a sinusoidal function multiplied by a rectangular window of length L. As previously mentioned, multiplication in the time domain is equivalent to convolution in the frequency domain. The DTFT of $e^{j\omega_a n}$ is a shifted delta function, i.e., $\delta[n - \omega_a]$; and the DTFT of a rectangular window is a sinc function. A sinc function convolved with a shifted delta function becomes a shifted sinc function, with the central peak at ω_a and nulls at $\omega_a + k2\pi/L$ or $\omega_a + k2\pi/L$ (Fig. 4.2).

Now the N-point equi-space sampling is perfomed on the shifted sinc funtion. Apparently, all the sampling occurs at $k\omega_0$, where $\omega_0 = \frac{2\pi}{N}$ and $k = 0, 1, ..., N-1$. Ideally, the samples should correctly describe the true information about the signal, i.e., it should only have one peak at ω_a with magnitude L. For the DFT to exactly sample at ω_a, the signal frequency ω_a has to be an integer multiple of ω_0. In the luckiest case, where $N = L$, DFT not only samples at the peak but also all the null points, which is the best possible result and is illustrated by the case (a) of Fig. 4.3.

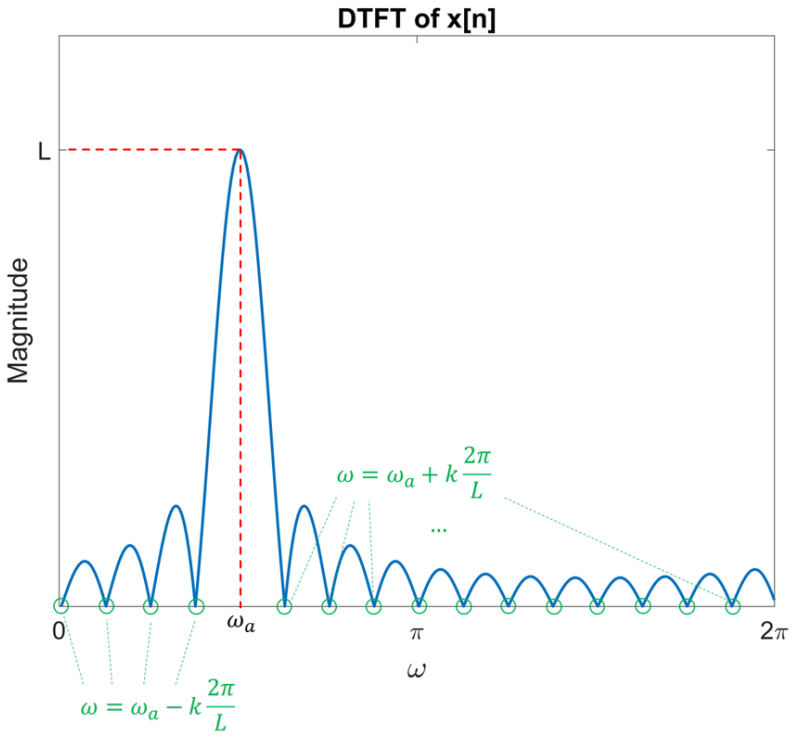

Fig. 4.2. DTFT of $x[n]$

If $N \neq L$, then the DFT can still correctly sample at the true peak location, as long as $\omega_a = k\frac{2\pi}{N}$, but other non-zero values will also be sampled. In other words, the side-lobes will be added. In a worse situation, where ω is not an integer multiple of ω_0, the DFT will definitely not sample at the true peak. In the case (c) of Fig. 4.3, the DFT is not only unable to sample at the peak, but is also deceiving about the true frequency content of the signal. Increasing the sampling number, N, yields a better estimation of the peak but it will still never be able to exactly pick the true peak and eliminate the side-lobes. All these effects can be attributed to the finite-length rectangular window because its DTFT is a sinc function. The phenomenon described above is referred to as spectral-leakage. A common solution is multiplying by another window function, which nulls out the sidelobes caused by the rectangular window.

In practice, the DFT and the IDFT are not computed directly by using Eq. 4.31 and Eq. 4.32, because the computation cost of evaluating of Eq. 4.31 and Eq. 4.32

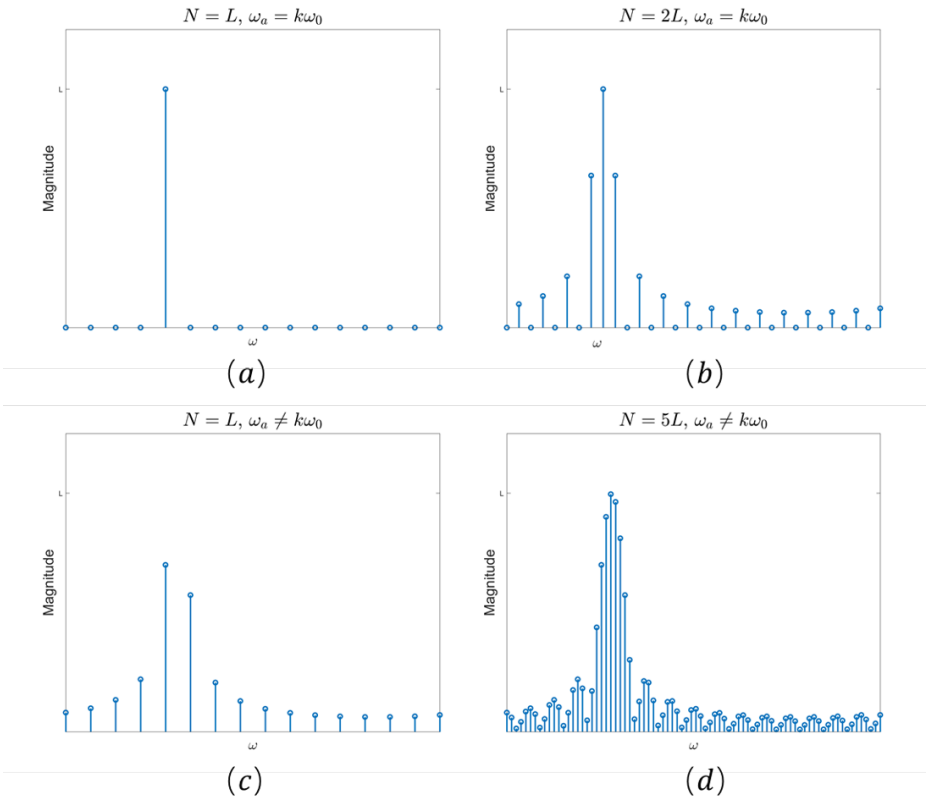

Fig. 4.3. DFT for Different Cases

grows quadratically with the number of DFT, expressed as $\Theta(N^2)$. A class of more efficient algorithms is usually used, called fast Fourier transforms, or FFTs. The FFT utilizes the divide-and-conquer strategy and reduces the algorithm complexity to $\Theta(N \log N)$. As a result, in many contexts, the term FFT is incorrectly used to refer to the DTF.

4.2 Acoustics

4.2.1 Linear Wave Equation

The linear, lossless wave equation for sound pressure propagation in a homogeneous inviscid fluid is given by

$$\nabla^2 p - \frac{1}{c^2}\frac{\partial^2 p}{\partial t^2} = 0 \tag{4.34}$$

where p is sound pressure, c is the speed of sound in the fluid, t is time, and ∇^2 is the Laplacian operator. In the Cartesian coordinate system,

$$\nabla^2 = \frac{\partial^2}{\partial x^2} + \frac{\partial^2}{\partial y^2} + \frac{\partial^2}{\partial z^2} \tag{4.35}$$

Eq. 4.34 is derived from the fluid continuity and another important equation, called the linearized Euler's equation, which describes the relationship between particle velocity and sound pressure:

$$\rho_0 \frac{\partial \boldsymbol{u}}{\partial t} = -\nabla p \tag{4.36}$$

where u is particle velocity, ρ_0 is the equilibrium air density.

Appliction of Fourier transform to Eq. 4.34 gives,

$$\mathcal{F}(\nabla^2 p - \frac{1}{c^2}\frac{\partial^2 p}{\partial t^2}) = 0 \tag{4.37}$$

Because of the linearity of $\mathcal{F}$,

$$\mathcal{F}(\nabla^2 p) - \mathcal{F}(\frac{1}{c^2}\frac{\partial^2 p}{\partial t^2}) = 0 \tag{4.38}$$

Then Eq. 4.38 then can be further simplified to

$$\nabla^2 \hat{p}(\omega) + k^2(\omega)\hat{p}(\omega) = 0 \tag{4.39}$$

where $k = \frac{\omega}{c}$ is called the wave number with units of rad/m, which physically means the spatial frequency. By pre-specifying the frequency, Eq. 4.39 can be expressed in a cleaner form as

$$\nabla^2 p + k^2 p = 0 \tag{4.40}$$

called the Helmholtz equation.

4.2.2 Solutions to Linear Wave Equation

The derivation above shows that Eq. 4.40 is the Fourier transform of Eq. 4.34. The advantage of Eq. 4.40 is it reduces the pressure from a function of space and time (four variables) to a function of just space (three variables), and the solution of Eq. 4.40 will directly yield the solution of 4.34.

Cartesian Coordinate System

In Cartesian coordinates, solving Eq. 4.40 is straightforward. In search of a function with second order derivative that has the same form as itself, it's not hard to think of complex exponentials. Thus, the solution to Eq. 4.40 is given by

$$p = Ae^{j(k_x x + k_y y + k_z z)} \tag{4.41}$$

where A is an arbitrary constant and

$$k^2 = k_x^2 + k_y^2 + k_z^2 \tag{4.42}$$

The vector (k_x, k_y, k_z) describes the direction of wave propagation, and this wave is referred to as a plane wave.

The steady-state pressure distribution in a source-free half space can be expressed as:

$$p(x, y, z) = \frac{1}{4\pi^2} \int_{-\infty}^{+\infty} \int_{-\infty}^{+\infty} P(k_x, k_y) e^{j(k_x x + k_y y + k_z z)} dk_x dk_y \tag{4.43}$$

Spherical Coordinate System

More pages will be devoted to on explaining the solutions in the spherical coordinate system, not only because it requires more manipulation to get the solution, but

also because the method that will later be implemented is based on a spherical wave expansion. Consider a standard spherical coordinate system, where

$$\begin{aligned} x &= r\sin(\theta)\cos(\phi) \\ y &= r\sin(\theta)\sin(\phi) \\ z &= r\cos(\theta) \end{aligned} \tag{4.44}$$

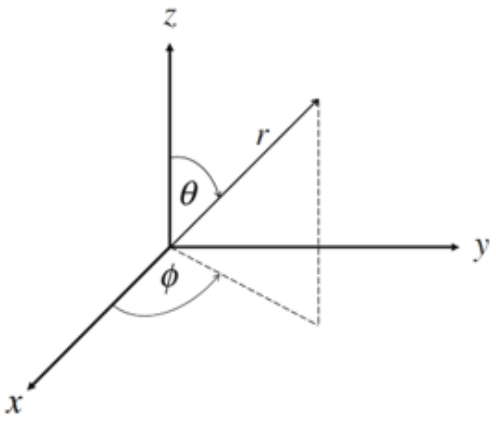

Fig. 4.4. Spherical Coordinate System

In a spherical coordinate system, the operator ∇^2 becomes

$$\nabla^2 = \frac{\partial^2}{\partial r^2} + \frac{2}{r}\frac{\partial}{\partial r} + \frac{1}{r^2\sin\theta}\frac{\partial}{\partial\theta}(\sin\theta\frac{\partial}{\partial\theta}) + \frac{1}{r^2\sin^2\theta}\frac{\partial^2}{\partial\phi^2} \tag{4.45}$$

Substituting Eq. 4.45 into Eq. 4.40 yields

$$\frac{1}{r^2}\frac{\partial}{\partial r}(r^2\frac{\partial p}{\partial r}) + \frac{1}{r^2\sin\theta}\frac{\partial}{\partial\theta}(\sin\theta\frac{\partial p}{\partial\theta}) + \frac{1}{r^2\sin^2\theta}\frac{\partial^2 p}{\partial\phi^2} + k^2 p = 0 \tag{4.46}$$

Eq. 4.46 can be solved by assuming the solution is product of three single-variable functions: i.e.,

$$p(r,\theta,\phi) = R(r)\Theta(\theta)\Phi(\phi) \tag{4.47}$$

Substitution of Eq. 4.47 into Eq. 4.46 followed by simplification yields,

$$\frac{1}{R}\frac{d}{dr}(r^2\frac{dR}{dr}) + k^2r^2 + \frac{1}{\Theta\sin\theta}\frac{d}{d\theta}(\sin\theta\frac{d\Theta}{d\theta}) + \frac{1}{\Phi\sin^2\theta}\frac{d^2\Phi}{d\phi^2} = 0 \tag{4.48}$$

Then Eq. 4.48 can be separated into 3 ordinary differential equations: i.e.,

$$\frac{d^2\Phi}{d\Phi^2} + m^2\Phi = 0 \tag{4.49}$$

$$\frac{1}{\sin\theta}\frac{d}{d\theta}(\sin\theta\frac{d\Theta}{d\theta}) + [n(n+1) - \frac{m^2}{\sin^2\theta}]\Theta = 0 \tag{4.50}$$

$$\frac{1}{r^2}\frac{d}{dr}(r^2\frac{dR}{dr}) + k^2R - \frac{n(n+1)}{r^2}R = 0 \tag{4.51}$$

The two constants m and n are created by separation.

Eq. 4.49 is a simple harmonic oscillator equation, whose solution is simply the sinusoidal functions:

$$\Phi(\phi) = c_1e^{jm\phi} + c_2e^{-jm\phi} \tag{4.52}$$

Let m be an integer, so that all the $e^{jm\phi}$ form a Fourier series basis such that any physically possible $\Phi(\phi)$ can be represented.

To solve Eq. 4.50 needs a transformation on θ. Let $\eta = \cos\theta$,

$$\frac{d}{d\eta}[1-\eta^2)\frac{d\Theta}{d\eta}] + [n(n+1) - \frac{m^2}{1-\eta^2}]\Theta = 0 \tag{4.53}$$

The solutions are then given by Legendre functions of the first and second kinds,

$$\Theta(\theta) = c_3P_n^m(\cos(\theta)) + c_4Q_n^m(\cos(\theta)) \tag{4.54}$$

The functions of the second kind, Q_n^m, are not finite at the poles when $\eta = \pm 1$ so this solution is discarded. The n and m are restricted to be integers, where $n \in \mathbb{Z}^+$ and $-n \leq m \leq n$, otherwise P_n^m diverges or equals 0. For each m, the functions $P_n^m(x)$ form a complete set of orthogonal functions which obeys:

$$\int_{-1}^{1} P_n^m(x)P_{n'}^m(x)dx = \frac{2}{2n+1}\frac{(n+m)!}{(n-m)!}\delta_{nn'} \tag{4.55}$$

The two angular functions $\Phi(\phi)$ and $\Theta(\theta)$ can be conveniently combined into a single function to describe the directional behaviors. Meanwhile, to normalize the integral, a factor depending on the order n and degree m is added, such that a new function that satisfies the wave equation is defined as

$$Y_n^m(\theta,\phi) \equiv \sqrt{\frac{(2n+1)}{4\pi}\frac{(n-m)!}{(n+m)!}}P_n^m(\cos(\theta))e^{jm\phi} \tag{4.56}$$

which is exactly the spherical harmonic function introduced in the Fourier analysis section.

Last, the radial equation, Eq. 4.51, has a solution given by

$$R(r) = c_5 h_n^{(1)}(kr) + c_6 h_n^{(2)}(kr) \tag{4.57}$$

where $h_n^{(1)}$ and $h_n^{(2)}$ are spherical Hankel functions of the first and second kind. $h_n^{(1)}$ represents the outgoing wave, and $h_n^{(2)}$ represents the incoming wave. Their expressions are given by

$$\begin{aligned} h_n^1(x) &= -j(-1)^n x^n (\frac{1}{x}\frac{d}{dx})^n \frac{e^{jx}}{x} \\ h_n^2(x) &= j(-1)^n x^n (\frac{1}{x}\frac{d}{dx})^n \frac{e^{-jx}}{x} \end{aligned} \tag{4.58}$$

The subscript n here is exactly the same order n of the spherical harmonic function. As a result, the spherical Hankel function can be considered as describing the radial behaviors of the spherical harmonic function at order n. The expressions of the spherical Hankel functions are complicated, but what is very helpful is their asymptotic properties:

$$\begin{aligned} h_n^{(1)}(kr) &\propto \frac{e^{jkr}}{r}, \qquad kr \gg n(n+1)/2 \\ h_n^{(2)}(kr) &\propto \frac{e^{jkr}}{r}, \qquad kr \gg n(n+1)/2 \end{aligned} \tag{4.59}$$

and

$$\begin{aligned} h_n^{(1)}(kr) &\propto \frac{1}{(kr)^{n+1}}, \qquad kr \ll 1 \\ h_n^{(2)}(kr) &\propto \frac{1}{(kr)^{n+1}}, \qquad kr \ll 1 \end{aligned} \tag{4.60}$$

As illustrated by these properties, the high order components decay rapidly; and as the wave reaches far enough, all the components at different orders behave like a simple 0-order spherical wave.

In the end, a general solution to Eq. 4.40 is given by

$$p(r, \theta, \phi, \omega) = \sum_{n=0}^{\infty} \sum_{m=-n}^{n} (c_{mn} h_n^{(1)}(kr) + d_{mn} h_n^{(2)}(kr)) \cdot Y_n^m(\theta, \phi) \tag{4.61}$$

where c_{nm} and d_{nm} are called spherical wave coefficients. In free field, the incoming wave term can be ignored, thus

$$p(r,\theta,\phi,\omega) = \sum_{n=0}^{\infty} \sum_{m=-n}^{n} c_{mn} \cdot h_n^{(1)}(kr) \cdot Y_n^m(\theta,\phi) \cdot e^{j\omega t} \tag{4.62}$$

4.2.3 Sound Energy

When a force $\boldsymbol{F}$ is exerted on a particle of matter and cause motion in space, energy is transferred to that particle by doing work: denote work as W,

$$W = \int_L \boldsymbol{F} \cdot ds \tag{4.63}$$

The rate of work is called power, given by:

$$P = \frac{dW}{dt} = \boldsymbol{F} \cdot \frac{ds}{dt} = \boldsymbol{F} \cdot \boldsymbol{u} \tag{4.64}$$

The power of sound pressure acting on the fluid particle is then given by:

$$P = \boldsymbol{F} \cdot \boldsymbol{u} = p\delta S \boldsymbol{u} \tag{4.65}$$

where p is sound pressure, $\boldsymbol{u}$ is particle velocity and δS is the area of the fluid element that is perpendicular to the particle velocity. The division of the power by the area defines a vector quantity that describes the power per unit area, called the sound intensity:

$$\boldsymbol{I} = p\boldsymbol{u} \tag{4.66}$$

Eq. 4.66 gives the expression for the instantaneous sound intensity. If both sound pressure and particle velocity are expressed as complex exponential forms, with magnitude $\hat{p}$ and $\hat{\boldsymbol{u}}$ respectively, then the time averaged intensity $\bar{\boldsymbol{I}}$ is given by:

$$\bar{\boldsymbol{I}} = \frac{1}{2}\mathrm{Re}\{\hat{p}\hat{\boldsymbol{u}}^*\} \tag{4.67}$$

The integral of the time-averaged sound intensity over a entire area enclosing a source gives the total radiated sound power, denoted by Π:

$$\Pi = \int_S \bar{\boldsymbol{I}} dS \tag{4.68}$$

From the general solution of sound pressure derived before, a simple and beautiful relation between the sound power Π and the spherical wave coefficients, c_{nm}, can be derived. First, substitute Eq. 4.62 into Eq. 4.36 to obtain the particle velocity:

$$u_r(r,\theta,\phi,\omega) = \frac{1}{j\rho\omega}\frac{\partial p}{\partial r} = \sum_{n=0}^{\infty}\sum_{m=-n}^{n}\frac{c_{nm}}{j\rho c}\cdot Y_n^m(\theta,\phi)\cdot h_n'(kr) \tag{4.69}$$

Then the sound power will be:

$$\Pi(\omega) = \frac{1}{2}\iint \mathrm{Re}\{pu_r^*\}r_0^2\sin\theta d\theta d\phi \tag{4.70}$$

Inserting Eq. 4.62 and Eq. 4.69 into Eq. 4.70, followed by the simplification through the orthogonality of the spherical harmonics, Eq. 4.70 becomes

$$\Pi = \frac{r_0^2}{2}\sum_{n=0}^{\infty}\sum_{m=-n}^{n}|c_{nm}|^2\mathrm{Re}\{\frac{h_n(kr_0)h_n'(kr_0)^*}{j\rho c}\} \tag{4.71}$$

This expression can be further simplified by using the Wronskian relationship (Williams 1999). It eventually reduces to:

$$\Pi = \frac{1}{2\rho c k^2}\sum_{n=0}^{\infty}\sum_{m=-n}^{n}|c_{nm}|^2 \tag{4.72}$$

4.2.4 $p-p$ Method for Sound Intensity Measurement

By definition, to calculate the sound intensity, both particle velocity and sound pressure are needed. In the cases where the linearized Euler's equation applies, the particle velocity can be estimated from the pressure gradient, thus the sound intensity can be measured by using two pressure transducers, which is the general principle of the $p-p$ method.

In Eq. 4.67, both the pressure and the particle velocity have to be the magnitudes of some sinusoidal functions. Meanwhile, the linearized Euler's equation requires differentiating $\boldsymbol{u}$ with respect to time. Therefore, the calculation of the sound intensity in the frequency domain is much simpler. Given the particle velocity, $\boldsymbol{u}(t)$, and sound pressure, $p(t)$, at an arbitrary position, with

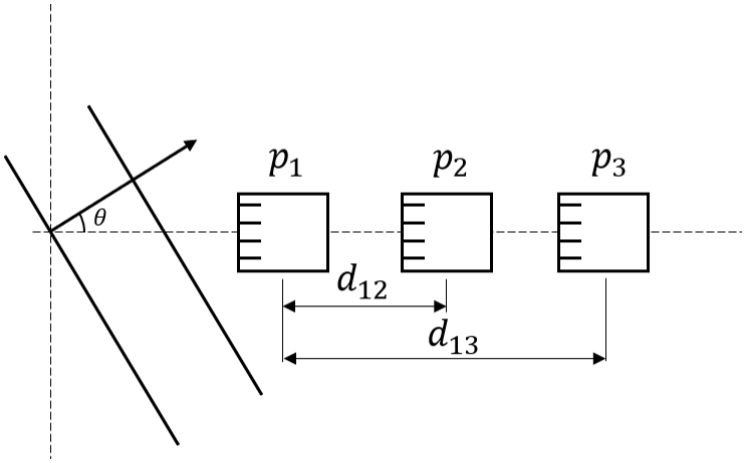

Fig. 4.5. $p-p$ Method Sound Intensity Measurement with 3-Microphone Probe

$$\boldsymbol{U}(\omega) = \mathcal{F}(\boldsymbol{u}),$$

and

$$P(\omega) = \mathcal{F}(p),$$

the spectral density of mean sound intensity will be

$$\bar{I}(\omega) = \frac{1}{2}\mathrm{Re}\Big\{ \lim_{T\to\infty} \frac{1}{T} P(\omega)\boldsymbol{U}^*(\omega)\Big\} \tag{4.73}$$

A division by T is necessary because $P(\omega)$ and $\boldsymbol{U}^*(\omega)$ are density functions i.e. p/Hz or $\boldsymbol{u}$/Hz, by definition. The term inside the real part operator is also called the cross-spectral density of p and $\boldsymbol{u}$, denoted by $G_{pu}(\omega)$. Fig. 4.5 shows the diagram of a sound intensity probe consisting of 3 microphones, which is exactly what are used on the robot. Each pair of 2 is enough for the sound intensity calculation. By taking microphones 1 and 2 for example, the sound intensity is calculated at the middle point of the two microphones, where

$$P(\omega) = \frac{1}{2}(P_1(\omega) + P_2(\omega)) \tag{4.74}$$

and

$$U_x(\omega) = \frac{1}{j\rho_0\omega}\frac{P_2(\omega) - P_1(\omega)}{d} \tag{4.75}$$

With this formulation, only the spatial gradient in the x-direction is estimated by the finite difference method. Thus, the $p-p$ method can only measure the intensity that is in the direction joining the microphone.

Inserting Eq. 4.74 and Eq. 4.75 into Eq. 4.73 yields,

$$\bar{I}(\omega) = -\frac{1}{\rho_0 \omega d} \mathrm{Im}\big\{G_{p_1 p_2}(\omega)\big\} \tag{4.76}$$

where $G_{p_1 p_2}(\omega)$ denotes the cross-spectral density of $p_1(t)$ and $p_2(t)$. In practice, the acquisition of infinitely long time sequences is impossible. Thus, $G_{p_1 p_2}(\omega)$ is then estimated by using the FFT, which is, however, affected by spectral leakage. To overcome this phenomenon, the Hanning window is applied to the time domains signals, and the computed DFT spectra are later scaled by a factor of $\sqrt{\frac{8}{3}}$ to account for the windowing.

It is necessary to point out that this $p-p$ method only works for a specific frequency band. To achieve confident accuracy, the distance d between two microphones needs to satisfy:

$$d < \frac{\lambda}{10} \tag{4.77}$$

The currently used 3-microphone probe has spacers with $d_{12} = 0.012$m, $d_{23} = 0.020$m, and $d_{13} = 0.032$m. The maximum frequency suggested by Eq. 4.77 is 2900 Hz, although the manufacturer gave a recommendation up to 5000 Hz. Microphone 1 and 2 are used for the frequency range of 500 Hz to 6000 Hz, and microphones one and three are taken for the frequency range of 40 Hz to 500 Hz (Klop 2010).

4.2.5 Spherical Harmonic Domain

Previous subsections introduced the spherical harmonic functions are solutions to the wave equation. It turns out that the pure mathematical solution can be connected to physics-based models directly.

Acoustical Multipoles

In acoustics, a complicated sound source can usually be modeled superposition of a series of simple sources, of which one of the most famous categories is the multipoles. These simple sources are induced by idealized physical models, and spherical harmonic functions are closely related to them.

The simplest multipole is called the monopole, which is generated by a dilating sphere. The sound field is determined by the volume change per unit time, or volume flow, Q_s and frequency f. Given Q_s and f in a fluid with known acoustic properties, the sound pressure is given by:

$$p(r,\theta,\phi) = -\frac{j\rho_0 ck}{4\pi} Q_s \frac{e^{jkr}}{r} \tag{4.78}$$

Note that this field is independent of angular variables and the radial part differs from the $h_0(kr)$ by a constant factor jk; thus, a monopole is identical to the order 0 spherical harmonic function Y_0^0. The relation between the spherical wave coefficient c_{00} and volume flow Q_s is given by:

$$c_{00} = \frac{\rho_0 ck^2}{\sqrt{4\pi}} Q_s \tag{4.79}$$

By putting two monopoles close to each other with the same magnitude but a 180 degree phase difference, a dipole can be created. For simplicity, only the sound pressure of a dipole along the z-axis is formulated: i.e.,

$$p(r,\theta,\phi) = -\rho ck^2 D_s \cos\theta (1 + \frac{j}{kr}) \frac{e^{jkr}}{4\pi r} \tag{4.80}$$

where $D_s = Q_s d$ called the dipole strength. Physically, a dipole is correlated to an oscillating force. The radial characteristic of this dipole is proportional to $h_1(kr)$ and the vertical dipole is identical to the Y_1^0. A dipole oriented along the x-axis is proportional to $\mathrm{Re}\{Y_1^{-1}\}$ and a dipole oriented along the y-axis is proportional to $\mathrm{Im}\{Y_1^1\}$. Consequently, an arbitrarily-oriented dipole can always be considered as the superposition of the three order 1 spherical harmonics.

The last multipole to be introduced in this thesis is quadrupoles. It can be considered as two oppositely-oriented dipoles. Physically, an oscillating moment can induce this type of sound source. Similar to a dipole, it is found that the quadrupoles has radial characteristics proportional to $h_2(kr)$, and angular directivity described by oder 2 spherical harmonics. However, not all quadrupoles can be represented by the linear combination of only order 2 spherical harmonics. It is found that the so-called longitudinal quadrupole is a Y_2^0 component subtracted a Y_0^0 component (Williams 1999). Nevertheless, projecting into the spherical harmonic domain provides valuable insight into the sound field.

Spherical Wave Spectrum

If the sound field on the surface of a sphere with radius r_0 is known, the spherical harmonic contents can be easily extracted by applying spherical Fourier transform Eq. 4.12: i.e.,

$$p_{nm}(r_0) = \iint p(r_0, \theta, \phi) Y_n^m(\theta, \phi)^* d\Omega \tag{4.81}$$

By comparing Eq. 4.62, the spherical wave expansion equation, with Eq. 4.9, the spherical Fourier series expansion, it's clear that the computed coefficients, p_{nm}, are the product of the spherical wave coefficients, c_{nm}, and the spherical Hankel function evaluated at kr_0, i.e.,

$$p_{nm} = c_{nm} h_n(kr_0) \tag{4.82}$$

The quantity p_{nm} is called the spherical wave spectrum (Williams 1999). Physically, this spectrum is related to the average of the sound pressure over the entire sphere distributed over different orthogonal components, described as

$$|\bar{p}_(r_0)|^2 = \frac{1}{S} \iint |p|^2 dS = \sum_{n=0}^{\infty} \sum_{m=-n}^{n} \frac{|p_{nm}(r_0)|^2}{4\pi} \tag{4.83}$$

where S denotes the area of the sphere. Here $\bar{p}_(r_0)$ is the surface averaged pressure; therefore $\frac{p_{nm}(r_0)}{\sqrt{4\pi}}$ can be considered to be the averaged pressure over the spherical harmonics Y_n^m.

The spherical Fourier transform can be applied to the radial particle velocity as well, which defines the particle velocity spectrum of the spherical wave,

$$u_{r,nm}(r_0) = \iint u_r(r_0, \theta, \phi) Y_(\theta, \phi)^* d\Omega \tag{4.84}$$

The relation among the velocity spectrum, pressure spectrum and the spherical wave coefficients are given by

$$u_{r,nm}(r_0) = \frac{c_{nm}}{j\rho c} h_n'(kr_0) = \frac{p_{nm}}{j\rho c} \frac{h_n'(kr_0)}{h_n(kr_0)} \tag{4.85}$$

Similarly, the velocity spectrum also represents the average of the squared velocity,

$$|\bar{u_r}(r_0)|^2 = \frac{1}{S} \iint |u_r|^2 dS = \sum_{n=0}^{\infty} \sum_{m=-n}^{n} \frac{|u_{r,nm}(r_0)|^2}{4\pi} \tag{4.86}$$

5. ACOUSTICAL HOLOGRAPHY

Although beamforming is a useful tool in many scenarios, acoustical holography was chosen to test the synthetic array, because it is able to give a comprehensive characterization of the sound field. In this chapter, some of the commonly used methods are reviewed and the one that suits the synthetic array and the objective of this thesis most is focused on. By analyzing the theory and conducting simulation test, it is anticipated to find problems upon the practical implementation, and propose some solutions if possible.

5.1 Review of Available Acoustical Holography Methods

Regardless of what method is used, acoustical holography includes two stages: decomposition and reconstruction. The first stage involves solving a boundary value problem. Given the governing equations of sound pressure and particle velocity, and a set of measured sound pressures and/or particle velocities on a boundary, the goal is to find a solution that satisfies the governing equations and boundary condition. The solution that satisfies the boundary condition is assumed to be the solution of the whole sound field. Thus, the acoustical quantities can be reconstructed anywhere in a 3-dimensional space. The locations of reconstruction depend on the interests and objectives of specific problems. Mostly, people desire a good reconstruction of pressure and particle velocity near the object surface, because it contains the information of source location and structural vibration. Obviously, the first stage is the harder part of this problem.

5.1.1 Fourier NAH

The Fourier method was the first version of acoustical holography to be developed. It is fair to say that this technology has fundamentally changed noise diagnostics (Wu 2008). Taking the Cartesian coordinate system, for example, the general solution for the sound pressure is:

$$p(x,y,z) = \frac{1}{4\pi^2}\int_{-\infty}^{+\infty}\int_{-\infty}^{+\infty} P(k_x,k_y)e^{j(k_x x+k_y y+k_z z)}dk_x dk_y \tag{5.1}$$

Suppose the pressure on an infinite plane is known, denoted by $p(\vec{\boldsymbol{r}}_h)$, then the pressure anywhere else in the 3-dimensional space can be described as:

$$p(\vec{\boldsymbol{r}}) = \mathcal{F}_x^{-1}\mathcal{F}_y^{-1}\Big(\mathcal{F}_x\mathcal{F}_y\big(p(\vec{\boldsymbol{r}}_h,\omega)\big)G_z(\vec{\boldsymbol{r}},\vec{\boldsymbol{r}}_h)\Big) \tag{5.2}$$

where

$$G_z(\vec{\boldsymbol{r}},\vec{\boldsymbol{r}}_h) = e^{jk_z(z-z_h)} \tag{5.3}$$

The process outlined by Eq. 5.2 involves a 2-dimensional Fourier transform and a 2-dimension inverse Fourier transform. The plane on which the measurements are taken is called the hologram. In practice, continuous spatial sampling over an infinite plane is impossible. Eq. 5.2 has to be reduced to discrete form, which is similar to the DFT or discrete-time Fourier series. For this formulation to be true, in each direction, equi-space sampling must be achieved to maintain the orthogonality. Meanwhile, due to the existence of the evanescent waves, this plane must be very close to the object, which is why the measurements have to be taken in the near-field.

The same idea can be applied to cylindrical coordinate and spherical coordinate system. In the spherical coordinate systems, if the pressure on the surface of a sphere is known (i.e., the hologram is a spherical surface), Eq. 4.12 and Eq. 4.62 can be applied. Preserving orthogonality on a discretely sampled spherical surface has previously also been discussed in Section 4.1.1. Because of the properties of spherical Hankel functions, the higher order a spherical harmonic decay rapidly in the radial direction. As a result, near-field measurements are also preferred.

5.1.2 IBEM

The inverse boundary element Method (IBEM) was developed to improve the performance of the reconstruction of sound fields radiated by irregularly-shaped sources. This method is derived from the Helmholtz integral equation, expressed as (Bai et al. 2013):

$$\alpha p(\vec{\boldsymbol{r}}) = \int_S \Big[p(\vec{\boldsymbol{r}}_0) \frac{\partial G}{\partial n}(\vec{\boldsymbol{r}}, \vec{\boldsymbol{r}}_0) - G(\vec{\boldsymbol{r}}, \vec{\boldsymbol{r}}_0) \frac{\partial p}{\partial n}(\vec{\boldsymbol{r}}_0) \Big] dS(\vec{\boldsymbol{r}}_0) \tag{5.4}$$

where S denotes the enclosed source surface; $\vec{\boldsymbol{r}}$ and $\vec{\boldsymbol{r}_0}$ denote the field point and the point on the source surface; $\frac{\partial}{\partial n}$ denotes the normal derivative on the surface; and $G(\vec{\boldsymbol{r}}, \vec{\boldsymbol{r}}_0)$ is the free-space Green's function associated with the Helmholtz equation,

$$G(\vec{\boldsymbol{r}}, \vec{\boldsymbol{r}}_0) = \frac{1}{4\pi |\vec{\boldsymbol{r}} - \vec{\boldsymbol{r}}_0|} e^{-jk|\vec{\boldsymbol{r}} - \vec{\boldsymbol{r}}_0|} \tag{5.5}$$

and

$$\alpha = \begin{cases} 1, & \vec{\boldsymbol{r}} \text{ is outside S} \\ 0.5, & \vec{\boldsymbol{r}} \text{ is on S} \\ 0, & \vec{\boldsymbol{r}} \text{ is inside S} \end{cases} \tag{5.6}$$

The integral in Eq. 5.4 can be numerically evaluated by using a mesh discretization on the boundary surface where the pressure and the normal velocity distribution on the boundary are interpolated by using surface shape functions. The pressure evaluated at an arbitrary location then becomes the linear combination of pressure and normal velocities on nodes of the boundary elements in the mesh. If Eq. 5.4 is evaluated on the source surface, then $\alpha = 0.5$, and

$$\frac{1}{2}\boldsymbol{p}_s = \boldsymbol{A}_s \boldsymbol{p}_s + \boldsymbol{B}_s \boldsymbol{u}_s \tag{5.7}$$

where $\boldsymbol{p}_s$ and $\boldsymbol{u}_s$ are the pressure and the normal velocity on the surface nodes (because of linearized Euler's equation, the term of normal derivative of pressure is proportional to the normal velocity), matrices $\boldsymbol{A}_h$ and $\boldsymbol{B}_h$ are the results of discretizing the two parts of the integral Eq. 5.4. If the the pressure is measured on a hologram

outside of the source, $\alpha = 1$ and the relation between the hologram pressure and the nodal pressure and normal velocity can be expressed as

$$\boldsymbol{p}_h = \boldsymbol{A}_h \boldsymbol{p}_s + \boldsymbol{B}_h \boldsymbol{u}_s \tag{5.8}$$

where $\boldsymbol{p}_h$ denotes the pressure measured on the hologram. The solution for $\boldsymbol{p}_s$ and $\boldsymbol{u}_s$ can be obtained by combining Eq. 5.7 and Eq. 5.7 will yield.

5.2 HELS

Both methods highlighted above have been used successfully. Unfortunately, neither of them is suitable for the synthetic array and the objectives of this thesis. Because of the hemi-spherical grid, the orthogonality apparently doesn't hold, and therefore the Fourier method is inapplicable. The IBEM is computationally expensive. It is risky to invest time and resources on the exploratory study before the concept of the synthetic array is proved feasible. Therefore, this thesis focused on is the method proposed by Wang and Wu called HELS (Wang & Wu 1997). It has a relatively simple formulation and competitive performance. In addition, this method uses the spherical harmonic functions as the component sources, which suits the robot grid very well.

Recall the Helmholtz equation,

$$\nabla^2 p + k^2 p = 0 \tag{5.9}$$

where p is the complex magnitude of sound pressure, and $k = \omega/c$ is the wave number. When p is subjected to Dirichlet, Neumann, or Robin boundary conditions, the solution can be expressed as a linear combination of orthogonal functions:

$$p = \sum_{i=1}^{N} C_i \psi_i \tag{5.10}$$

The function ψ_i is selected to satisfy any one of the following three conditions:

(1) Eigenfunctions satisfying the differential equation and the homogeneous boundary conditions

(2) Functions satisfying the differential equation, but not necessarily the boundary conditions

(3) Functions satisfying the boundary conditions, but not necessarily the differential equation

There are a great number of options for the selection of ψ_i. The easiest one is choosing the functions that satisfy condition (2) because the solution to the equation is well-known. As derived in Chapter 2, the general solution to Eq. 5.9 can be expressed as

$$p(r,\theta,\phi) = \sum_{n=0}^{\infty} \sum_{m=-n}^{n} c_{nm} h_n(kr) Y_n^m(\theta,\phi) \tag{5.11}$$

An obvious option for ψ_i will be

$$\psi_i(r,\theta,\phi) = h_n(kr) Y_n^m(\theta,\phi) \tag{5.12}$$

Given a set of sound pressure, $[p_1, p_2, \cdots, p_L]^{\mathrm{T}}$, measured at locations $[\vec{\boldsymbol{r}_1}, \vec{\boldsymbol{r}_2}, \cdots, \vec{\boldsymbol{r}_L}]^{\mathrm{T}}$

$$\begin{bmatrix} \psi_1(\vec{\boldsymbol{r}_1}) & \psi_1(\vec{\boldsymbol{r}_1}) & \cdots & \psi_{(N+1)^2}(\vec{\boldsymbol{r}_1}) \\ \psi_1(\vec{\boldsymbol{r}_2}) & \psi_2(\vec{\boldsymbol{r}_2}) & \cdots & \psi_{(N+1)^2}(\vec{\boldsymbol{r}_2}) \\ \vdots & \vdots & \ddots & \vdots \\ \psi_1(\vec{\boldsymbol{r}_L}) & \psi_3(\vec{\boldsymbol{r}_L}) & \cdots & \psi_{(N+1)^2}(\vec{\boldsymbol{r}_L}) \end{bmatrix} \begin{bmatrix} c_1 \\ c_2 \\ \vdots \\ c_{(N+1)^2} \end{bmatrix} = \begin{bmatrix} p_1 \\ p_2 \\ \vdots \\ p_L \end{bmatrix} \tag{5.13}$$

or

$$\boldsymbol{\Psi c} = \boldsymbol{p} \tag{5.14}$$

where N is the truncation order. Since there are $(2n+1)$ corresponding spherical harmonic functions at order n, the total number of unique term will be $(N+1)^2$ when truncated at order N. The subscript i on the coefficient c_i is called the spherical harmonic index in this thesis, which represents the order of the spherical harmonic in the sequence where the spherical harmonics are sorted from top to bottom and from left to right in Figure 4.1. For example, the vertical dipole has an index of 3.

In Eq. 5.14, $\boldsymbol{\Psi}$ can be evaluated, and $\boldsymbol{p}$ is the measured pressure. Thus it forms a system of linear equations where the c_i are the unknowns that need to be found. The general solution is given by:

$$\boldsymbol{c} = \boldsymbol{\Psi}^{\dagger} \boldsymbol{p} \tag{5.15}$$

where $(\cdot)^\dagger$ denote the pseudo-inverse operation. When the matrix $\boldsymbol{\Psi}$ is invertible, the pseudo-inverse is equivalent to the normal inverse and Eq. 5.15 gives the exact solution. In the cases that $\boldsymbol{\Psi}$ is not invertible, Eq. 5.15 gives the least squares estimate of $\boldsymbol{c}$.

5.3 Ill-Condition

A well-posed problem requires the existence, uniqueness, and stability of the solutions. Any problem that violates even one of these conditions is called an ill-posed problem. In the least squares fitting problem, the stability of the solution is more likely to be of concern. Instability implies any small variation in data or computation can lead to a change of orders of magnitude in the solution.

That effect is well illustrated by the following example. Given two matrices $\boldsymbol{A}_1$ and $\boldsymbol{A}_2$,

$$\boldsymbol{A}_1 = \begin{bmatrix} 1 & 1 \\ 0 & 0 \end{bmatrix}, \qquad \boldsymbol{A}_2 = \begin{bmatrix} 1 & 1 \\ 0 & 1 \times 10^{-10} \end{bmatrix}.$$

$\boldsymbol{A}_1$ is apparently singular and it's column space is a line. The matrix $\boldsymbol{A}_2$ differs from $\boldsymbol{A}_1$ by a very tiny value in the second row of the second column. That is, $\boldsymbol{A}_2$ is apparently non-singular and the column space of $\boldsymbol{A}_2$ is a plane. The equation

$$\boldsymbol{A}_1 \boldsymbol{x} = \begin{bmatrix} 2 \\ 1 \end{bmatrix}$$

has no exact solution because the vector $[2, 1]^{\mathrm{T}}$ is not in $\boldsymbol{A}_1$'s column space. The solution in least-squares sense is $\boldsymbol{x} = [1, 1]^{\mathrm{T}}$. However, the solution for this equation

$$\boldsymbol{A}_2 \boldsymbol{x} = \begin{bmatrix} 2 \\ 1 \end{bmatrix}$$

exists because the vector $[2, 1]^{\mathrm{T}}$ is in the column space of $\boldsymbol{A}_2$. The exact solution to this equation is $x = [2 - 10^{10}, 10^{10}]^{\mathrm{T}}$.

Although the solution of the second equation exists, the value is extremely large and the huge difference is caused by a tiny variation. This is because the matrix $\boldsymbol{A}_2$

is nearly-singular. Although the columns of $\boldsymbol{A}_2$ spans a plane, the angle between the two column vectors is extremely small. Consequently, if orthogonalizing $\boldsymbol{A}_2$, one of the basis vector will have an extremely small magnitude.

This intuitive example can be explained more rigorously by singular value decomposition (SVD). An arbitrary matrix $\boldsymbol{M}$ must have this decomposition

$$\boldsymbol{M} = \boldsymbol{U}\boldsymbol{\Sigma}\boldsymbol{V}^{\mathrm{H}} \tag{5.16}$$

where both $\boldsymbol{U}$ and $\boldsymbol{V}^{\mathrm{H}}$ are orthogonal, and $\boldsymbol{\Sigma}$ is diagonal. In more detail, the columns of $\boldsymbol{U}$ form an orthogonal basis of $\boldsymbol{M}$'s column space, and the rows of $\boldsymbol{V}^{\mathrm{H}}$ form an orthogonal basis of $\boldsymbol{M}$'s row space. The diagonal elements of $\boldsymbol{\Sigma}$, σ_i, usually sorted to $\sigma_1 > \sigma_2 > \cdots > \sigma_q$, are called the singular values of $\boldsymbol{M}$, which manifest the projected length of $\boldsymbol{M}$'s vectors onto these bases. Therefore, a singular value of zero indicates rank deficiency, and a small value indicates that one direction is insignificant. If there exists a strong correlation among the vectors of a matrix, this matrix must have small singular values. The condition of a matrix can also be described as the condition number,

$$\kappa = \frac{\sigma_{max}}{\sigma_{min}} \tag{5.17}$$

where σ_{max} is the greatest singular value and σ_{min} is the smallest non-zero singular value.

Given the theorem,

$$\boldsymbol{x} = \boldsymbol{M}^{\dagger}\boldsymbol{b} = \left(\boldsymbol{U}\boldsymbol{\Sigma}\boldsymbol{V}^{\mathrm{H}}\right)^{\dagger}\boldsymbol{b} = \boldsymbol{V}\boldsymbol{\Sigma}^{\dagger}\boldsymbol{U}^{\mathrm{H}}\boldsymbol{b} \tag{5.18}$$

how ill-conditioning will affect the inverse problem is better analyzed. Consider an over-determined system of linear equations, i.e., one in which the number of equations is greater than the number of unknowns

$$\boldsymbol{\Psi} = \boldsymbol{U}\boldsymbol{\Sigma}\boldsymbol{V}^{\mathrm{H}} = \boldsymbol{U} \begin{bmatrix} \sigma_1 & 0 & \cdots & 0 \\ 0 & \sigma_2 & \cdots & 0 \\ \vdots & \vdots & \ddots & \vdots \\ 0 & 0 & \cdots & \sigma_n \\ \vdots & \vdots & \vdots & \vdots \\ 0 & 0 & 0 & 0 \end{bmatrix} \boldsymbol{V}^{\mathrm{H}} \tag{5.19}$$

Substitution of Eq. 5.19 into Eq. 5.15 yields

$$\boldsymbol{c} = \boldsymbol{V} \begin{bmatrix} 1/\sigma_1 & 0 & 0 & 0 & \cdots & 0 \\ 0 & 1/\sigma_2 & 0 & 0 & \cdots & 0 \\ \vdots & \vdots & \ddots & 0 & \cdots & 0 \\ 0 & 0 & 0 & 1/\sigma_n & \cdots & 0 \end{bmatrix} \boldsymbol{U}^{\mathrm{H}}\boldsymbol{p} \tag{5.20}$$

According to Eq. 5.20, if there exists extremely small singular values, the estimated $\boldsymbol{c}$ will be very large. Given a fixed measurement numbers and locations, the content of the matrix $\boldsymbol{\Psi}$ completely depends on the order of truncation N. As the truncation order goes up, $\boldsymbol{\Psi}$ will eventually become ill-conditioned. One of the reasons for that is the correlation of the polynomials. The discrete $\cos(\theta)$ sampling is unable to reflect the complexity of polynomials of high degree. Another reason is the aliasing happening in the sinusoidal part of the spherical harmonic functions, which involves the discrete sampling of ϕ. And then, hemi-spherical sampling makes this problem even worse.

5.4 Regularization

To stabilize the results, a technique called regularization has to be introduced. The most straightforward approach to regularization is discarding the small singular values because they are the fundamental reason for instability, and small singular

values also imply that some dimensions of the space are negligible. This method is called truncated singular value decomposition (TSVD), and the solution given by this method is written as

$$\boldsymbol{c}_{reg} = \sum_{i=1}^{I_{reg}} \frac{\boldsymbol{u}_i^* \boldsymbol{p}}{\sigma_i} \boldsymbol{v}_i \tag{5.21}$$

where I_{reg} is the truncation order, and $\boldsymbol{u_i}$ and $\boldsymbol{v_i}$ are the column vectors of $\boldsymbol{U}$ and $\boldsymbol{V}$, respectively.

Another commonly used method is called the Tikhonov method. Since the instability results in the huge magnitude of the solution, the idea of this method is to find such a $\boldsymbol{c}$ that minimizes

$$\|\boldsymbol{\Psi c} - \boldsymbol{p}\| + \lambda \|\boldsymbol{c}\|$$

instead of the norm of the error, where λ is a constant called the regularization parameter. Essentially, the Tikhonov method stabilizes the results by changing Eq. 5.20 to

$$\boldsymbol{c} = \boldsymbol{V} \begin{bmatrix} \frac{\sigma_1}{\sigma_1^2+\lambda} & 0 & 0 & 0 & \cdots & 0 \\ 0 & \frac{\sigma_2}{\sigma_2^2+\lambda} & 0 & 0 & \cdots & 0 \\ \vdots & \vdots & \ddots & 0 & \cdots & 0 \\ 0 & 0 & 0 & \frac{\sigma_n}{\sigma_n^2+\lambda} & \cdots & 0 \end{bmatrix} \boldsymbol{U}^{\mathrm{H}} \boldsymbol{p}. \tag{5.22}$$

When using both methods, it is necessary to determine their own parameters, I_{reg} and λ respectively. Commonly used techniques for parameter selection include (1) the L-curve method; and (2) Generalized Cross Validation (GCV). In the L-curve method, the norms of the solutions and the norms of the residuals are calculated at different truncation order. When plotting these two norms against each other on the log-log scale, the curve usually has an L-shape. On the curve, the corner is considered to be the optimal choice of the parameter. For the GCV method, one of the measured data points is first removed, and the remaining data is used to make a prediction at that point, with an assumed λ. This process is repeated for every single location and the optimal choice parameter is the one that minimizes the sum of errors at all the measurement locations.

5.5 Simulation Study

To verify the theory of HELS and also understand the limitations of this method, a few idealized cases were simulated in MATLAB. In each case, a number of point sources (monopoles) are placed at different positions. In the scope of linear acoustics, the sound pressure at any arbitrary point is the superposition of the pressure generated by each source. An imaginary microphone array "measures" the sound pressures and the spherical wave coefficients are then estimated by using HELS. Once the coefficients are determined, the substitution of these coefficients into Eq. 4.62, with evaluated $Y_n^m(\theta, \phi)$ and $h_n(kr)$ at locations of interest, would give the sound pressure reconstruction. In the cases where the sound intensity is concerned, the coefficients c_{nm} would be substituted into Eq. 4.69 to obtain the particle velocity, or the pressure gradient could be computed numerically.

5.5.1 Case 1 - Monopole

The first case compares the sound field of an analytic monopole with the HELS computed results. As introduced in Chapter 4, a monopole can be generated by a dilating sphere. Given the volume flow, Q_s and frequency f, the sound pressure is described by Eq. 4.78. A monopole is identical to an order 0 spherical harmonic function. Given the characteristic parameters of the monopole, the spherical wave coefficient c_{00} can be computed by Eq. 4.79.

The sound intensity in the θ and ϕ direction of a monopole are zero because the pressure gradients in those directions are zero. The radial sound intensity is given by:

$$I_r(r, \theta, \phi) = \frac{|Q_s|^2}{2} \frac{\rho_0 c k^2}{(4\pi r)^2} \tag{5.23}$$

Since the sound intensity is a constant at the same radius, the sound power is calculated simply by multiplying the latter by the surface area: i.e.,

$$\Pi = \frac{\rho_0 c k^2}{8\pi} |Q_s|^2 \tag{5.24}$$

Table 5.1.
Case 1 Results

	Analytic	HELS
c_{00}	3.8939 E1	3.8939 E1 + 2.1950 E-12j
I_r	4.4742 E0	4.4742 E0
Π	5.4923 E-3	2.7461 E-3

In the simulation, a 1000 Hz monopole is placed at the origin with volume flow of 1×10^{-3} m^3/s, with $\rho_0 = 1.20\mathrm{kg}/\mathrm{m}^3$ and $c = 343.2$ m/s. The virtual microphone array is the 225-point robot grid with 0.96-meter radius and its center at the origin. Knowing there is only a monopole source, the spherical wave truncation order is set to be $N = 6$. The matrix $\mathbf{\Psi}$ is then a 225-by-49 matrix that is well-conditioned. Table 5.1 summarizes the simulation results. HELS accurately determined the spherical harmonic coefficient and sound intensity. The sound power of HELS is exactly half of the analytic sound power because the robot grid only measures a hemisphere, which only includes 50% sound energy.

5.5.2 Case 2 - Dipole

In the second case, two 1000 Hz monopoles are placed at $(0, 0, -0.01)$ and $(0, 0, 0.01)$ with a 180 degree phase difference, which should theoretically create a vertical dipole. The sound pressure generated by this dipole is the superposition of two monopoles and the analytic sound intensity of a dipole is given by:

$$I_r(r, \theta, \phi) = \frac{\rho_0 c k^4 |D_s|^2 \cos^2\theta}{2(4\pi r)^2} \tag{5.25}$$

where $D_s = Q_s d$ called the dipole strength, and d is the distance between the two monopoles. Integration of Eq. 5.25 gives the sound power of a dipole:

$$\Pi = \frac{\rho_0 c k^4 |D_s|^2}{24\pi} \tag{5.26}$$

The vertical dipole is identical to spherical harmonic Y_1^0. Thus only one significant value is expected to appear in the estimated coefficients. Insertion of Eq. 5.26 to Eq. 4.72 allows the possibility to derive relation between spherical wave coefficients and the dipole strength:

$$\sum_{i=-1}^{1} |c_{1,i}|^2 = |c_{10}|^2 = \frac{\rho^2 c^2 k^6}{12\pi} |D_s|^2 \tag{5.27}$$

In the same way as for case 1, the 225-point robot grid is used and the spherical wave is truncated at order $N = 6$, at which point ill-conditioning still does not occur.

Figure 5.1 highlights the sound pressure simulation results. Only one peak appears at index 3, which is exactly the term of Y_1^0. The estimated coefficient is literally the same as the one given by the analytic equation, as shown in Figure 5.2. To visually compare the original sound field with the reconstruction, the sound pressure on the $y-z$ plane is plotted. The reconstructed sound field matches the original sound field, seemingly perfect, and the bottom right graph says there is nearly 0 error on the whole plane.

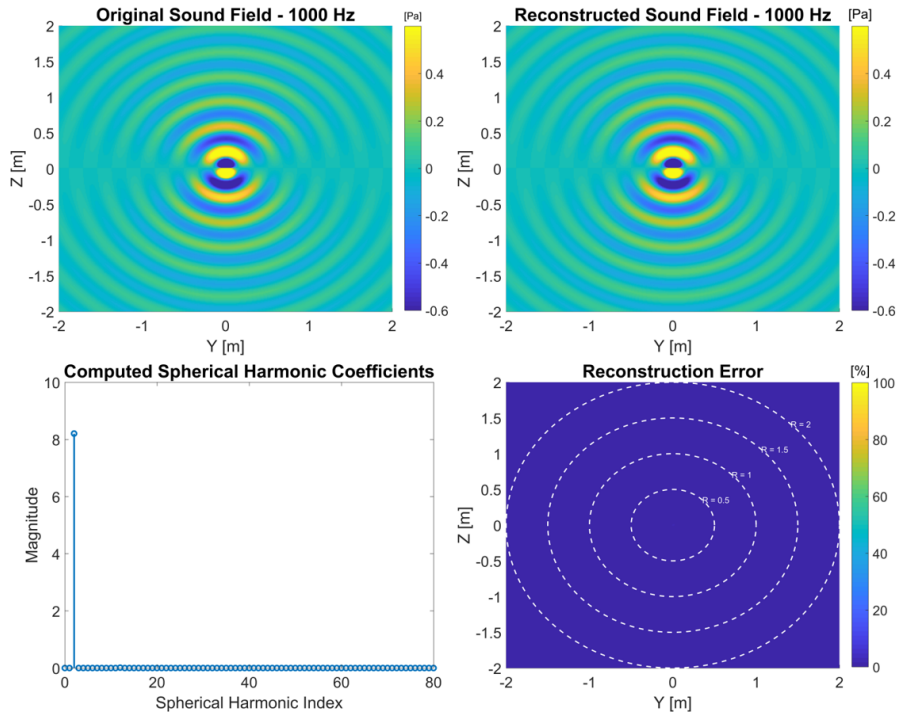

Fig. 5.1. Sound Pressure Simulation of Dipole

Figure 5.2 compares the sound intensity and sound power given by Eq. 5.25 with HELS reconstruction. Eq. 5.25 describes the radial sound intensity as a function of elevation angle θ. The HELS reconstructed sound intensity shows great consistency with this analytic sound intensity. Again, the HELS sound power is approximately 50% of the analytic sound power because the grid only covers half of a sphere. To demonstrate the capability of acoustical holography, a vector intensity map is reconstructed on the plane at $x = 0.5$ m, as presented on Figure 5.3. The color and arrow

length represents the magnitude of the intensity, and the arrow direction points to the intensity direction. The orange lines are the velocity streamlines. Definitely, all the information needed for the 3-dimensional energy flux is available: it is just more complicated in the visualization side.

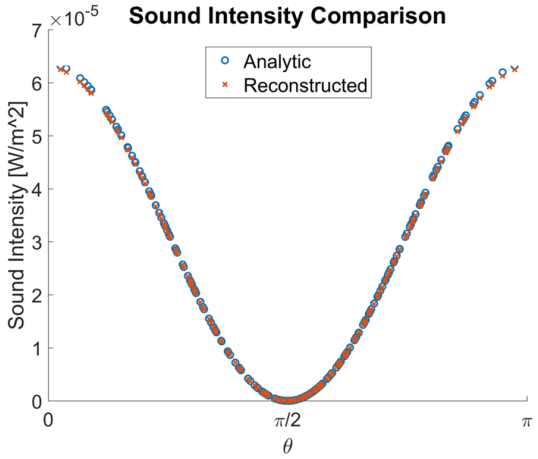

	Analytic	HELS
$\lvert c_{1,0}\rvert$	8.2317 E1	8.2042 E1
Π	2.4545 E-04	1.2120 E-04

Fig. 5.2. Sound Intensity and Sound Power Comparison

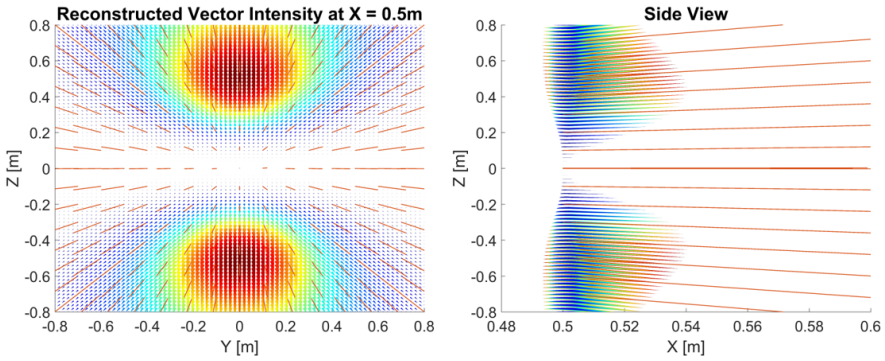

Fig. 5.3. Vector Intensity of a Dipole at $x = 0.5$ m

5.5.3 Case 3 - Complicated Source

The good results in the previous two cases were not too surprising because the sound fields were simple and clean. The following case studies a complicated sound

field, which is generated by putting 3 monopoles at random positions with random magnitudes and phases. The positions and magnitudes of the dipoles are summarized in Table 5.2. Since there is not an analytic description for this field, the criteria for good results is totally based on (1) the goodness of fit on the measured data, and (2) the quality of the reconstruction. Unlike the previous two cases, was 225-point grid is not used in this case; instead, a 2701-element virtual array was placed in the simulated sound field, shown as Figure 5.4. The number of elements is unrealistically big because the goal is to find the limiting factor of the method that is independent of the finite sampling. All these elements are on a sphere with a 1-meter radius. The angular resolution in both the θ and ϕ directions was 5 degrees.

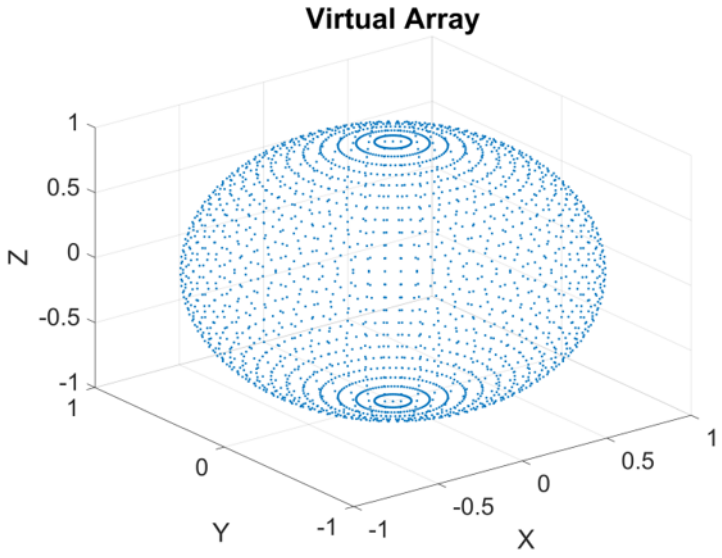

Fig. 5.4. 2701-Element Virtual Array

Truncation, in this case, happens at $N = 19$, which results in a 2701-by-400 matrix $\mathbf{\Psi}$ with good conditioning. Figure 5.5 outlines the results. Clearly, more spherical harmonics appeared. The $x - y$ plane is sliced to observe the sound pressure. What is impressive is that the reconstruction error in the center region is extremely big, but beyond that region the is nearly zero. From the estimated spherical harmonic coefficient plot, it's clear that the components above order 9 are all basically 0. By

Table 5.2.
Locations and Magnitudes of Monopoles

Index	x[m]	y[m]	z[m]	Magnitude
1	0.0163	-0.2136	-0.0529	0.6262 + 0.4927j
2	-0.1333	0.0914	-0.0448	-0.8249 + 0.4498j
3	-0.0795	0.2084	-0.0558	-0.3503 + 0.7486j

examining the pressure in the center, it is found that the pressure is unreasonably high. It is safe to say the failure in the center is not because of the insufficient order. In a word, under an idealized condition, with sufficient order and an excessive number of microphones, it is still not possible to achieve perfect reconstruction on the whole field, especially in the region that is close to the origin.

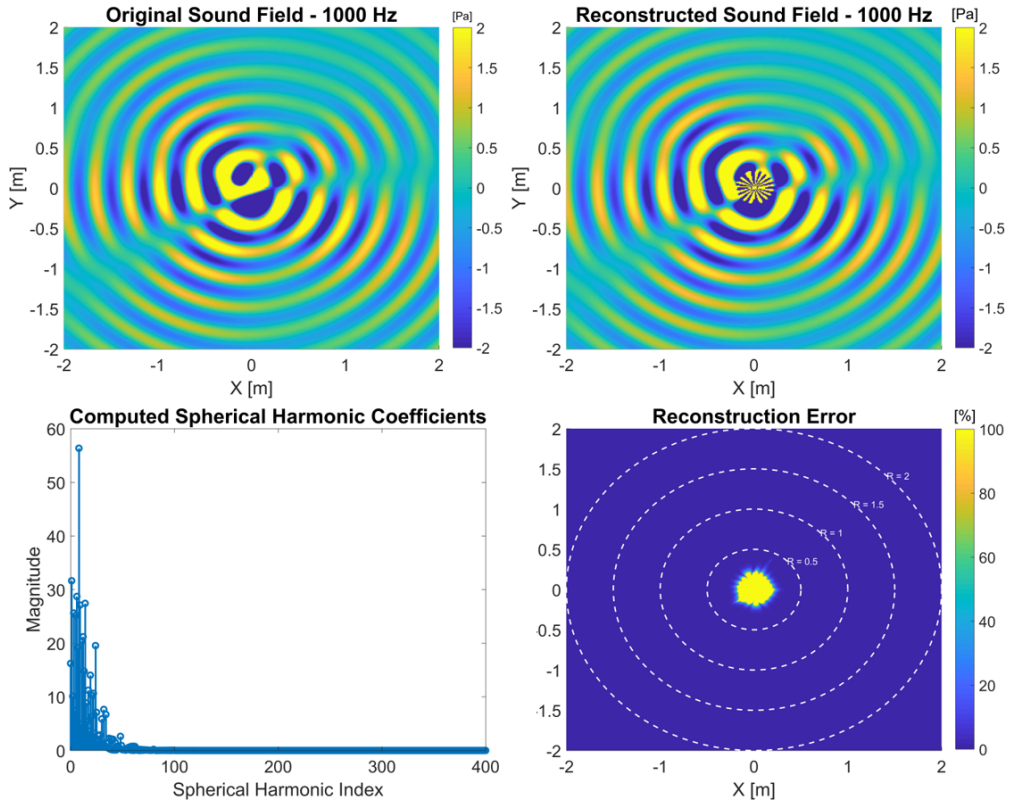

Fig. 5.5. Sound Pressure Simulation of a Complicated Field

This phenomenon should be attributed to the properties of the spherical Hankel functions. As mentioned in Chapter 4, when kr approaches 0, the value of spherical Hankel function goes up quickly with the rate of $(kr)^{n+1}$. If trying to use the measurements taken at $r = r_1$ to reconstruct sound pressure at $r = r_2$, given $h_n(kr_2) = 10^x \cdot h_n(kr_1)$, the estimation of the coefficients at order n must be accurate to the x^{th} decimal place; otherwise, the reconstruction error will go beyond 100%. As demonstrated by Figure 5.6, when the measurements are taken at $r_0 = 1$ m and the order of 10 is required, for example, it will require the estimation to be accurate to at least the 7^{th} decimal place to achieve good reconstruction at $r = 0.1$ m. The latter requirement becomes very challenging from the perspective of either numerical computation or data collection. The only good news is, the size of an axial piston machine is usually greater than a 0.1-meter-radius sphere. The pump used for the later case study has the dimensions of 243mm × 150mm × 235mm.

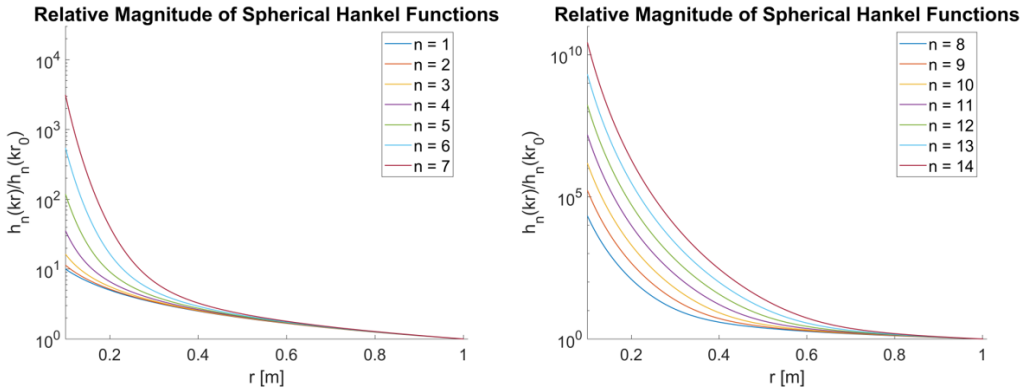

Fig. 5.6. Relative Magnitude of Spherical Hankel Functions, $r_0 = 1$

In the same sound field, it would be interesting to see what happens if the 225-point grid is used as the microphone array. Due to the complexity of the sound field, the truncation order was set as high as possible. A value of $N = 14$ is finally decided because in that case, the number of unknowns equals the number of equations. However, this 225-by-225 matrix turned out to be ill-conditioned, with a condition number of 2.30×10^{12}. Consequently, if simply applying least squares estimation,

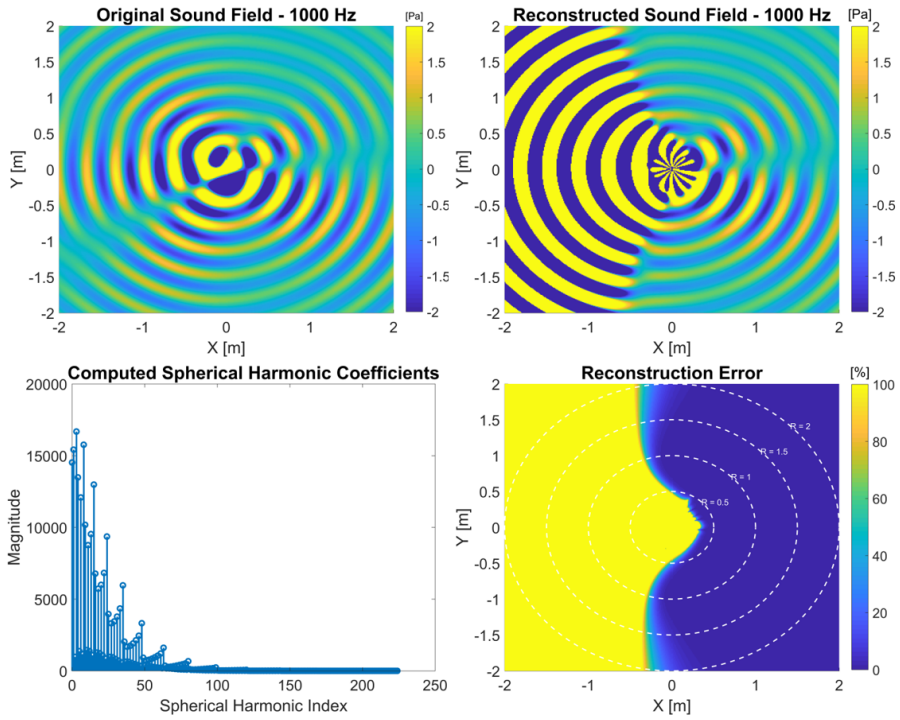

Fig. 5.7. Sound Pressure Simulation of a Complicated Field Using 225-pt Grid

shown as Figure 5.7, many of the estimated coefficients have magnitudes above 10000, while the maximum value from the 2701-element array was below 60. Although the reconstruction results on one side of the space ($x > 0$), on which the microphone array is placed, were surprisingly good, the pressure on the other side ($x > 0$) had values up to 1500 pascal (not visible because of the color scale saturation), which is definitely beyond the range of acoustical pressures.

The problem of ill-conditioning had been foreseen, and the solution for it is regularization. When using the same data collected, Figure 5.8 presents the results given by the Tikhonov method. Introducing regularization will definitely hurt the goodness of fit because the criterion is no longer to minimize the total residuals. Surprisingly, under the Tikhonov regularization, the R^2 is still 0.9998, which is defined as

$$R^2 = 1 - \frac{\boldsymbol{e}^{\mathrm{H}} \cdot \boldsymbol{e}}{\boldsymbol{p}^{\mathrm{H}} \cdot \boldsymbol{p}} \tag{5.28}$$

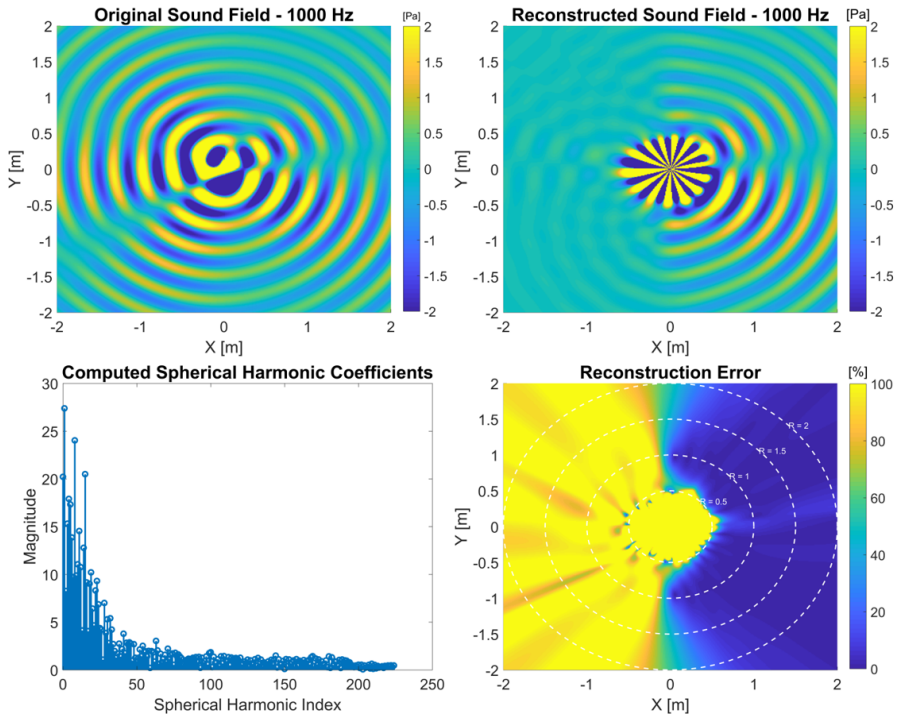

Fig. 5.8. Sound Pressure Simulation of a Complicated Field Using Tikhonov Method

where $\boldsymbol{e} = \boldsymbol{\Psi c} - \boldsymbol{p}$. This value is definitely acceptable, because it statistically means 99.98% of the measured data can be described by the regression model. After regularization, the estimated coefficients are now in the normal range, but they still differ significantly from the 2701-element estimation and the high order contents become much noisier. The reconstruction on the measurement side of the space is still decent, and the acoustical quantities on the other side are now in a reasonable range, although they are still not even close to the true values.

5.5.4 Case 4 - Symmetric Sound Field

The consistent failures on the left side of space in the previous study imply an important piece of information: sampling only on one side of the space will not necessarily give satisfying results on both sides. This is because the solution satisfying

the given boundary condition is not unique. Unfortunately, the possessed synthetic array is hemi-spherical; although the only the results on one half of the space (chamber room) are interested, the other half still places constraints on our solutions. Without taking this into consideration, the estimation will not be physically correct. This hidden constraint is symmetry.

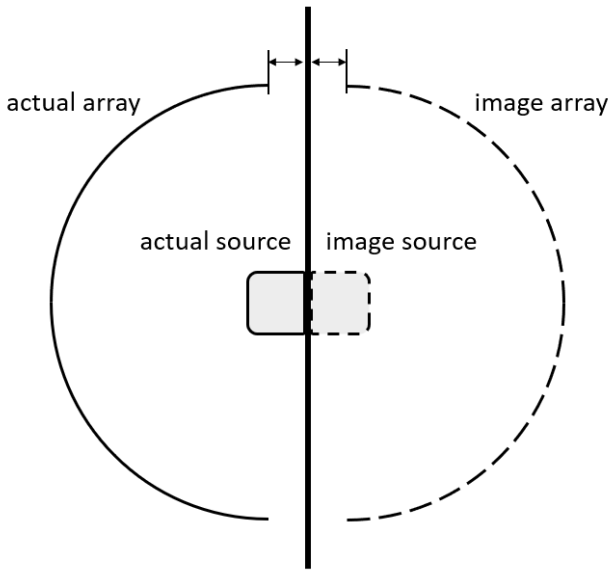

Fig. 5.9. Image Source and Image Array

As introduced in Chapter 3, the wall in the hemi-anechoic chamber functions as a reflective plane. In acoustics, when a reflective surface is hard, the boundary condition on this surface is zero normal particle velocity, i.e. $u_n = 0$. A common approach to simplifying this problem is to use the image source method. If we assume there is no reflective surface, and instead put an identical source at the mirror image position of the actual source, the sound field on the reflected side is equivalent to the case where there is a reflective surface, and the boundary condition of $u_n = 0$ is also satisfied. Meanwhile, the sound field is now symmetric with respect to the reflective plane. Thanks to that symmetry, we can easily give a solution that satisfies all the boundary conditions and the hidden constraint by putting an image array on the side

of the image source. The data gathered on each element of the image array is exactly the same as its corresponding actual microphone measurement, shown as Figure 5.9.

To accomplish this process, there is another fact that needs to be accounted for. In previous simulation studies, the origin of the coordinate system was set at the center of the 225-point hemi-spherical grid; however, the center of the hemi-spherical grid is not on the plane of the wall. If we mirror the array with respect to the wall, the origin has to be on the wall and the final symmetric array won't be on any spherical surface, although it doesn't bring any difficulties to the HELS method.

Table 5.3.
Locations and Magnitudes of Monopoles

Index	x[m]	y[m]	z[m]	Magnitude
1	-0.1487	0.1185	0.1389	0.3573 + 0.2804j
2	-0.1912	-0.0828	0.1853	-0.4122 - 0.6267j
3	0.0532	-0.1657	-0.1703	0.4018 - 0.5843j
4	0.1487	0.1185	0.1389	0.3573 + 0.2804j
5	0.1912	-0.0828	0.1853	-0.4122 - 0.6267j
6	-0.0532	-0.1657	-0.1703	0.4018 - 0.5843j

In the simulation, the symmetric sound field was created by putting 6 monopoles symmetrically with respect to $y - z$ plane. We firstly execute HELS on a hemi-spherical array on which $x > 0$ and compare the results with the symmetric array created by mirroring. Again, a dense array is made with 5-degree angular resolution on both θ and ϕ direction to avoid ill-conditioning. Figure 5.10 summarizes the results of the one-sided hemi-spherical array. Familiar results are observed: reconstruction on the positive x side is decent but failure occurs on the side of negative x.

At the same time, by using the mirrored 225-point robot grid (with 450 elements in total), reconstruction on both sides matches the true sound field very well (if ignoring the center region), which means this proposed method successfully solves the problem.

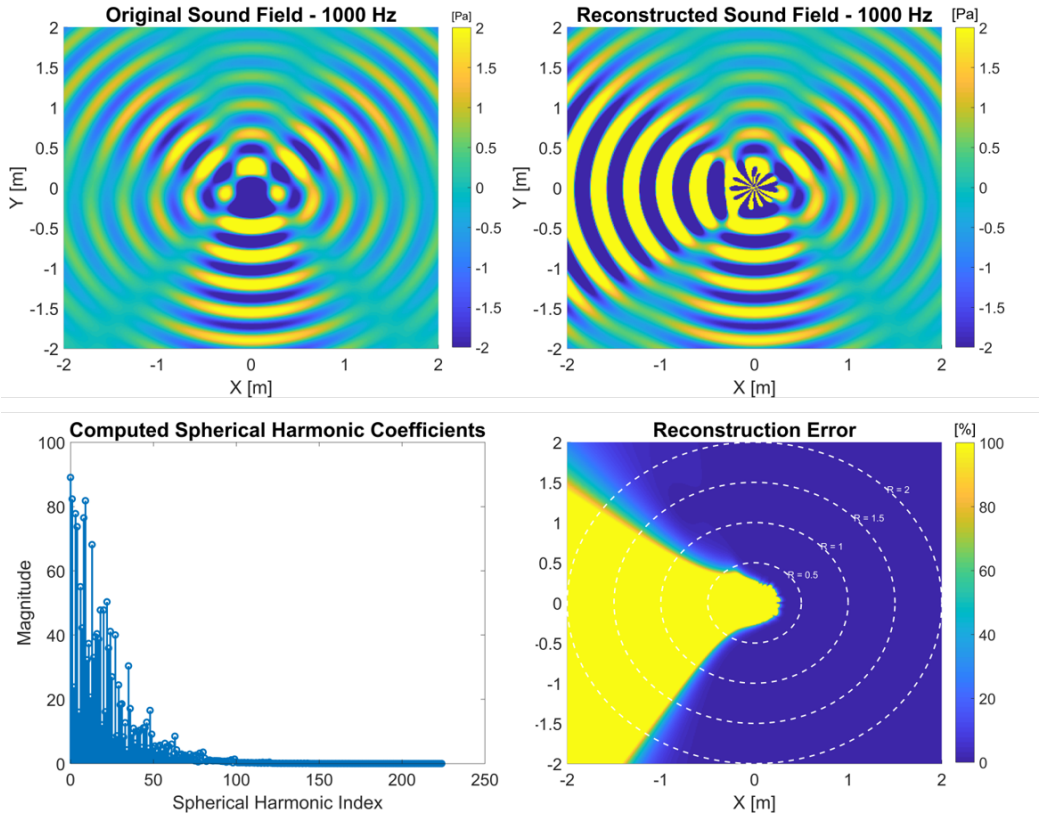

Fig. 5.10. Simulation for One-sided Sampling Only

If we observe the coefficients computed by two different virtual arrays, we found they are distinct. This proves that the solution satisfying the condition on the space of $x > 0$ is not unique. Meanwhile, the mirroring of the grid brings another surprise: it improves the conditioning of matrix $\mathbf{\Psi}$, which is still truncated at $N = 14$ but now has a size of 450-by-225. Thus, regularization is not even needed in this case.

5.5.5 Summary

All these simulation studies numerically proved the applicability of HELS and provided meaningful insight into this method. If there are mulipoles placed at the origin, this method could give an accurate parameter estimation and nearly perfect reconstruction on the whole field. If the sound field is complicated, some high order

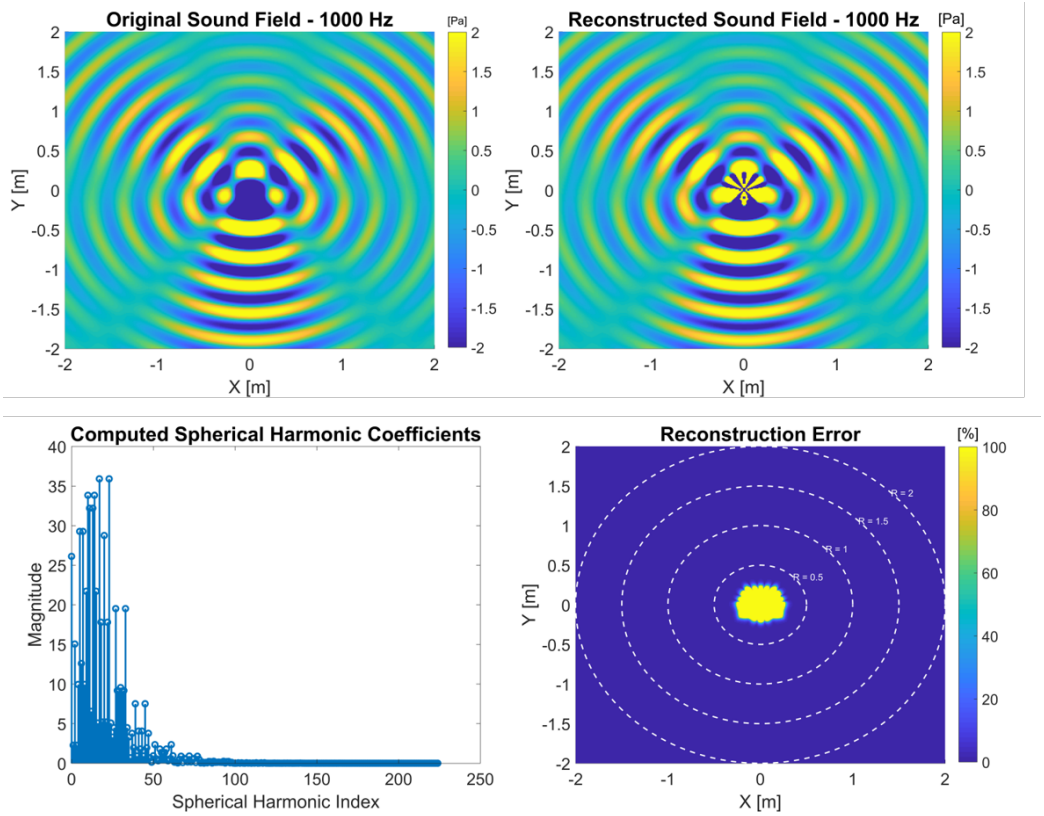

Fig. 5.11. Simulation with Image Array

functions will have to be included in the solution. Once the high order components are introduced, inward reconstruction will be limited to a small range because of accurately estimating the magnitudes of coefficients is difficult and the error will be exaggerated by the spherical Hankel functions as the reconstruction point approaches the center.

Another important finding was, sampling only on one side of origin is likely to cause failure of reconstruction on the other side, because of the non-uniqueness of the solution. In the cases where sampling only happens on one side, the constraints on the other side must be taken into consideration. In Maha's chamber, due to the existence of the reflective wall, the sound field must be symmetric with respect to the plane of the wall. Consequently, an image array is placed on the image field to

guarantee that the solution satisfies the requirement of symmetry. As a side effect, the ill-condition of the matrix $\mathbf{\Psi}$ is surprisingly eliminated.

6. CASE STUDY

In this chapter, acoustical holography is implemented on the synthetic array for real pump measurements. Two cases are used for the study, of which both were for the same 44cc open circuit pump, but operated under different conditions. Table. 6.1 highlights the operating conditions of these two cases. It needs to be pointed out that both cases are running on the same 225-point robot grid. There is a missing point in the first case because one of the measurements were taken while the DAQ was being initialized. Thus on that point the sensors were not measuring; therefore it is discarded. These two cases were operated under 1200 rpm and 2400 rpm respectively, which leads to the 1^{st} shaft frequencies of 20 Hz and 40 Hz. Combined with the fact that this machine has 9 pistons, the 1^{st} harmonic frequency in both cases are 180 Hz and 360 Hz respectively.

Table 6.1.
Operating Conditions of Case Study

Opcon.	Speed [rpm]	Pressure [bar]	β [%]	Grid #
1	1200	200	100	224
2	2400	200	75	225

6.1 Characteristics Overview

Figure 6.1 illustrates the SPL spectrum of the two cases. In both cases, the strongest components are at the pump harmonics and all the local maxima (peaks) occur at the shaft orders. When it is recognized that the TSA functions as a comb filter, only picking up the shaft orders, we can safely use deterministic components of

the measured signals to represent the array signals without worrying about missing important information. The spectrum of case 1 is dominated by its 1^{st} harmonic, which is more than 10 dB greater than the second strongest peak. In case 2, there is not a significantly dominant component, and the signal power is evenly distributed over the pump harmonics, and the high-frequency components begin to make more of a contribution.

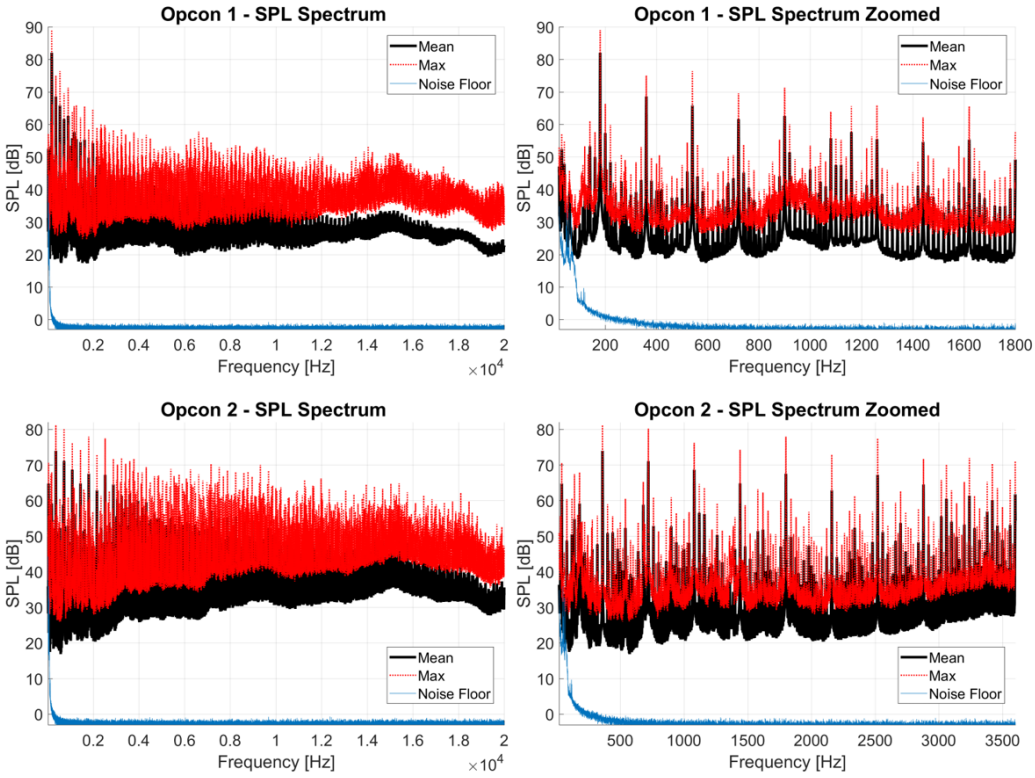

Fig. 6.1. SPL Spectrums

Figure 6.2 highlights the distribution of A-weighted sound pressure level (SPL) on the sphere for both cases. The surface averaged SPL for both cases are 77.37 dBA and 83.63 dBA, respectively. It can be seen that, over the surface of the sphere, 15dB and 6 dB variations are observed in both cases, respectively. Figure 6.3 illustrates the distribution of the sound intensity for both cases. The sound power in the region of 40 Hz to 5000 Hz for both cases are 87.86 dB and 87.35 dB, respectively. The two

values of sound power are close because: (1) the A-weighting applied on the SPL but not on SIL, and (2) the high-frequency energy, which is relatively high according to the spectrum, is not included.

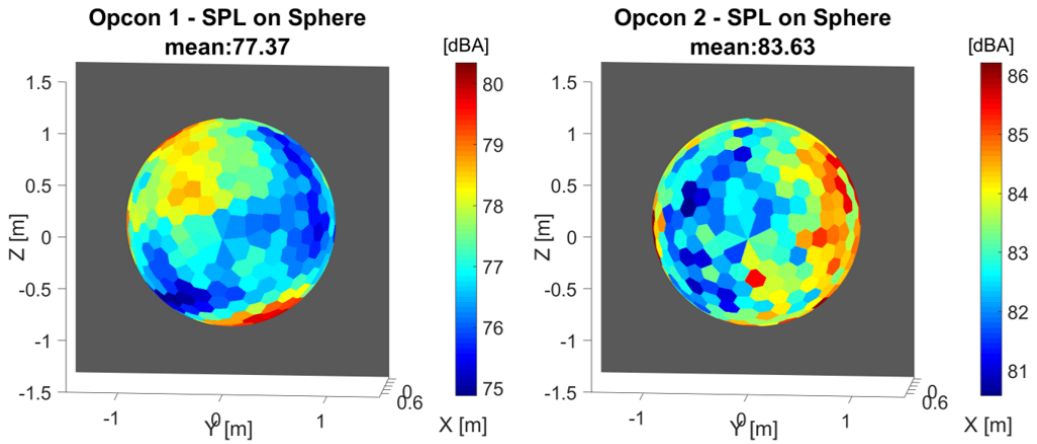

Fig. 6.2. SPL on Sphere

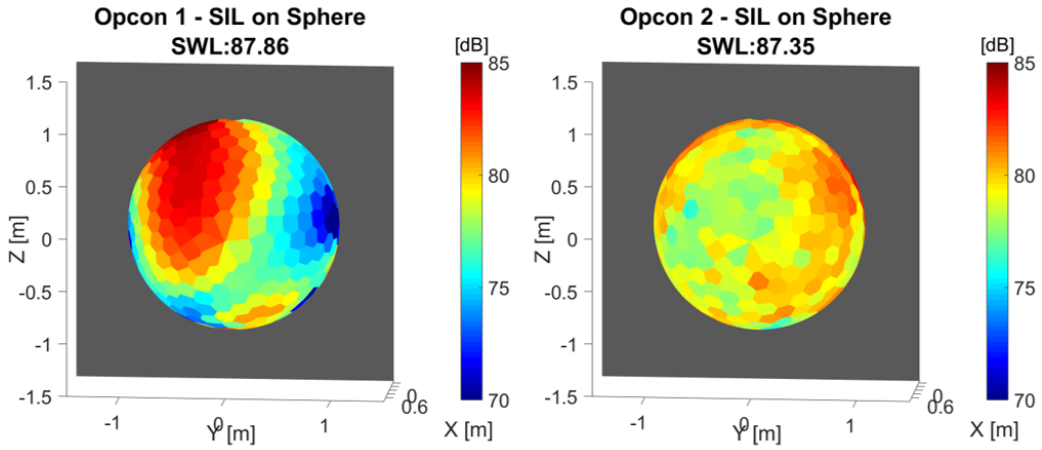

Fig. 6.3. SIL on Sphere

6.2 HELS Implementation

Of all the frequency components, the 1^{st} harmonic of case 1 has the strongest signal power. Thus, this frequency is taken as an example to illustrate the HELS fitting. Noticing that the formula of HELS requires a knowledge of the single frequency complex pressure, the DFT needs to be applied. Recalling the DFT case study demonstrated in section 4.1.3, if the DFT number, denoted by N_{dft}, is not chosen properly, the discrete frequency domain sample will not occur at the frequencies of interest. The frequency resolution, f_0, (converting ω_0 to Hz) is determined by N_{dft}: i.e.,

$$f_0 = \frac{f_s}{N_{\text{dft}}} \tag{6.1}$$

where f_s is the sample rate. The frequency of interest, f_i, must be an integer multiple of f_0, i.e.

$$f_i = k\frac{f_s}{N_{\text{dft}}}, \qquad k \in \mathbb{Z} \tag{6.2}$$

Thus, N_{dft} is an integer than satisfies the form of:

$$N_{\text{dft}} = k\frac{f_s}{f_i}, \qquad k \in \mathbb{Z} \tag{6.3}$$

As long as f_i is a rational number (it must be true for any shaft order), there must exist such a $k \in \mathbb{Z}$ that makes the right side of Eq. 6.3 an integer. After the FFT is applied to every deterministic component, the vector $\boldsymbol{p}$ is produced by picking the complex pressure at the desired frequency from every DFT spectrum. Meanwhile, because the DFT of a real-valued signal has both positive and negative frequency contents, to correctly represent the strength at the chosen frequency, a factor 2 needs to be applied.

Figure 6.4 illustrates the magnitudes of measured sound pressure and the fitted sound pressure at 180 Hz. The graphs can be interpreted as the directivity pattern of the sound. Plotting on a sphere, they are created by replacing the constant radius by the pressure magnitudes on each point. In Figure 6.4, the shape on the left and right are nearly identical. Statistically, the R^2 value is 0.9999. It is safe to conclude that very good fitting is achieved on the hologram.

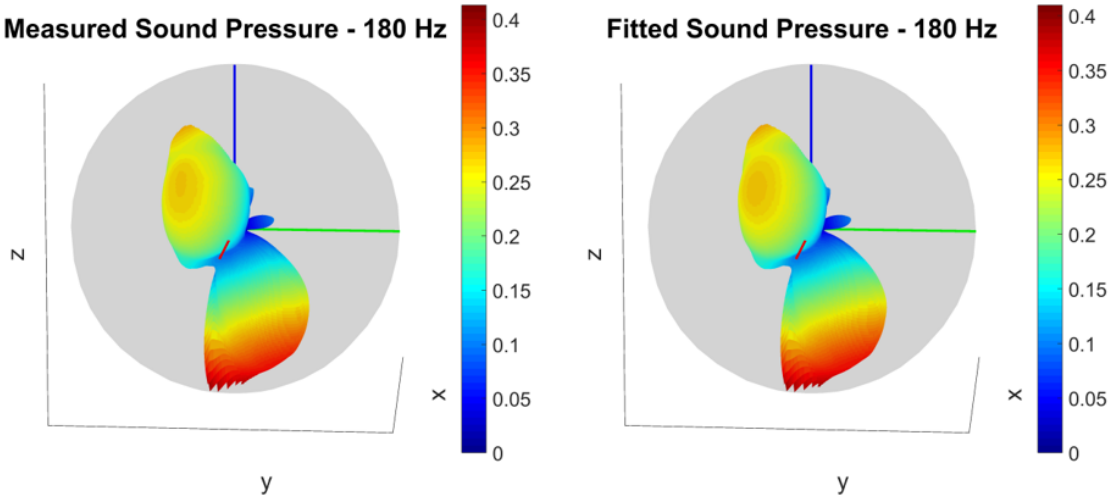

Fig. 6.4. Measured vs Fitted at 1^{st} Harmonic of Opcon. 1

Figure 6.5 shows the computed c_{nm}. As expected, since the matrix $\mathbf{\Psi}$ is well-conditioned, all the computed coefficients are in a reasonable range. For the indices greater than approximately 50 ($N > 6$), the magnitudes of the coefficients are relatively small. When zooming in, it can be seen that the top 3 strongest components are at indices 2, 3 and 4, which together form an inclined vertical dipole. This result also agrees with the intuitive interpretation of the directivity pattern shown on Figure 6.4.

6.2.1 Validation

A good estimation of c_{nm} should not only produce precise fitting on the measurement data set but also enable a good reconstruction at other locations. To examine the ability of the reconstruction, two validation tests were conducted without making additional measurements. The first test was called cross-validation. The fitting model was firstly generated from a subset of the measured data. Then the complex pressure

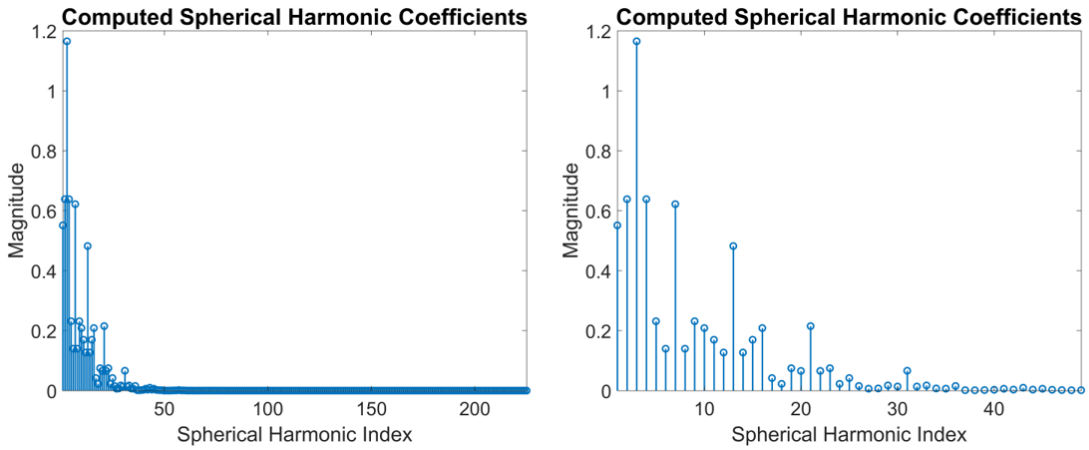

Fig. 6.5. Computed c_{nm} at 1^{st} Harmonic of Opcon. 1

was reconstructed at the locations of the remaining data set, using the fitting model obtained.

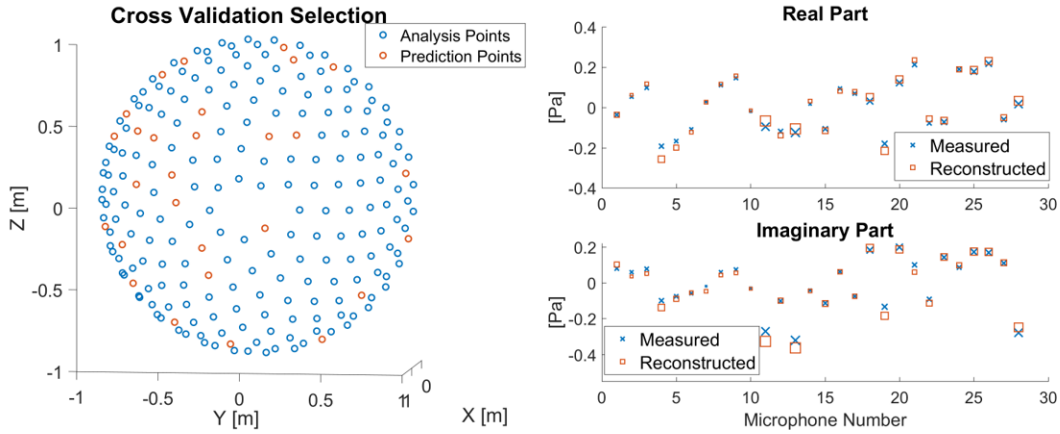

Fig. 6.6. Cross Validation for Reconstruction

That is, 196 measured points were randomly picked for the HELS analysis and the remaining 28 were used for the reconstruction comparison. Their locations are shown on the left of Figure 6.6. The plot on the right of Figure 6.6 compares the

measured and reconstructed data. Although the reconstruction was not perfect, the errors between the two values are in an acceptable region.

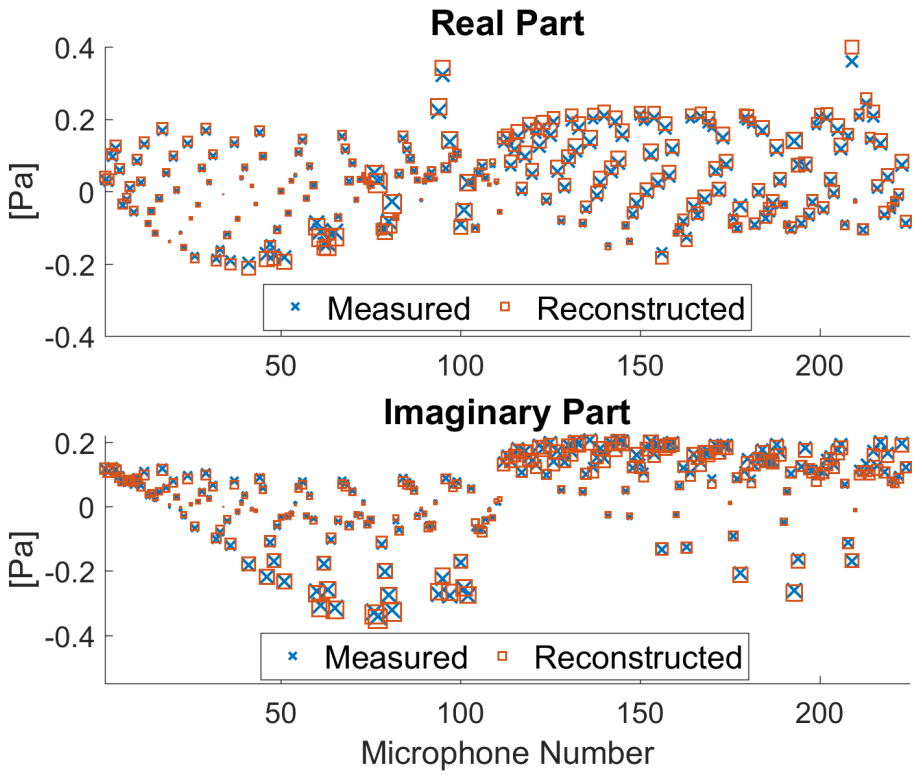

Fig. 6.7. 2 Microphone Validation

The second test was the validation among two different microphones. The robot holds a three-microphone probe, and only one microphone is used for HELS each time. Thus reconstructing at the other microphone locations will give another quick validation of reconstruction. Figure 6.7 highlights the comparison between microphone 1 and microphone 2; between them there is a 0.012 m distance. The reconstruction matches the measured data very well, although the short distance between these 2 microphones to some degree might undermine the credence of the results. The great consistency observed from the graph implies that it is possible to calculate the sound intensity from the reconstructed pressure.

6.2.2 Sound Energy Analysis from HELS

For a fair comparison, both the measured and reconstructed sound intensity are calculated using $p-p$ method. The measured sound intensity is calculated from data collected from microphones 1 and 2, and the reconstructed sound intensity replaces the measured pressure on microphone 2 by the HELS reconstructed pressure. The final comparison in the decibel scale, which is defined as

$$\text{SIL} = 10 \times \log_{10}(\frac{I}{I_{ref}}) \tag{6.4}$$

where $I_{ref} = 1 \times 10^{-12}$ W/m^2. Figure 6.8 provides an overview of the results. The distributions characterized by both methods are very similar. Figure 6.9 shows how the error distributes on the sphere, which is also presented on a decibel scale. The region with the highest error of estimation turns out to be the bottom and a small area on the top near the wall. The discrepancy at the bottom is observed not only in this measurement and analysis, it also appears in many other different tests and analysis, which probably suggests that there exists an intrinsic error caused by the test rig set up. This can possibly be attributed to reflection. Although acoustical foams are placed on the floor, their thickness were approximately 4-5 cm, and the distance between the lowest point of the microphone to the ground were around 10-15 cm. Considering there is also a reflective wall, the sound at the bottom corner region can be interfered with by the reflections. Another possible cause is the pipes that transmit the fluid through the wall. Since their heights are relatively close to the ground, it is logical to infer that these structures may have an influences on the sound. The pipes themselves can produce noise because they are subject to vibration caused by the pressure ripple; besides, as time goes, the air sealing can be damaged by the by their vibration, thus some noise from the motor room may leak into the chamber through the air gap.

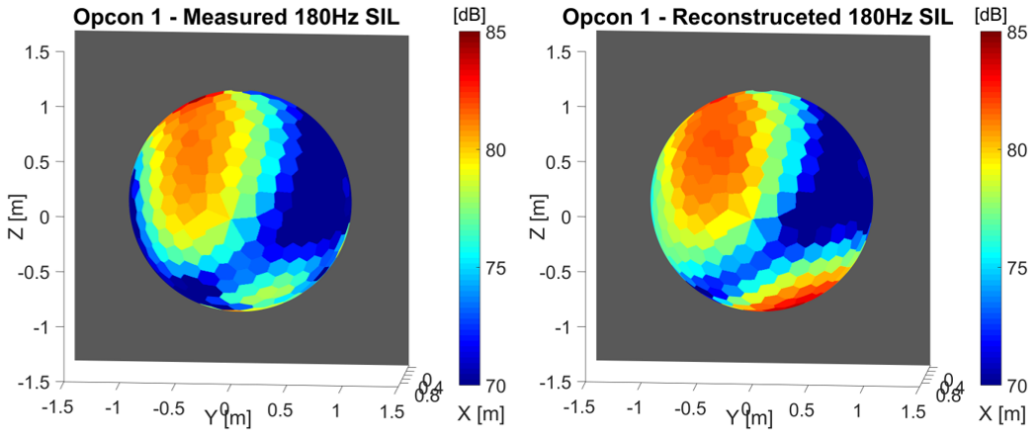

Fig. 6.8. Measured vs. HELS Reconstructed SIL

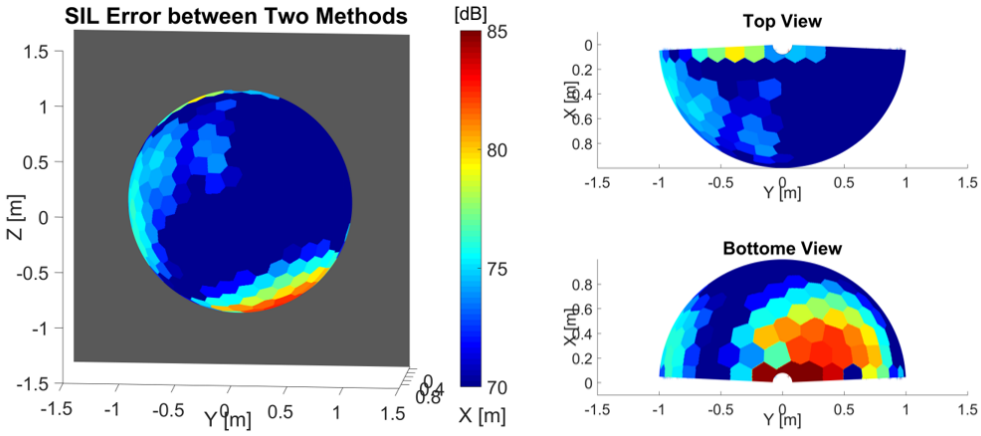

Fig. 6.9. SIL Error between 2 Method

To compare the overall sound intensity estimation by different methods quantitatively, sound powers are calculated. Since the grid satisfies the criteria of equi-area, the sound power can be written as:

$$\Pi = \frac{2\pi r^2}{Q} \sum_{n=1}^{Q} I_n \tag{6.5}$$

where $r = 0.96$ m, and Q is 224 and 225 for both cases respectively. Besides these two methods, there is another approach to get the sound power, which calculates the sound power directly from c_{nm} described by Eq. 4.72. Considering Eq. 4.72 gives

the sound power radiated to a whole field, it is divided by 2 before comparing with hemi-sphere grid, i.e.

$$\Pi = \frac{1}{4\rho c k^2} \sum_{n=0}^{\infty} \sum_{m=-n}^{n} |c_{nm}|^2 \tag{6.6}$$

Only the shaft order components are expected to exist in the synthetic array signals. Thus, we compare the SWL from the 2^{nd} to 99^{th} shaft order (starting from the 2^{nd} because 40 Hz was the lowest frequency for the SIL measurement). Figure 6.10 shows the results. The three results were close to each other. The only exceptions happen at order 50 and order 58. There are strong peaks measured by the probe but not captured by HELS, which means it doesn't exist after TSA. This phenomenon consistently happens on some other the measurements and different machines, which also implies this might be an intrinsic feature in the test rig too. Table. 6.2 and Table. 6.3 list the values of the SWL from the 1^{st} to 10^{th} harmonics. In both cases and at almost all the frequencies, the differences between the $p-p$ method and the HELS-reconstructed values are within 0.5 dB, which is a good result. The 180 Hz case just studied, happens to have the greatest error among all the frequencies. Nevertheless, the difference is, in this case, is still less than 0.8 dB. If looking at the SWL computed by using Eq. 6.6, it is found that this formula always gives higher estimation than the other two methods. It is reasonable because Eq. 6.6 gives exactly half of SWL radiated to the space, but the hologram only covers a hemi-sphere centered off the origin, which only perceives energy slightly less than half of the total.

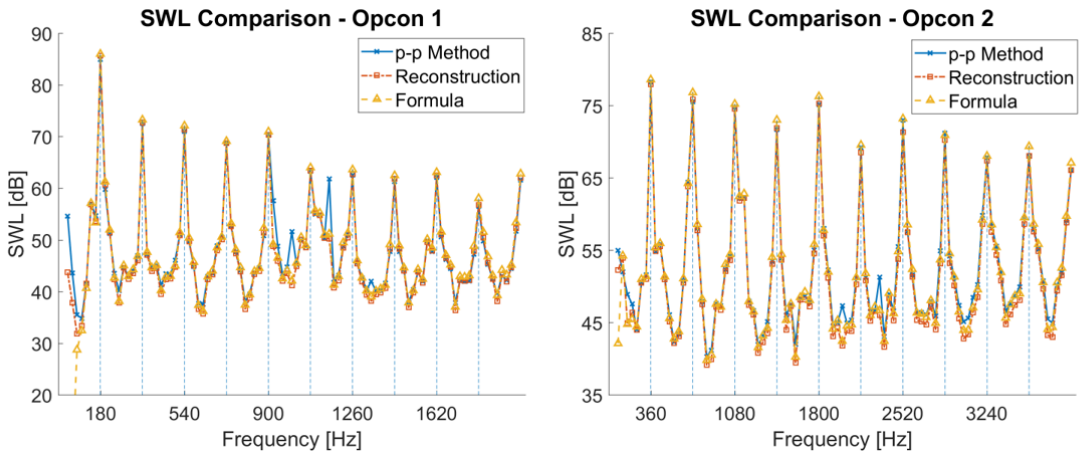

Fig. 6.10. Comparison of SWL Computed by Three Methods

Table 6.2.
SWL Reconstruction Validation - Opcon 1

Frequency [Hz]	$p-p$ Method SWL [dB]	Reconstructed SWL [dB]	Formula SWL [dB]
180	84.90	85.69	86.00
360	72.55	72.78	73.26
540	71.04	71.39	72.11
720	68.77	68.72	69.12
900	70.25	70.36	70.96
1080	63.28	63.41	64.00
1260	62.51	62.73	63.61
1440	61.31	61.85	62.48
1620	62.12	62.46	63.10
1800	56.53	56.78	58.06

Table 6.3.
SWL Reconstruction Validation - Opcon 2

Frequency [Hz]	$p-p$ Method SWL [dB]	Reconstructed SWL [dB]	Formula SWL [dB]
360	78.25	77.97	78.59
720	75.52	75.84	76.81
1080	74.77	74.56	75.22
1440	71.67	71.95	73.01
1800	75.11	75.29	76.27
2160	69.19	68.53	69.56
2520	73.00	71.32	73.20
2880	71.16	70.23	70.91
3240	67.83	67.35	68.04
3600	67.98	68.05	69.36

Now that the sound power calculated by Eq. 6.6 correlate with the measured sound power very well, the coefficients c_{nm} themselves can directly represent the sound energy contributed by different spherical harmonic contents after some manipulations. We define

$$\Pi_{nm} = \frac{1}{4\rho c k^2}|c_{nm}|^2, \tag{6.7}$$

where Π_{nm} is the sound power generated by the spherical wave content at order n and degree m. Then a 2-D spectrum can be made, shown as Figure 6.11. This spectrum shows how sound energy is distributed at different frequencies and different spherical wave contents. Knowing most of the energy is at the pump harmonics, Figure 6.11 excluded other frequency contents. This spectrum can sometimes tell very useful information. In the operating condition 1, most of the noticeable contributors are in the 1^{st} harmonic. Of all the contributors, the vertical dipole dominates. Even in the 2^{nd} and 3^{rd} harmonics, we can literally only see the vertical dipoles. In the operating condition 2, the dipole is still the strongest, although it is not dominating the others like in the operating condition 1. Thinking of how a dipole can be physically generated, it is logical to infer that there is a cantilever motion of the pump is happening under that operating condition. If this inference is true, reducing the cantilever motion should reduce the dipole strength and thus the total radiated power.

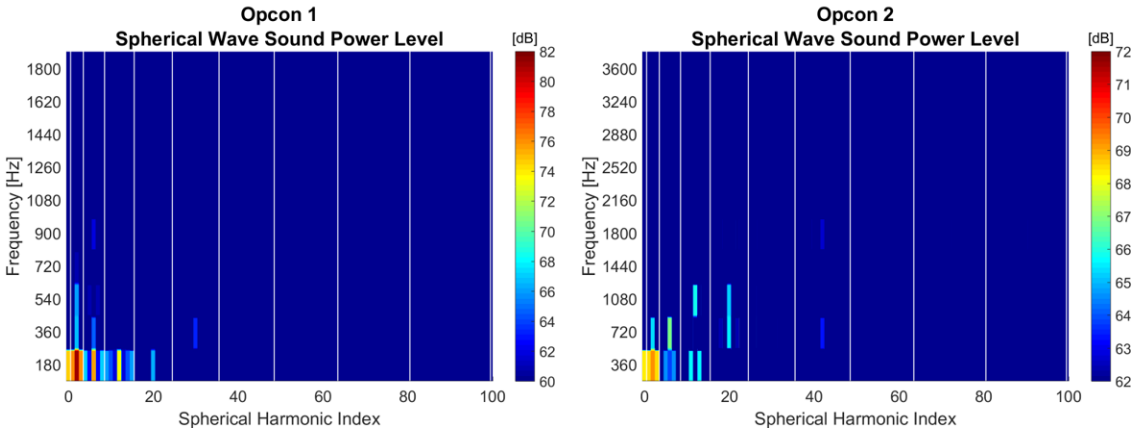

Fig. 6.11. Sound Power Spectrum

In fact, all these analyses presented so far have not completely demonstrated the power of acoustical holography. Other useful information can be obtained, including the sound energy flux and the vibration pattern. Vibration pattern requires the particle velocity on the machine surface to be calculated. The previous simulation study and theoretical analysis have shown that inwardly reconstructing on a small sphere can be challenging when the hologram is on a 1-meter sphere. To avoid being too ambitious, the vector intensity is reconstructed on the plane of $x = 0.8$ m, presented on Figure 6.12. Although the information shown on this graph can hardly be correlated to the physical structure of the machine, it demonstrates a promising future if good results of reconstruction near the machine can be obtained. It can be very helpful to localize the radiation sources, and analayze the vibration patterns of the structrues.

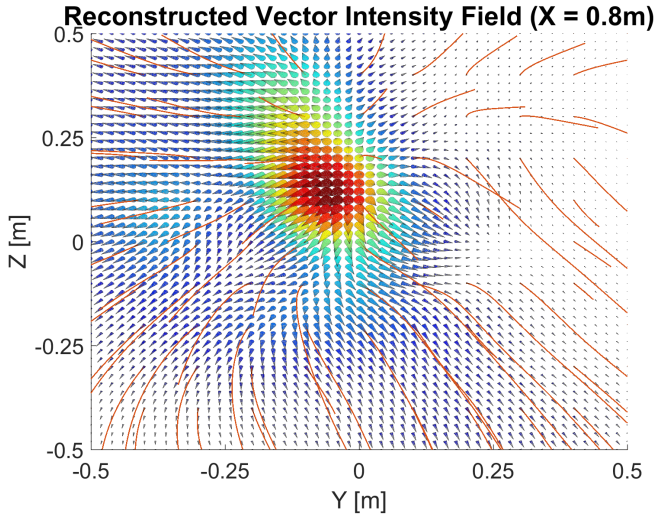

Fig. 6.12. Vector Intensity on $x = 0.8$ m

6.2.3 Inward Reconstruction

Although it has been anticipated that it is difficult to achieve a good reconstruction at a relatively small radius, knowing how the final results look is still helpful. Figure

6.13 highlights the sound pressure reconstruction on two spheres with radii of 0.3 m and 0.5 m, respectively. The two sub-figures on the left are for truncation at $N = 14$. Without any validation, we can conclude the results were wrong because they clearly exceed the possible range of acoustical pressure. If we reduce the truncation order to $N = 3$, shown as the two sub-figures on the right, they are now in a reasonable range. However, the R^2 is also reduced to 0.8963. In other words, including the high order components will lead to the failure of reconstruction inward, but without the high order components, it is not possible to achieve a decent level of fitting.

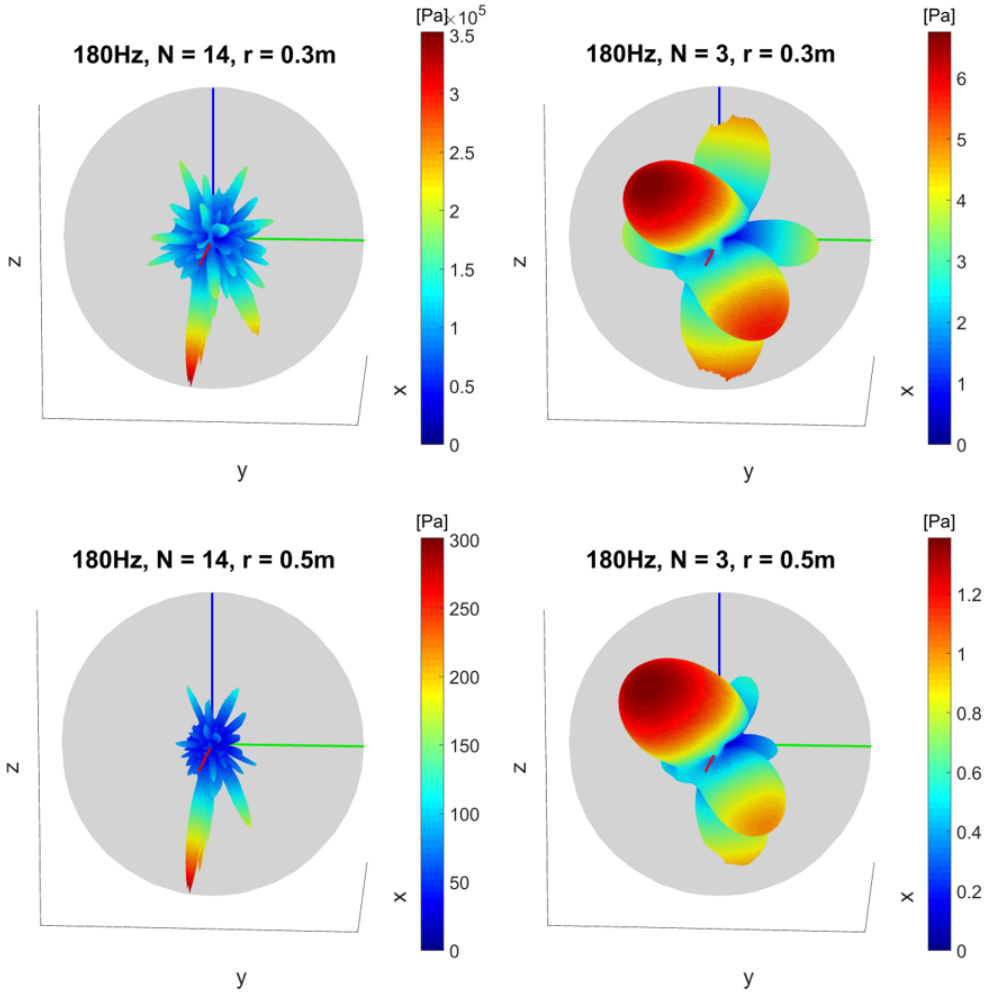

Fig. 6.13. Inward Reconstruction

One of the most important objectives of this work is to understand the limitations of the methods and point out directions for future researchers who will keep working on this topic. The extremely large values, in particular, must be attributed to the high order components. Now that the matrix $\boldsymbol{\Psi}$ (450-by-225 after mirroring) is full rank and well-conditioned, the vector $\boldsymbol{p}$ must be in the column space of $\boldsymbol{\Psi}$. Thus, every estimated coefficient truly reflects the projected length a specific basis. The question that needs to be answered is: where do the high order components come from?

Two types of reasons lead to this result. First, random noise exists in the process of data collection and synthesizing the microphone array. This noise cause variation of measured pressure at each point. Affected by this noise, the true $\boldsymbol{p}$ existing in a subspace of $\boldsymbol{\Psi}$ with lower dimension can outgrow unrealistic components in higher dimensions. This type of noise is inevitable; obtaining a higher SNR and avoiding long-distance inward reconstructing can minimize its effect.

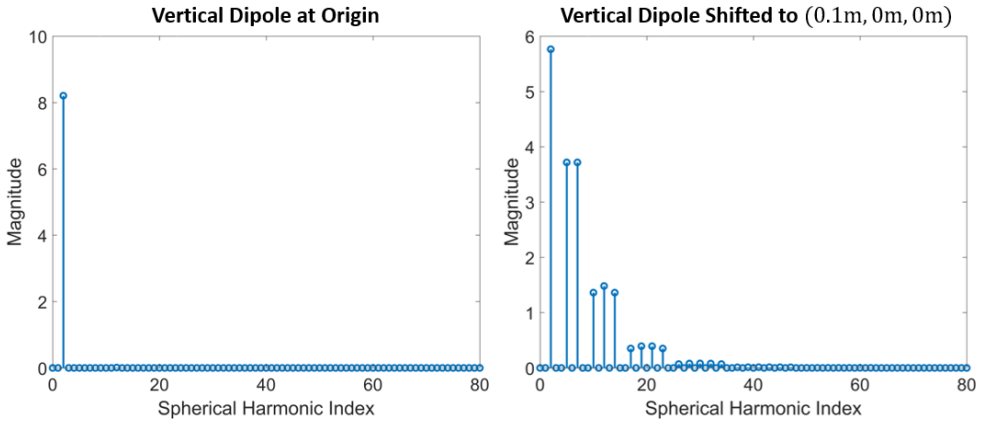

Fig. 6.14. Estimated Coefficients for Vertical Dipole w/o Position Shift

Another reason, playing a more important role, is a characteristic of the solution to the wave equation given by Eq. 4.62. Indeed, the solution described by Eq. 4.62 is a general one; as long as there are infinite terms, any wave field can be described by Eq. 4.62, because the multiplication of $h_n(kr)$ and Y_n^m forms a complete basis. However, Eq. 4.62 is not the only solution (even in the spherical coordinate system) and not

necessarily the simplest one. For example, a vertical dipole can be represented by only one term in Eq. 4.62; but if the source location of the vertical dipole is shifted from the origin, probably an infinite number of terms are needed. As demonstrated by Figure 6.14, by putting the same dipole simulated in case 2 in Chapter 5 away from the origin to $(0.1\text{m}, 0\text{m}, 0\text{m})$, higher order contents start to appear in the estimation. In theory, if manipulating of Eq. 4.62 by coordinate system transform, i.e. writing the spherical harmonic functions and spherical Hankel functions to be originating from the true location of the dipole, then one term will again be enough. In the previous implementation, the origin was set at the intersection of the shaft axis and the wall, which is definitely not the location of the true source (if there is one). As a result, to fit the measured data on the hologram in the sense of least-squares, the high order components must be introduced even for relatively simple sources, which is the limitation of HELS upon the implementation of the current synthetic array.

7. CONCLUSIONS

7.1 Conclusions

This thesis successfully proved the concept of synthetic microphone array based on a robotic measurement system, and implemented an acoustical holography method, HELS, on this array. Differing from traditional methods of dealing with non-synchronous measurements, the method proposed by this thesis does not utilize the reference microphones and estimate the path functions between the field microphones and reference microphones. Instead, it is developed on an assumption of periodicity and a specific synchronization technique to achieve the equivalent effect of a multi-sensor snapshot.

By analyzing the theoretical model of the axial piston machine, it was found that the sources of the FBN and SBN are periodic with the shaft rotation when the system is operated under steady-state. Thus, it is assumed that there must be a periodic component in the sound field, which is called the deterministic component. The actual perceived signal contains this deterministic sound and sound generated by other uncorrelated signals and random noise. Thus, a shaft encoder based on an optical sensor was designed, from which a square wave is generated periodically with the shaft rotation and the edges of the square wave correspond to 2 fixed shaft angles. By recording the sensor signals and the encoder signal in parallel, the signals produced in every shaft revolution can be extracted. Averaging these extracted signals, called TSA, can theoretically obtain the deterministic component. Since the obtained deterministic component on every measurement point starts from a fixed shaft angle, the effect of a snapshot is achieved, which therefore successfully creates a synthetic microphone array.

On a 225-element hemi-spherical synthetic microphone array, HELS is implemented in 2 cases for a 44cc unit open circuit pump operated under different conditions. In both cases, good results were achieved on the hologram and the region that is near the hologram. In fact, 99.99% of the measured pressure on the hologram was described by the HELS estimated model. The cross-validation results and 2-microphone validation demonstrated a good level of prediction ability of the HELS model. Furthermore, the sound intensity and sound power calculated by traditional $p-p$ measurements and HELS reconstruction were compared. If simply looking at the values, the SWL calculated at nearly a hundred frequencies of each case by three methods are very close. By examining the strongest frequency (180 Hz of case 1), it was found that most of the estimation error in the SIL happens in the bottom region that is close to the floor and the wall. This anomaly consistently happens in the same region over different measurements for different machines under different analysis; therefore, it is logical to infer that it is a test-rig-induced error, and most likely because of the reflection from the ground and wall. Another important finding from HELS is, in both cases, the sound power is dominated by the vertical dipole. It might imply that there is a cantilever motion as the machine runs, which is the main cause of the noise.

Although good results were obtained on the hologram, it was difficult to achieve satisfactory reconstruction results in the region that was close to the machine because of a relatively long distance from the hologram to the machine and the properties of spherical Hankel functions. Therefore, the power of acoustical holography, unfortunately, had not been fully exploited. Two possible reasons for the existence of the high order components were summarized. One was the random noise, and the other one was the intrinsic nature of this formulation: it has implicitly assumed the sound is generated from the origin.

7.2 Recommendations for Future Works

After this work, future researchers can safely use the synthetic array. Not only for the axial piston machine, as long as it can be verified that there exists a long-lasting stationary deterministic component, but this technique can also be used for other types of machines' noise diagnostics. As presented, the inward reconstruction was not successful, but there is no doubt a successful reconstruction can provide much valuable information. With the exploration of this work, future work will cost less and give more. According to the analysis of the failure, two recommendations are provided, which will definitely lead to better results.

The first recommendation is about the improvement of the method. Methods such as classical ESM, IBEM, and SONAH, are of course potential options to choose. If future researchers want to move further on HELS, on the same hologram that used in this thesis, the key is to get rid of the high order components, because error and noise will be exaggerated more severely in high orders. Possible solutions can be either changing the locations where the spherical harmonics originate or using spherical harmonics originated from multiple locations. Under the current configuration, the high order harmonics have to be introduced because of the need of the least-squares approach. Adjusting the origin of the spherical harmonics aims to find a location that is closer to the "actual" source, which should be able to reduce the necessary order. However, the sound field can be generated by complex phenomena; therefore, it's not realistic to expect only the lower order sources from one point are enough to describe the whole field. A more recommended alternative is to put the spherical harmonics at multiple locations. With multiple locations, the order at each location can be limited to a relatively low number. In other words, the idea is to achieve the equivalent effect of the single-origin high order sources by more lower order sources distributed at different locations. This method becomes very similar to the classical equivalent source method. In addition to these solutions, a third solution is to design algorithms that place the sound power constraint when performing the inward

reconstruction. Since the sound power estimation on the hologram was demonstrated good, this number should conserve from one radius to another. With this constraint, the reconstructed pressure should be limited to a reasonable range.

The second recommendation involves the modification of the measurement system. The purpose of the modification is to shorten the distance from the machine to the hologram. It brings at least three advantages. First, the shorter distance to the machine leads to higher SNR. Secondly, there is no longer that much error exaggeration to inwardly reconstruct on the machine surface. Third, it also gets rid of the effect of the floor reflection. There are many solutions to achieve this goal. The simplest way without changing the current robotic configuration is replacing the inner arm: see Figure 7.1 which proposes a possible design. With the same kinematics as the current robot, the microphones can be constrained on a sphere with a smaller radius. To allow flexible sphere size adjustment and reserve the ability to take regular sound power measurements, an adjustable feature is also designed. Besides, if taking the sound intensity probe apart, 3 holograms can be at 3 distinct radii (current distances are relatively short) can be created simultaneously. This setup measures the decaying ratio directly, which should increase the robustness of the holography methods.

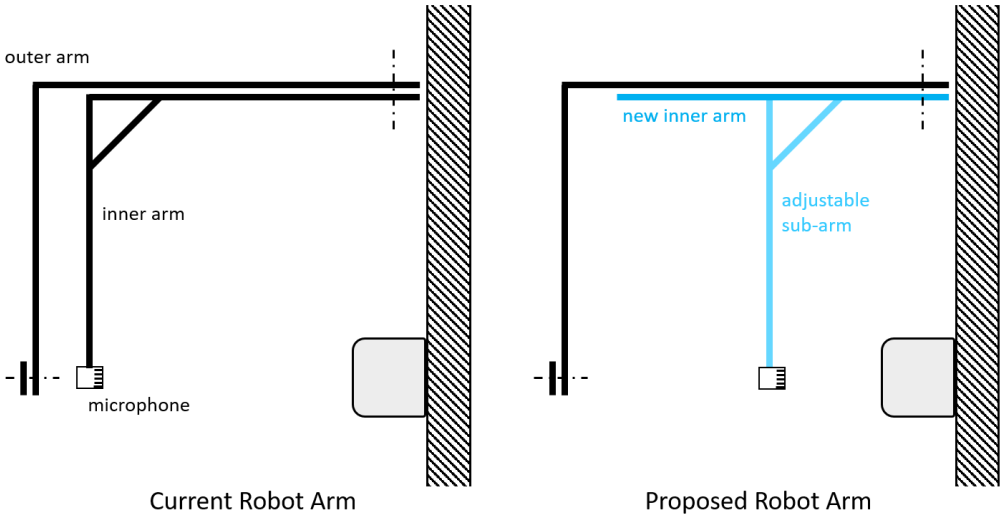

Fig. 7.1. Proposed New Robot Arm

REFERENCES

REFERENCES

Antoni, J., Liang, Y. & Leclère, Q. (2015), 'Reconstruction of sound quadratic properties from non-synchronous measurements with insufficient or without references: Proof of concept', *Journal of Sound and Vibration* **349**, 123–149.
URL: *http://dx.doi.org/10.1016/j.jsv.2015.03.008*

Bai, M. R. (1992), 'Application of BEM (boundary element method)based acoustic holography to radiation analysis of sound sources with arbitrarily shaped geometries', *The Journal of the Acoustical Society of America* **92**(1), 533–549.
URL: *http://asa.scitation.org/doi/10.1121/1.404263*

Bai, M. R., Ih, J.-G. & Benesty, J. (2013), *Acoustic Array Systems: Theory, Implementation, and Application*, John Wiley & Sons Singapore Pte. Ltd., Singapore.
URL: *http://doi.wiley.com/10.1002/9780470827253*

Billingsley, J. & Kinns, R. (1976), 'The acoustic telescope', *Journal of Sound and Vibration* **48**(4), 485–510.

Braun, S. (2011), 'The synchronous (time domain) average revisited', *Mechanical Systems and Signal Processing* **25**(4), 1087–1102.
URL: *http://dx.doi.org/10.1016/j.ymssp.2010.07.016*

British Hydromechanics Research Group (1982), *Quieter Fluid Power Handbook*, BHRA Fluid Engineering.

Brooks, T. F. & Humphreys, W. M. (2006), 'A deconvolution approach for the mapping of acoustic sources (DAMAS) determined from phased microphone arrays', *Journal of Sound and Vibration* **294**(4), 856–879.

Cho, Y. T., Bolton, J. S. & Hald, J. (2005), 'Source visualization by using statistically optimized near-field acoustical holography in cylindrical coordinates', *The Journal of the Acoustical Society of America* **118**, 2355.

Christensen, J. J. & Hald, J. (2004), 'Beamforming', *B&K Technical Review* (1).

Devries, L. A. (1994), Acoustical holography in spherical coordinates for noise source identification, Master, Purdue University.
URL: *http://link.aip.org/link/JASMAN/v95/i5/p2921/s2&Agg=doi*

Ding, D., Ivantysynova, M. & Kalbfleisch, P. (2016), 'Development of data analytics tools for acoustic measurement of positive displacement machines', *The Summer Undergraduate Research Fellowship (SURF) Symposium* .
URL: *https://docs.lib.purdue.edu/surf/2016/presentations/38*

Edge, K. (1999), Designing Quieter Hydraulic Systems Some Recent Developments and Contributions, *in* 'Proceedings of the JFPS International Symposium on Fluid Power', Vol. 1999, pp. 3–27.
URL: *http://joi.jlc.jst.go.jp/JST.Journalarchive/isfp1989/1999.3?from=CrossRef*

Fahnline, J. B. & Koopmann, G. H. (1991), 'A numerical solution for the general radiation problem based on the combined methods of superposition and singularvalue decomposition', *The Journal of the Acoustical Society of America* **90**(5), 2808–2819.
URL: *http://asa.scitation.org/doi/10.1121/1.401878*

Hald, J. (1989), 'Stsfa unique technique for scan-based near-field acoustic holography without restrictions on coherence', *B&K technical review No.1* .

Hald, J. (2009), 'Basic theory and properties of statistically optimized near-field acoustical holography', *The Journal of the Acoustical Society of America* **125**(4), 2105–2120.
URL: *http://asa.scitation.org/doi/10.1121/1.3079773*

Heinz, G., Döbler, D. & Nguyen, T. (1999), 'Acoustic Photo- and Cinematography basing on the H-Interference Transformation (HIT)', *137th meeting of the Acoustical Society of America, 2nd Convention of the European Acoustics Ass. and 25th German Acoustics and DAGA Conference at TU Berlin* .

Horn, S. (2018), Investigation of the shaftspeed fluctuation effect on steady state vibro-acoustic measurements in axial piston pump, Master's thesis, Technische Universitat Dresden.

Ivantysyn, J. & Ivantysynova, M. (2003), *Hydrostatic Pumps and Motors: Principles, Design, Performance, Modelling, Analysis, Control and Testing*, english edn, Akademia Books International, New Delhi, India.

Ivantysynova, M., Huang, C. & Christiansen, S.-K. (2004), 'Computer Aided Valve Plate Design - An Effective Way to Reduce Noise', *SAE Technical Paper* pp. Olems, L. (2000) Investigations of the temperatur.
URL: *http://dx.doi.org/10.4271/2004-01-2621*

Jeans, R. & Mathews, I. C. (1992), 'The wave superposition method as a robust technique for computing acoustic fields', *The Journal of the Acoustical Society of America* **92**(2), 1156.
URL: *http://scitation.aip.org/content/asa/journal/jasa/92/2/10.1121/1.404042*

Kalbfleisch, P. (2015), Computational Valve Plate Design, Master's thesis, Purdue University.

Kalbfleisch, P., Horn, S. & Ivantysynova, M. (2018), Cyclostationary Analysis of Measured Pump Acoustic and Vibration Signals, *in* 'BATH/ASME 2018 Symposium on Fluid Power and Motion Control', Vol. 1, ASME, Bath, UK, p. V001T01A050.
URL: *http://proceedings.asmedigitalcollection.asme.org/proceeding.aspx?doi=10.1115/FPMC2 8899*

Kalbfleisch, P. & Ivantysynova, M. (2012), Noise Reduction in Hydraulic Axial-Piston Pumps and Motors, *in* 'SSAU', pp. Olems, L. (2000) Investigations of the temperatur.

Kalbfleisch, P. K. (2018), Experimental diagnostics and modeling of noise for axial piston machines. Preliminary Report.

Kalbfleisch, P. K., Ding, D., Baruah, A., Ivantysynova, M., Franzoni, G. & Zhang, H. (2019), Swashplate Plate Type Axial Piston Pump Noise Diagnostics for Design, *in* 'The Fourteenth Scandinavian International Conference on Fluid Power', Tampere, Finland.

Kalbfleisch, P., Kim, T. & Ivantysynova, M. (2016), Robotic Arm for Automatic Sound Intensity Measurements, *in* 'BATH/ASME 2016 Symposium on Fluid Power and Motion Control', ASME, pp. Olems, L. (2000) Investigations of the temperatur.
URL: *http://proceedings.asmedigitalcollection.asme.org/proceeding.aspx?doi=10.1115/FPMC2*
1788

Kim, D. (2012), Valve plate optimization focusing on noise reduction in the axial piston machine with high volumetric efficiency, *in* 'FPNI PhD Symposium on Fluid Power', pp. Olems, L. (2000) Investigations of the temperatur.

Kim, T., Kalbfleisch, P. & Ivantysynova, M. (2014), 'The effect of cross porting on derived displacement volume', *International Journal of Fluid Power* **15**(2), 77–85.
URL: *http://dx.doi.org/10.1080/14399776.2014.923605*

Klop, R. & Ivantysynova, M. (2008), Investigation of Noise source Reduction Strategies in Hydrostatic Transmissions, *in* '5th FPNI PhD Symposium'.

Klop, R. & Ivantysynova, M. (2010*a*), Sound Intensity Measurements to Investigate Noise Generation of Hydrostatic Transmissions, *in* 'Proceedings of the 7th international fluid power conference', pp. Olems, L. (2000) Investigations of the temperatur.

Klop, R. & Ivantysynova, M. (2010*b*), Validation of a Coupled Pump-Motor-Line Model to Predict Noise Sources of Hydrostatic Transmissions, *in* 'Proc. of the 6th FPNI PhD Symposium'.

Klop, R. J. (2010), Investigation of Hydraulic Transmission Noise Sources, PhD thesis, Purdue Univeristy.

Klop, R., Williams, K., Dyminski, D. & Ivantysynova, M. (2007), A Simulation Study to Reduce Noise of Compact Power-Split-Drive Transmissions, *in* 'Proc. of the 20th Power Transmission and Motion Control Symposium (PTMC 2007)'.

Koopmann, G. H., Song, L. & Fahnline, J. B. (1989), 'A method for computing acoustic fields based on the principle of wave superposition', *The Journal of the Acoustical Society of America* **86**(6), 2433–2438.
URL: *http://asa.scitation.org/doi/10.1121/1.398450*

Kumar Seeniraj, G., Zhao, M. & Ivantysynova, M. (2011), 'Effect of combining precompression grooves, PCFV And DCFV on pump noise generation', *International Journal of Fluid Power* **12**(3), Olems, L. (2000) Investigations of the temperatur.

Kwon, H.-S., Kim, Y.-J. & Bolton, J. S. (2003), 'Compensation for source nonstationarity in multireference, scan-based near-field acoustical holography', *The Journal of the Acoustical Society of America* **113**(1), 360–368.
URL: *http://asa.scitation.org/doi/10.1121/1.1529669*

Lee, M. & Bolton, J. S. (2006), 'Scan-based near-field acoustical holography and partial field decomposition in the presence of noise and source level variation', *The Journal of the Acoustical Society of America* **119**(1), 382–393.
URL: *http://asa.scitation.org/doi/10.1121/1.2133717*

Liu, Y. (2016), Efficient Modeling of Sound Source Radiation in Free-Space and Room Environments, Phd, Purdue University.

Maynard, J. D., Williams, E. G. & Lee, Y. (1985), 'Nearfield acoustic holography: I. Theory of generalized holography and the development of NAH', *The Journal of the Acoustical Society of America* **78**(4), 1395–1413.
URL: *http://asa.scitation.org/doi/10.1121/1.392911*

McFadden, P. D. (1989), 'Interpolation techniques for time domain averaging of gear vibration', **3**(1), 87–97.

Nejade, A. (2014), 'Reference-less acoustic holography techniques based on sound intensity', *Journal of Sound and Vibration* **333**(16), 3598–3608.
URL: *http://dx.doi.org/10.1016/j.jsv.2014.03.031*

Oppenheim, A. V., Willsky, A. S. & Nawab, S. H. (1996), *Signals and Systems*, second edn, Pearson, Upper Saddle River.

Opperwall, T. & Vacca, A. (2013), Performing and Interpreting Experiments Towards Understanding Noise Generation in Displacement Machines, *in* 'The 13th Scandinavian International Conference on Fluid Power, SICFP2013'.

Proakis, J. G. & Manolakis, D. G. (2006), *Digital Signal Processing - Principles, Algorithms, and Applications*, fourth edn, Pearson Education, Inc.

Rafaely, B. (2015), *Fundamentals of Spherical Array Processing*, Vol. 8 of *Springer Topics in Signal Processing*, Springer Berlin Heidelberg, Berlin, Heidelberg.
URL: *http://link.springer.com/10.1007/978-3-662-45664-4*

Schmidt, R. D. (1981), A Signal Subspace Approach to Multiple Emitter Location and Spectral Estimation, PhD thesis, Stanford University.

Seeniraj, G. K. & Chandran, R. S. (2011), 'Study Into Effect of Dead Center Position on Pressure and Flow Ripples of a Variable Displacement Axial Piston Swash Plate Hydraulic Pump', *The Twelfth Scandinavian International Conference on Fluid Power* pp. Olems, L. (2000) Investigations of the temperatur.

Seeniraj, G. K. & Ivantysynova, M. (2006), Impact of Valve Plate Design on Noise, Volumetric Efficiency and Control Effort in an Axial Piston Pump, *in* 'ASME International Mechanical Engineering Congress and Exposition', pp. Olems, L. (2000) Investigations of the temperatur.

Seeniraj, G. K. & Ivantysynova, M. (2008), 'Noise Reduction in Axial Pison Machines Based on Multi-Objective Optimization', *5th FPNI PhD Symposium* pp. Olems, L. (2000) Investigations of the temperatur.

Skaistis, S. (1962), 'Sounds of Hydraulics, Pumps and Motors', *Design News* pp. 14–19.
URL: *https://www.youtube.com/watch?v=G1mOt6R3bJw*

Standard, I. (1991), 'ISO 4412-1:1991 Hydraulic fluid power – Test code for determination of airborne noise levels – Part 1: Pumps'.

Standard, I. (2002), 'ISO 4412-2 Hydraulic Fluid Power - Test Code for Determination of Airborne Noise Levels - Part 2: Motors'.

Standard, I. (2007), 'ISO 4409:2007 Hydraulic Fluid Power: Positive-Displacement Pumps, Motors and Integral Transmissions: Methods of Testing and Presenting Basic Steady-State Performance'.

Standard, I. (2011*a*), 'ISO 16902-1 Hydraulic Fluid Power Test Code for the Determination of Sound Power Levels Using Sound Intensity Techniques: Engineering Method Part 1: Pumps'.

Standard, I. (2011*b*), 'ISO 4412-3 Hydraulic Fluid Power - Test Code for Determination of Airborne Noise Levels - Part 3: Pumps - Method Using a Parallelepiped Microphone Array'.

Wang, Z. & Wu, S. F. (1997), 'Helmholtz equationleast-squares method for reconstructing the acoustic pressure field', *The Journal of the Acoustical Society of America* **102**(4), 2020–2032.
URL: *http://asa.scitation.org/doi/10.1121/1.419691*

Williams, E. G. (1999), *Fourier Acoustics: Sound Radiation and Nearfield Acoustical Holography*, Academic Press, Washington. D.C.
URL: *http://asa.scitation.org/doi/10.1121/1.1289662*

Williams, E. G., Maynard, J. D. & Skudrzyk, E. (1980), 'Sound source reconstructions using a microphone array', *The Journal of the Acoustical Society of America* **68**(1), 340–344.
URL: *http://asa.scitation.org/doi/10.1121/1.384602*

Wu, S. F. (2008), 'Methods for reconstructing acoustic quantities based on acoustic pressure measurements', *The Journal of the Acoustical Society of America* **124**(5), 2680–2697.
URL: *http://asa.scitation.org/doi/10.1121/1.2977731*

Yu, L., Antoni, J. & Leclère, Q. (2016), 'Spectral matrix completion by Cyclic Projection and application to sound source reconstruction from non-synchronous measurements', *Journal of Sound and Vibration* **372**, 31–49.
URL: *http://dx.doi.org/10.1016/j.jsv.2016.02.031*

Yu, L., Antoni, J., Leclère, Q. & Jiang, W. (2017), 'Acoustical source reconstruction from non-synchronous sequential measurements by Fast Iterative Shrinkage Thresholding Algorithm', *Journal of Sound and Vibration* **408**(November), 351–367.
URL: *http://dx.doi.org/10.1016/j.jsv.2017.07.036*

Yu, L., Antoni, Jérôme & Leclère, Q. (2014), Recovering phase relationships between non-synchronous microphone array measurements, *in* 'Proceedings of the International Conference on Noise and Vibration Engineering', number September, pp. 1415–1429.

Yu, L., Jiang, W., Antoni, J., Leclère, Q. & Wu, H. (2018), Acoustic beamforming by non-synchronous microphone array measurements, *in* 'Berlin Beamforming Conference', number March, pp. 1–14.